Spatial Frequency Domain Imaging for Characterising the Wound Healing Process

LAI ZHANG

Spatial Frequency Domain Imaging for Characterising the Wound Healing Process

Lai Zhang

A thesis presented for the degree of

Doctor of Philosophy

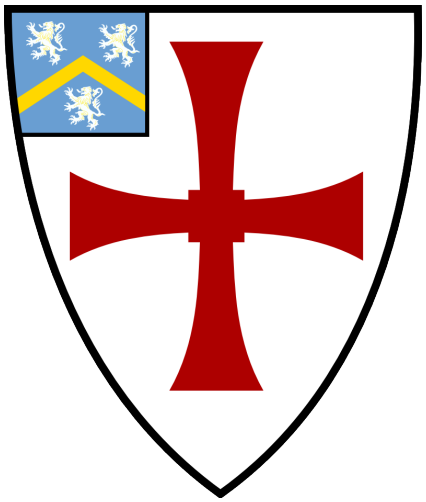

Centre for Advanced Instrumentation

The University of Durham

United Kingdom

October 2023

"I understand now that boundaries between noise and sound are conventions.

All boundaries are conventions, waiting to be transcended.

One may transcend any convention if only one can first conceive of doing so."

Cloud Atlas, 2004

Spatial Frequency Domain Imaging for Characterising the Wound Healing Process

Lai Zhang

Abstract

Postoperative surgical wound infection is a serious global problem and a non-contact and early diagnosis method is urgently required. In this thesis, we explore the use of spatial frequency domain imaging (SFDI) as a non-contact optical imaging method for characterising surgical wound healing and detecting early infection. Firstly, a numerical model is built up for analyse the vertical heterogeneity in biological tissue using the Monte Carlo method. The lateral resolution of SFDI is determined related to the wound width, the reduced scattering and the spatial frequency used. Then, we set up a practical SFDI system and conduct resin phantom experiments to validate the result of the simulation. Finally, we have three clinical interesting cases: SLS triggered acute skin irritation, chronic eczema and biopsy wound monitored by our SFDI system for the first time. SFDI is found to have great potential in characterising the wound area after surgery.

Supervisors: Prof. John Girkin and Prof. Timothy Morris

Acknowledgements

First and foremost, my greatest thanks go to my supervisor Prof. John Girkin. I thank John for his guidance, support and believing in me from the time I applied for this PhD. He taught me to keep things simple and his enthusiasm inspires me in both research and life. John is an extremely kind, caring and knowledgeable supervisor that I couldn't ask more! I would also thank Dr Alistair Bounds for supervising me during the Covid time, reviewing papers and designing the first version of phantom recipe.

I thank our collaborators Denise and Anderson for the fantastic Brazil trip. Thank you APC group for maintaining the Hamilton and Dr Karen Bower for providing speedy solutions to my simulations. Physically, SFDI instrument could not be built up without the helps from the department mechanical and electronic workshop.

Huge thanks must go to our anonymous volunteers for providing invaluable *in vivo* human measurement opportunities for my PhD project.

I thank everyone in CfAI for creating such a friendly and warm atmosphere to work in. I will always feel proud to be a part of CfAI family. All pub trips, pizza and coffee do shaped me. Thank you all the members in Biophotonics group (past and present: Alistair, Penny, Amrit, Larry, Cyril, John, Chris, Josh, James, Jeremi and Wenyue) for the lab help, Xmas lunch, bio-meeting and mental support during the lockdown time.

Outside work, I feel lucky to have my dear friends in Durham: Kim, Yuankang, Siyu, Zhengquan, Yuchan, Nuo, Jiayun, Xuewen, Zhida and Han. My special thanks goes to Xingyu for being my bestie and growing up together since 1999!

I would express my deepest gratitude to my family. Thank you mom and dad for always supporting my bold decisions and offering unconditional love. The long distance from UK to China never set us apart but links us tightly. Thank you my

partner Dr Muyang for all love, understanding and encouragement. We unite as one to conquer difficulties and share the joy through each other's PhD life.

My PhD journey cannot step so far without the help and support from any of you!

Contents

Declaration

The work in this thesis is based on research carried out at the Centre for Advanced Instrumentation, Department of Physics, University of Durham, England. No part of this thesis has been submitted elsewhere for any other degree or qualification, and it is the sole work of the author unless referenced to the contrary in the text.

Some of the work presented in this thesis has been published in journals and conference proceedings - the relevant publications are listed below.

Publications

Zhang, L., Bounds, A., & Girkin, J. (2023). Monte Carlo simulations and phantom modeling for spatial frequency domain imaging of surgical wound monitoring. Journal of Biomedical Optics, 28(12), 126003-126003.

Zhang, L., Bounds, A., Fleming, J., & Girkin, J. (2022, August). Using Monte Carlo simulation for the spatial frequency domain imaging and monitoring a case of biopsy wound. Biophotonic Workshop 2022, IPEN University of São Paulo.

Zhang, L., Bounds, A. D., Fleming, J. P., & Girkin, J. M. (2022, August). Characterizing surgical wound sites with spatial frequency domain imaging (SFDI). In Latin America Optics and Photonics Conference (pp. Tu1B-7). Optica Publishing Group.

Zhang, L., Bounds, A. D., Fleming, J. P., & Girkin, J. M. (2022, July). Spatial frequency domain imaging (SFDI) method for characterizing surgical wound sites. In Imaging Systems and Applications (pp. ITu3E-2). Optica Publishing Group.

Zhang, L., Bounds, A., Fleming, J., & Girkin, J. (2022, March). Monitoring of surgical wound healing using spatial frequency domain imaging. In Society of

Photo-Optical Instrumentation Engineers (SPIE) Conference Series (Vol. 11974, p. 1197407).

In preparation

The following two papers will be submitted before the viva:

"Using spatial frequency domain imaging to monitor a skin biopsy wound: A pilot study."

"Monitoring skin condition with spatial frequency domain imaging for eczema and chemical challenges."

List of Figures

List of Tables

Nomenclature

SFDI spatial frequency domain imaging

RTE radiative transfer equation

MTF modulation transfer function

LUT look up table

R_d diffuse reflectance

AC alternating component

DC direct component

s-PSF spatial point spread function

DMD digital mirror device

SNR signal noise ratio

Hb deoxy-hemoglobin

HbO_2 oxy-hemoglobin

StO_2 oxygen saturation

SLS sodium lauryl sulfate

VIS visible

IR infrared

LDI laser Doppler imaging

ICD irritant contact dermatitis

OCT optical coherence tomography

TEWL trans-epidermis water loss

PDT photon dynamic therapy

Chapter 1

Introduction

1.1 Surgical site wound healing and infection

The human skin is the largest organ in body serving as the first barrier to the pathology. It plays a key function interfacing between the body and the outside world, including sensing and linking the internal tissues. The damage in the skin disrupts the physical function of the skin and also weakens the defence barrier.

There are situations in which there is a requirement to temporarily cut the skin when invasive surgery is an effective and widely used approach for illness diagnosis and treatment. Clinicians open the skin and underneath tissue layer by layer to reach the target site. After the operation is finished, the the incision is closed and forms a surgical wound.

Postoperative care is also crucial for the primary disease treatment. Surgical site infection (SSI) is a global healthcare problem leading to high morbidity and mortality while significantly adding burden in surgical expense and procedures. In the UK, SSI accounts for up to 1 in 7 hospital patient acquired infections[17]. Patient with SSI are required to stay 7 - 11 days longer compared to the patient without such wound infections. On a population basis, the estimated cost attribute to SSI is £700 million per annual to the National Health Service (NHS) in UK[18]. The medical human resource cost is also significant along with the money expense.

The annual wound management involves around 54.4 million district/community nurse visits, 53.6 million healthcare assistant visits and 28.1 million practice nurse visits[19]. This illustrates why a method to rapidly detect SSI is important area to study.

1.1.1 Human skin structure

Human skin is formed of three main layers including epidermis, dermis, and subcutaneous tissue.[20] Together they significantly serve the human body with their anatomy and function. The geometry of the skin is shown in Fig. 1.1.

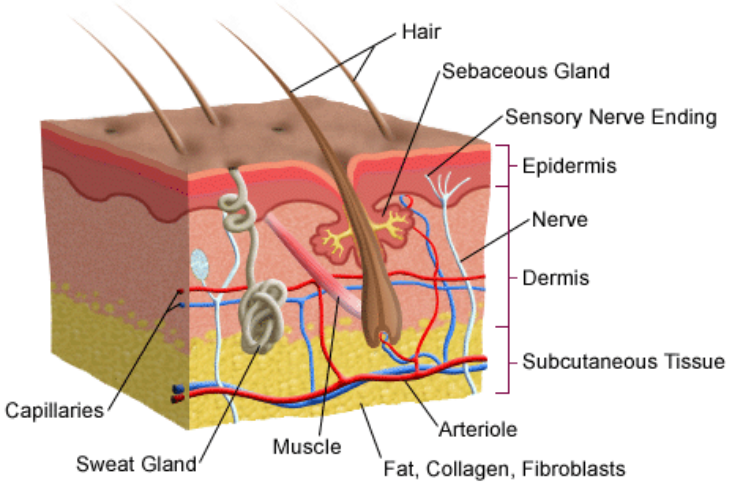

Figure 1.1: The cross section of human skin anatomy, adapted from [1].

The epidermis is the superficial layer of the skin 80% formed by keratinocytes[21]. This layer acts as a protective layer and provides the skin of colour with melanin. There is a continuously regeneration in the epidermis by keratinization progressively undergoing with cells generating in the stratum germinatum of the epidermis[22]. As the cells mature, they migrate to the outer layer of the epidermis and become flatter.

The medium layer dermis contains collagen fibres and elastic fibres also facilitating vessel network and nerve endings, hair follicles and glands[23]. This layer provides nutrition support for the epidermis and the elasticity of the skin. The collagen

is the principal filamentous protein occupying 18% - 30%[24] of the dermis and serving as the principal protein.

The bottom layer of skin is the subcutaneous tissue (also known as hypodermis)[25]. It attaches the skin to muscles, bones and organs also serving as a shocker absorber for protection. The vessels and nerves in the dermis are branching out to body through subcutaneous tissue. The subcutaneous tissue also helps to regulate the body temperature as storing body's fat.

1.2 Physiology of the wound healing

The surgical wound normally takes two to three weeks to be visibly healed. The skin wound healing time scale is depended on the wound size, shape and depth. Other factors influence the healing time include the position of the wound, age of the patient and patient's conditions (e.g. diabetes, smoking and weakened immune system). There are four overlapped stages[2, 26] in the wound healing process: early response, inflammation, new tissue formation and remodelling. The diagram for demonstrating the physiological process is shown in the Fig. 1.2.

Early response Haemostasis appears immediately when blood starts to leak[27]. It prevents the blood loss and protects the vascular system of the tissue. The vasoconstriction occurs and platelets become active and aggregate in the injury site. The blood clot is formed from insoluble fibrin which fills the wound bed as a provisional wound matrix. At the same time it traps the platelets and attracts the immune cells to the wound site.

Inflammation Right after the injury, the inflammation stage occurs and normally last for 2 - 5 days[27, 28]. The injured blood vessels leak transudate leading to the local swelling appears as inflammation. The soluble fragment of degraded collagen recruits the immune cells while acting as signal to promote the develop-

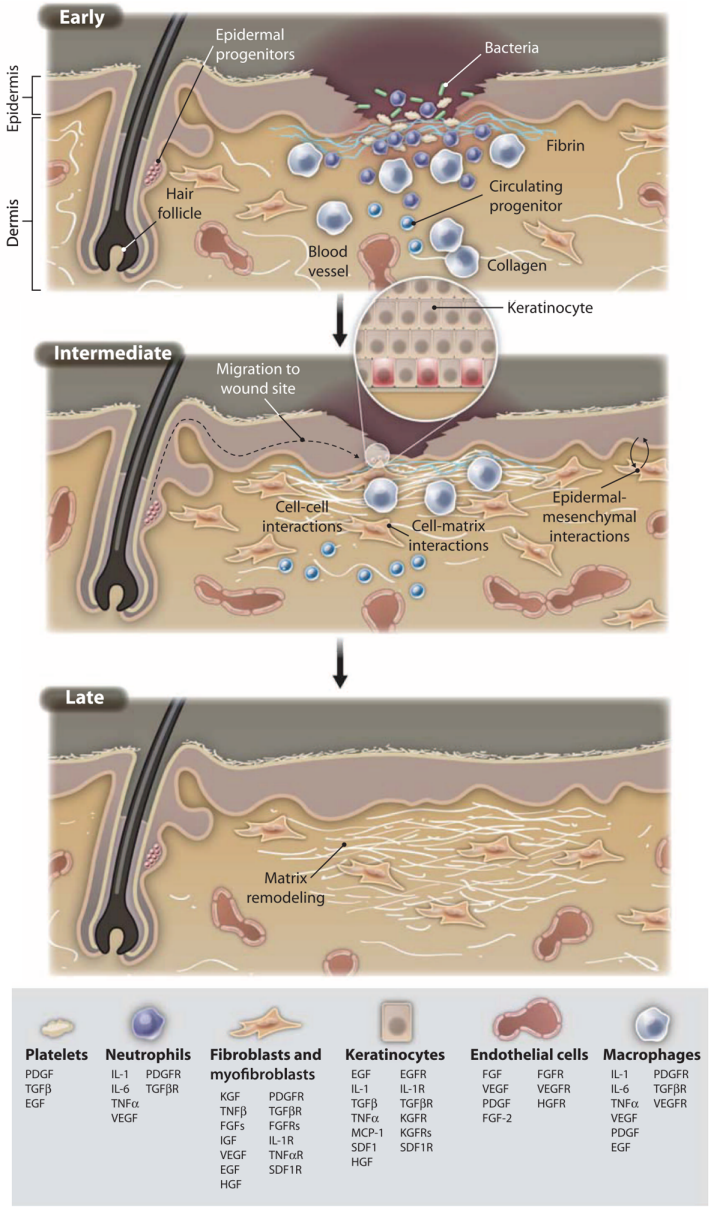

Figure 1.2: The diagram for the wound healing process adapted from [2]. The early phase picture is for the early response and inflammation stage, the intermediate picture is for the proliferation stage, the late picture is for the remodelling stage. The bottom bar is the legends for the cell involved in the wound healing.

ment of new blood vessels[29]. The immune cells are delivered through the blood flow to patrol the wound[26]. The neutrophils clear the bacteria and produce the reactive oxygen. The macrophages remove dead cells, debris and bacteria. In appearance, a scab is formed to protect the wound and provides a ideal moisture

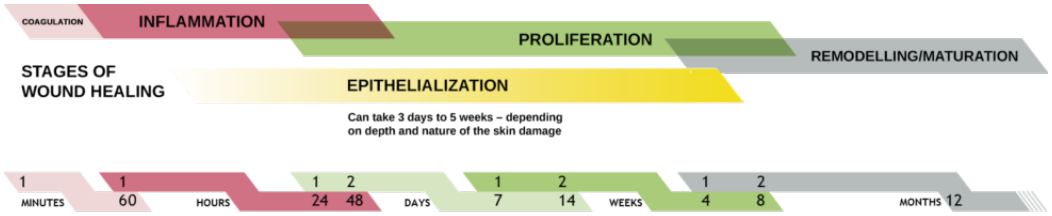

Figure 1.3: The graphic timeline representation for the wound healing stages adapted from [3]. The four stages are overlapping to each other and working jointly.

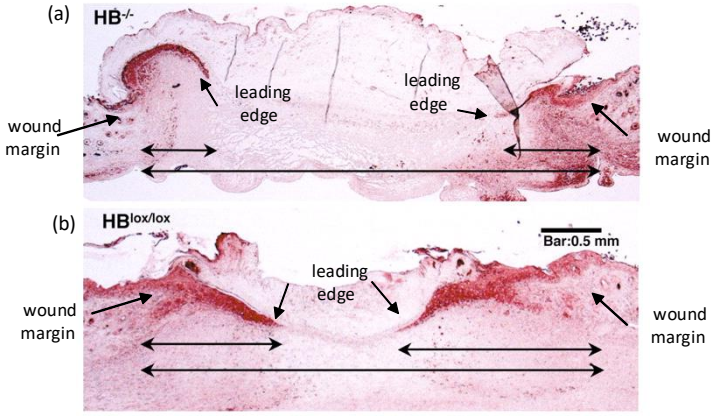

Figure 1.4: (a) The biopsy section from the keratinocyte-specific Heparin-binding growth factor (HB-EGF) knockout mice ($HB^{-/-}$) at the day 7 of wound healing. Without the keratinocyte-specific HB-EGF, the re-epithelialization cannot happen in the wound healing. (b) The biopsy section from the normal mice ($HB^{lox/lox}$) measured at day 7 in the wound healing. The keratinocyte migration can be seen from the leading edge change resulting the wound contraction. The epidermis was stained with anti-keratin antibody. The picture is adapted from [4].

environment for wound healing. The swelling, heat, pain and redness are common signs in the inflammation stage of wound healing.

Proliferation The proliferation stage starts approximately 10-12 days after wounding and can last for two weeks thereafter[30]. The granulation tissue forms from the previous provisional wound matrix replacing the fibrin clot with capillary-rich fibroblastic tissue[31, 32]. In this process, angiogenesis generates new capillaries to replace the damaged vessels and restore circulation. At the same time, fibroblasts proliferate and deposit collagen and extracellular matrix (ECM) aiding with granulation formation. As a result, the wound contracts by the deposition process due

to granulation tissue gradually filling the wound gap[33]. Parallel with this, the re-epithelialization takes place where keratinocytes migrate from the edge of the wound to the centre of the wound as shown in the Fig. 1.4. Thus, the epidermis is thickened at the top of the wound and resurfaces the skin.

Remodelling This is the final and longest stage of the wound healing process, taking from months to years[26]. In this stage, the new epithelium and final scar are developed. The cells no longer needed for the wound repair are removed or programmed for cell death. Meanwhile, the capillaries stop growing and blood flow to the wound area decreases.[34] The collagen matrix in the dermis are remodelled from type 3 to type 1 (a more stable form of the collagen) resulting in a more oriented and cross-linked structure. The tensile strength of the tissue is increased but is still lower than the strength of unwounded skin area. In the end, the wound site turns into a fully matured scar with high tensile strength.

1.2.1 Wound infection

The majority of surgical wound infections are superficial skin infections[35]. The wound infection can happen at any time 2 to 3 days after the surgery until the wound is fully healed[36] The infection is caused by the bacteria contaminate the wound site. In most SSIs, the responsible pathogens originate from the patient's endogenous flora, including staphylococcus aureus, coagulase-negative staphylococci, enterococcus spp. and escherichia coli.[37]. The risk factors of the wound infection are the basic health condition of the patient, the degree of bacterial wound contamination, and use of antibiotic prophylaxis. The wound infection contributes negatively to each stage of wound healing, including disruption, tissue damage or slower and deeper scarring[38].

The identification for the wound infection has always been a challenge for the wound management[39]. Currently 98% of the wound infection is diagnosed based on the clinical sign of the wound via naked eye observation accompanied with symptoms

reported from the patient and wound cultures[40]. The signs include absecess, discharge (serous exudate with inflammation, seropurulent, heamopurulent, pus) and cellulitis[41, 42]. The golden standard[43, 44] for the diagnosis is wound culture acquired by a swab or biopsy to determine the antibiotics regime. These methods are invasive and take several days to culture, frequently making it's too late for the early treatment. Along with the infection control in the surgery and wound dressing, the rapid, highly specific and accurate diagnosis for wound infection is significantly required by clinicians.

Before the clinical characteristics of the wound infection becoming visible, most of the symptoms have been developed underneath. Therefore the optical method is feasible in non-contact skin imaging for the wound infection. Along with regular infection prevention protocols, the close monitoring and early infection detection are significant for accurate and effective treatment.

There are two factors we are interested at in this thesis, one is the sign of the infection. Can we determine the infection earlier than the naked eye can figure out or before patient report? The other factor is characterising wound structure change precisely. As quantification of the wound structure change is significant for monitoring the all aspect of the wound progress. It serves as a overall determination for the wound healing and repairing outcome.[45]. Along with these two aspects, the other biomedical markers and their changes during the wound healing are also of great interests to clinicians. We are looking to explore the wound healing monitoring with optical imaging method to detect them at the same time.

1.2.2 Optical methods for skin imaging

Optical imaging tools can provide more detailed, accurate, potentially quantifiable and earlier information on the wound healing process for detection, diagnosis and monitoring of treatment compared to visual inspection alone[46]. There have been non-invasive imaging methods aiding with the wound monitoring along with the

visual inspection. For skin imaging and clinical diagnosis, there are state-of-art instruments as potential candidates.

Optical coherence tomography Optical coherence tomography (OCT)[47] scans the biological tissue like an optical "ultrasound" to provide high resolution (3-5 μm) structure information. There have been matured OCT instruments used in hospital for retina assessment[48, 49]. For skin imaging, OCT has been employed to characterising the collagen denaturation[50], epidermis presence in wound healing[51, 52, 53] and burn wound depth[54]. The image depth of OCT for human skin is around 0.5 mm. The trade-off of OCT in high resolution in vertical 2D structure is the time costing for the the point-to-point scan. However, the OCT is not capable to measure the absorption coefficient which limits in monitoring the chromophores concentration in the wound healing.

Optoacoustic imaging Optoacoustic imaging (OA)[55, 56] is conducted by projecting short laser pulse to be absorbed within the target tissue area and consequent generation of pressure waves are introduced by the thermal expansion. OA is advance in detecting the chromophores through the human skin and reconstruct capillary and lipid structures with high resolution (laterally 4 μm). The detection depth is from 1 mm to 10 mm depending on the wavelength utilised. It has been applied to detect and quantify cancer[57, 58], skin layers[59], burn wound depth[60, 61, 62] and ulcers[63]. However, the field of view is limited to couples of millimetre[64] range which is not effectively matching for surgical wound size. At the same time, epidermis migration and the collagen structure cannot be determined by OA.

Spatial frequency domain imaging Spatial frequency domain imaging (SFDI) is a rapid and wide field non-contact imaging tool for mapping reduced scattering coefficient μ_s' and absorption coefficient μ_a of the biological tissue[65, 6, 5]. The reduced scattering properties μ_s' is an indicator of the structural change whilst the absorption present the chromophore concentration. The field of view is relatively

larger, i.e. 3 cm × 3 cm, which is feasible for surgical wound site imaging. SFDI has been utilised for a range of clinical applications[66, 67, 68] for *in vivo* and preclinical model study [69, 70] for the skin complication measurement. SFDI can provide rapid imaging to the wound site and by changing the spatial frequency, one can obtain the tomography information. The cost for build and maintenance SFDI system is cost-effective in the laboratory, i.e. approximate 2269 dollars for optical components according to openSFDI instruction[71]. However, the trade-off here is the lateral resolution of SFDI is relatively lower at 1 mm[6] and the mathematics model is complex.

Laser Doppler imaging The laser Doppler imaging (LDI)[72, 73] is developed based on the Doppler shifting where incident light undergoes a change in the frequency when encounter the moving blood cells. The blood perfusion can be calculated with LDI method which have been used as an healing indicator for burn wound[74, 75]. However, this method cannot provide information neither on the other structural or absorption chemical change.

Hyperspectral imaging The hyperspectral imaging (HSI)[76, 77] is capable for determining the skin chromophores by reflectance from the skin area are taken with different wavelength. HSI have been employed in various research to obtain the water, lipid, oxy-hemoglobin, deoxy-hemoglobin and melanin distribution and concentration in the skin. It has been a good candidate for monitoring the skin complications[10, 78, 79] combining with classification method[80, 81]. However, the reduced scattering and absorption coefficients in the skin cannot be derived from HSI measurements.

By comparing the prons and cons for the above optical imaging tools, the SFDI method matches our purpose best. The wound size will be at centimetre range, which requires a larger field of view in the imaging. At the same time, SFDI is capable to detect the structural change, e.g. collagen, skin fibrosis and epi-

dermis presence, by reduced scattering coefficient. At the same time, absorption coefficient can be separated from the SFDI imaging result. This will aid us in monitoring hemodynamic such as hemoglobin and oxygen saturation which indicating the blood volume and metabolism activity in the target area.

Therefore, in this thesis we will explore SFDI for early sign of infection detection and wound healing monitoring. The principle behind SFDI and detailed review of its applications will be introduced in the following section.

1.2.3 Spatial frequency domain imaging

Spatial frequency domain imaging (SFDI) was first proposed by Beckman Laser Institute in University of California, Irvine in 2009 by Cuccia et al[6]. It is a quantitative, wide-field and non-contact imaging tool for mapping the optical properties of tissue with the ability to provide depth information[65, 6, 5]. The diagram in the Fig. 1.5 illustrates how SFDI works.

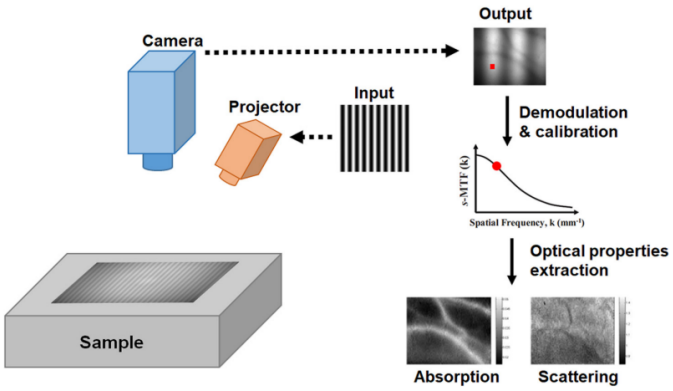

Figure 1.5: SFDI method projects three phases sine patterns to the tissue separately. A camera records diffuse reflected light from the tissue for each individual pattern. The collected images are calibrated and demodulated to obtain the spatial modulation transfer function (MTF) of the tissue to recover the reduced scattering and absorption coefficient. Picture adapted from [5].

In this thesis, we utilise SFDI method for the wound healing observation as it is capable in mapping the reduced scattering coefficient μ_s' and absorption coefficient μ_a of the tissue at millimetre resolution.

1.2.4 SFDI application for biological tissue

For the acute wound, SFDI aids in assessment of burn wound depth and severity[69, 70] within 72 hours in porcine model and infection risk prediction [82] in rat model. The hemoglobin breakdown in the burn wound is analysed with spectral information with SFDI[83]. For the chronic wound and long-term skin condition, risk of diabetic foot ulcers[66], pressure ulcers[67] and scleroderma skin are assessed by SFDI[68].

Beside from the wound imaging, SFDI is applied to the cancer field for diagnosing nonmelanoma skin cancer[84] and determining the breast cancer margin in surgery[85]. SFDI demonstrates the potential to detect early stage dental caries [14] by quantitatively identifying demineralized areas of dental enamel and dentin with μ_s'. Combined with the polarisation, the hypertrophic scar[86, 87] and heart tissue[88] has been characterised by SFDI method.

We expect reduced scattering and absorption coefficient work jointly to interpret the structural and functional parameters of the target area. SFDI application has not yet extended to the surgical wound site monitoring. But based on various SFDI clinical application, we believe SFDI has great potential to characterise the surgical wound healing in a non-contact way.

1.2.5 SFDI modelling

For the surgical wound healing monitoring, identifying the wound margin is the key for wound structure measurement. For this purpose, we need to know how accurate SFDI could detect the position of the margin and determine optical properties for the wound-skin interface and surrounding area, as shown in the Fig. 1.6 (b). Thus, building up the mathematical and photon propagation model for SFDI method is the vital step.

The SFDI method provides significantly more information than the simple observa-

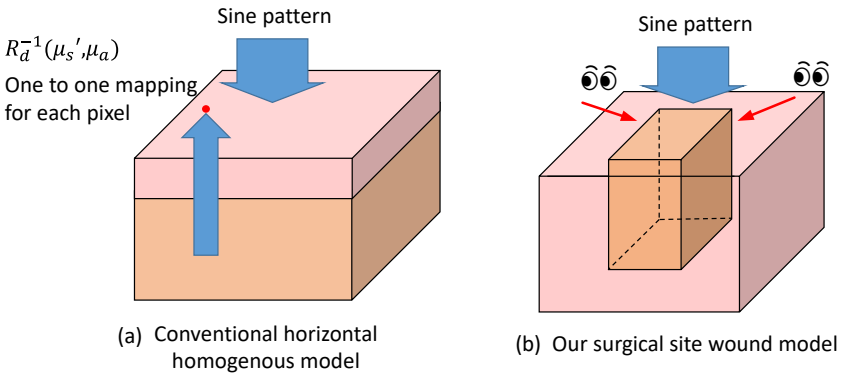

Figure 1.6: The tissue model in the conventional SFDI works compares to the model we explore in this thesis.

tion by naked eye into the detailed biological process that may be taking place on or below to the skin surface. Previous modelling works in SFDI has been targeted at measuring the optical properties of each pixel precisely from the diffuse reflectance R_d (see Fig. 1.6 (a)), based on single layer homogeneous model with variation occurring only with depth. People are working on better solution for the Radiative Transfer Equation (RTE) analytically or numerically. There are analytical solutions extended for two-layer tissue measurement[89, 90, 91]. The partial current boundary condition for the RTE function is utilized to upgrade the analytical solution[92].

In the numerical solution, diffuse reflectance R_d, the modulation transfer function (MTF) value of the tissue, is calculated by performing a Fourier transform to point spread function (PSF) (We will detail this in the Section 2.2.2.2). Hayakawa[93] determining the depth-dependent probability distributions in diffuse reflectance using a numerical method. ANN network was trained with two layer optical properties to provide the numerical solutions[94].

Regarding the error estimation work of the SFDI measurement, most of them are based on the homogeneous tissue model. Pera[95] used an ill-posed problem method combined with machine learning method to estimate the uncertainty in optical properties from the diffuse reflectance error. Tabassum[96] analysed the effect of instrument design into the SFDI's resolution. The source of SFDI error is

discussed with the input parameters and how it propagate into the results[97]. The error from the look up table (LUT) recovery method has also been analysed[98].

Due to the definition of PSF, the phantom must be symmetric in horizontal direction. However, there are no perfect homogeneous biological tissues as heterogeneity always exists in skin and this is further complicated when a wound is formed and healing taking place. SFDI method has rarely looked much into the heterogeneous effect on the SFDI resolution. The previous works are not sufficient for modelling the surgical wound structure.

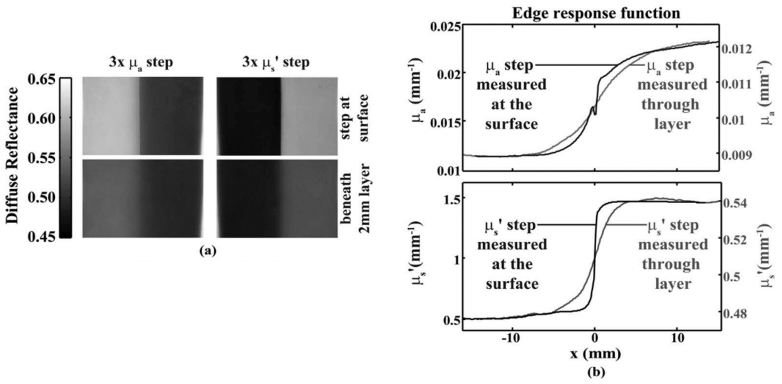

Figure 1.7: Two gelatin phantoms with a three times μ_a and μ_s' step for adjacent blocks separately. (a) The diffuse reflectance measured by SFDI. (b) The edge profile for the absorption coefficient μ_a and reduced scattering coefficient μ_s' are compared to the true value of the media. This picture is adapted from [6].

The edge response is known in the SFDI measurement due to the discontinuity in optical properties as shown in the Fig. 1.7. The different optical properties in adjacent points do have an effect and influence each other. Laughney et al[99] designed phantoms with vertical inclusions varying the scattering coefficient and radius to help determine the SFDI resolution in breast tumour surgery. Wirth et al[100] assembled phantom blocks having laterally different optical properties to analyse the edge function on scattering and absorption maps. They noticed the edge response at the boundary of heterogeneity limiting SFDI's lateral resolution but only conducted specific *ex vivo* tissue or phantom experiments without further modeling.

The reason behind is the partial volume effect[101] limiting the resolution of the imaging system at very small object or discontinuity in the optical properties. This effect has been found and corrected in the PET-CT and MRI[102, 103], but only be noticed for SFDI measurement result uncertainty[104, 105, 106]. For our purpose, this impact at the heterogeneous interface (i.e. the path of the surgeon's scalpel) needs to be closely investigated via diffuse reflectance and optical property maps for the wound.

1.3 Synopsis

In this thesis, chapter 2 covers the methodology of the SFDI method, introducing the optical property features of skin and explaining the principle behind the SFDI method. This Chapter gives a detailed guideline in using the SFDI method from capturing diffuse reflected images to recovering the optical properties step by step.

In chapter 3, we build up thee vertical heterogeneous tissue model of the SFDI method using a 3D Monte Carlo simulation. The sensitivity of SFDI method to detect the wound structure is discussed with the spatial frequency, wound reduced scattering coefficient and wound width. We also try a snapshot way for figuring out the change in the structure. The reason behind the sensitivity is explored with tracking the photon trajectory in the simulation.

Chapter 4 covers building and operation of the lab built SFDI instrument optimized for the wound healing application. This chapter then goes on to describe the phantom experiments to validate the modelling conclusions from Chapter 3. A resin sample are designed to mimic the wound model in the simulation.

Chapter 5 reports *in vivo* human tissue imaging experiments with the SFDI instrumentation built in chapter 4. The SLS irritation response of six volunteers, chronic eczema and biopsy wound healing are monitored by the SFDI system. The measurement results are discussed in the context of the known biological changes and the feasibility of SFDI system are evaluated for these conditions.

Chapter 6 proposes the future improvement plan for this approach in surgical wound healing monitoring.

Chapter 2

Methodology

2.1 Physics of scattering, absorption and Optical properties of human skin

2.1.1 Interaction between biological tissue and light

When light reaches human skin, Fresnel reflection and transmission occurs. The major light interactions with the tissue are absorption and scattering with the transmitted light. The reflection taking place on the top surface is negligible (around 4% to 7%)[24].

Absorption decreases the incident light intensity along the path of travel. The direction of the light propagating through the tissue remains the same after the absorption process. The absorption coefficient μ_a describing the effectiveness of absorption is defined as

$$\mu_a = -\frac{1}{T}\frac{\partial T}{\partial L} \tag{2.1}$$

where T is the transmitted fraction of the incident light after the path length ∂L. The light attenuation fraction can be calculated with the Beer-Lambert law[107]. For biological tissue the absorption effect is mainly due to the chromophores including melanin, oxy-hemoglobin, deoxy-hemoglobin, water and lipid.

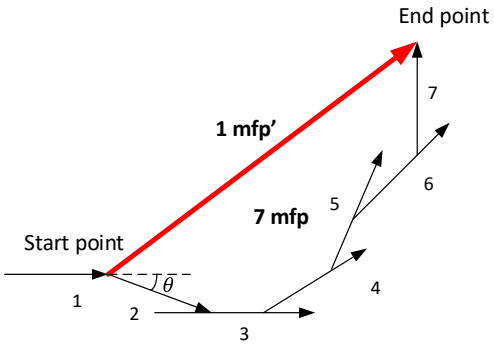

Figure 2.1: One reduced mean free path mfp' equal to, for example, seven small steps of the mean free path mfp. The θ is the deflection angle during the scattering event.

Scattering operates in a different way, changing the direction of the photon without consuming the energy of the light. Scattering can be considered a process of collision between photons and the particles on its path continuously removing intensity from the incident light and re-radiating it into different directions and not following the law of reflection[108].

The phase function $p(\theta)$ is used to describe the angular distribution of the re-radiating direction of a scattered photon where θ is the deflection angle from the photon's original forward trajectory. Anisotropy g is the expectation value of $cos(\theta)$ determined by measuring the scattering phase function $p(\theta)$. The scattering coefficient μ_s represents the concentration of scattering particles per volume in the media. The mean free path $mfp = \frac{1}{\mu_s}$ is the average path length the photon travels before getting involved in the next the scattering event. Multiple individual scattering steps can be extrapolated into one large displacement as shown in the Fig. 2.1. The incorporated one big step is the reduced mean free path $mpf' = \frac{1}{\mu_s'}$ where $\mu_s' = \mu_s(1-g)$. Thus, we have the reduced scattering μ_s' which is commonly used to describe the overall scattering effect of the light in tissue in the SFDI method.

2.1.2 Human skin optical properties

The optical properties of the skin are the parameters which describe the overall effect of light interaction with the skin. Here we review the human skin's absorption and scattering properties in the 400 nm - 1000 nm region as a guidence for the following simulation and experiment design.

The absorption property of skin is dependent on the skin chromophores which include blood, water, melanin and lipids[109]. In the visible (VIS) region (400 nm - 700 nm), the melanin and the hemoglobin dominate the absorption effect in human skin[24]. Melanin is contained in melaninsomes which lie in the epidermis providing a broadband absorption for the human skin decaying from the ultraviolet (UV) to infrared (IR) regions[110]. The volume fraction of the melaninsomes in the epidermis is from 1% in pale to 5% in darker skin[111].

The spectral graphs for blood content, melanin, water and lipid at the wavelength range 400 nm - 1000 nm are shown in the Fig. 2.2, Fig. 2.3 and Fig. 2.4 separately.

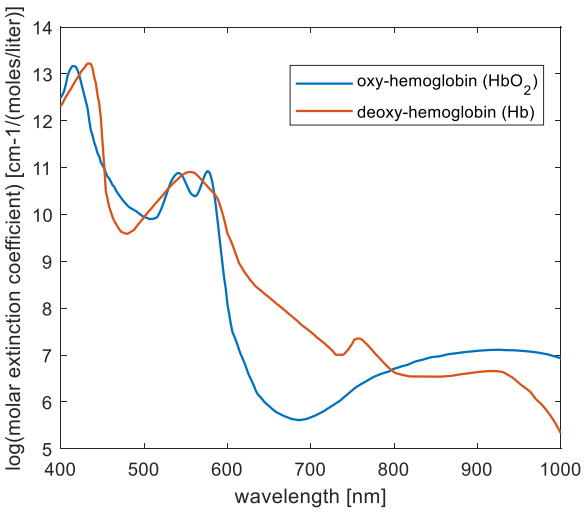

Figure 2.2: The molar extinction coefficient of the oxy-hemoglobin (HbO_2) and the deoxy-hemoglobin (Hb) in the blood in the 400 nm - 1000 nm range. The data points to draw this figure are adapted from [7, 8, 9]

The dermis is permeated with blood vessels where red blood cells contain hemoglobin making up 95% of its dry mass[21]. When the hemoglobin binds with oxygen,

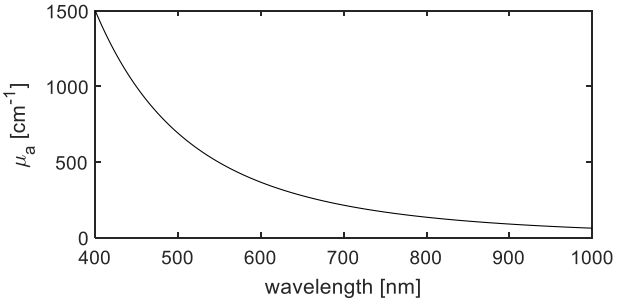

Figure 2.3: The absorption coefficient of the melanin in the 400 nm - 1000 nm range. The data points are adapted from [10].

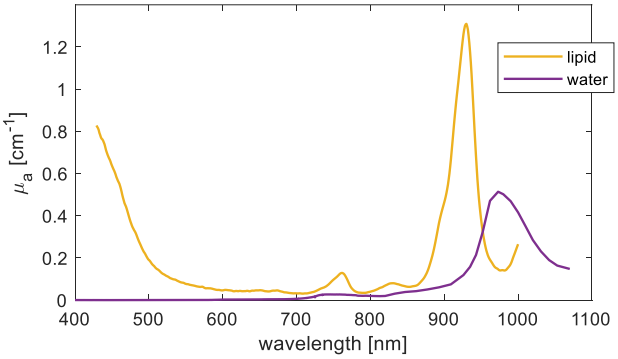

Figure 2.4: The absorption coefficient of the water and lipid in the 400 nm - 1000 nm range. The data points are adapted from [11, 12, 13].

it becomes oxy-hemoglobin (HbO_2) or it will stay as deoxy-hemoglobin (Hb). The total hemoglobin content (THC) present in blood content, can be measured with a single wavelength which is high in both absorption coefficient for HbO_2 and Hb. At 600 nm - 900 nm, either HbO_2 or Hb (see Fig. 2.2) dominates the absorption providing a spectral region to measure the oxygen saturation by using at least two wavelengths[112]. The melanin absorption is decreasing with the wavelength increase. Thus, using longer wavelength will benefit from this feature to detect deeper into skin. As water and lipid have low absorption coefficient there, this spectral range is suitable for quantifying hemoglobin-derived biomarkers. Longer IR wavelengths ($>$ 900 nm) are suitable for characterising the lipid (absorption peak 930 nm) and water (absorption peak 970 nm) content of the skin.

The scattering of the wound is related to the skin structure where the primary

scattering agent is the filamentous proteins[21]. In the epidermis, keratin is a filamentous protein formed inside the keratinocytes. In the dermis, collagen is the main scattering agent, here occupying 18% - 30% of the dermis volume[113]. The reduced scattering coefficient of the epidermis is significantly higher than the dermis[114]. However, the scattering effects from the epidermis have a small contribution to the overall skin μ_s' due to its thin depth.

The refractive index and the anisotropy g also influence the light propagation. From the previous work, the epidermis has a refractive index from 1.41 - 1.49 and the dermis is 1.39-1.41 in the VIS to IR range[115]. The anisotropy g value for the soft biological tissue is commonly taken as 0.9[116].

2.2 Spatial frequency domain imaging

2.2.1 Diffuse theory

Biological tissue is a turbid media where light transport in it is a stochastic process involving scattering and absorption. It can be modelled analytically using the Radiative Transfer Equation (RTE) (see Equ.2.2[117]) or via numerical solutions. The numerical method is more accurate but more computational intensive and time consuming. In this chapter, we will look at the analytical light transport model and the numerical solution will be discussed in Chapter 3.

The mathematical starting point for diffuse optics is the RTE function

$$\frac{1}{v}\frac{\partial L(\boldsymbol{r},\widehat{\Omega},t)}{\partial t}+\widehat{\Omega}\cdot\nabla L(\boldsymbol{r},\widehat{\Omega},t)=-\mu_{tr}L(\boldsymbol{r},\widehat{\Omega},t)+Q(\boldsymbol{r},\widehat{\Omega},t)+\mu_s\int_{4\pi}L(\boldsymbol{r},\widehat{\Omega}',t)f(\widehat{\Omega},\widehat{\Omega}')d\Omega' \tag{2.2}$$

where t stands for the time, v is the speed of the light in the media ($v=\frac{c}{n}$, where $c=3\times10^8$ m/s is the speed of the light, n is the refractive index of the media),

$\boldsymbol{r}$ is position and $\widehat{\Omega}$ and $\widehat{\Omega}'$ are the direction of incident light and scattered light separately.

The left-hand side of the equation represents the convective time derivative of the radiance from the light source. $L(\boldsymbol{r}, \widehat{\Omega}, t)$ is the light radiance, standing for the light power at position $\boldsymbol{r}$ time t per unit area heading in $\widehat{\Omega}$ direction. The right-hand side of the equation is formed of the loss within the media due to the absorption and scattering, the gain from the light source in the incident direction $\widehat{\Omega}$ and the diffuse scattering light into the direction $\widehat{\Omega}'$. $f(\widehat{\Omega}, \widehat{\Omega}')$ is the probability function for the incident light in $\widehat{\Omega}$ direction, scattering into the direction $\widehat{\Omega}'$. μ_{tr} is the transport coefficient given by $\mu_{tr} = \mu_a + \mu_s'$, and $\mu_{eff} = \sqrt{3\mu_a\mu_{tr}'}$. The μ_a is the absorption coefficient and the μ_s' is the reduced scattering coefficient where $\mu_s' = \mu_s(1-g)$, g is the anistropy.

To begin with, here we will briefly review the simple conceptual framework of the diffuse light interaction with ideal biological tissue assumption. We will discuss the RTE solution via numerical method for more realistic situation in Chapter 3.

The analytical solution can be derived from approximation for specific conditions. Regarding a homogeneous and semi-infinite biological tissue the diffuse approximation of the RTE is

$$\nabla^2\varphi - \mu_{eff}^2\varphi = -3\mu_{tr}q \tag{2.3}$$

where the φ is the fluence rate, q represents the illumination source. For the SFDI, the light source is a 1D sine pattern given as

$$q = q_0(z)cos(k_x x + \alpha) \tag{2.4}$$

where k_x is the wavenumber, $q_0(z)$ is the amplitude of the projected sine pattern and α is the spatial phase of the pattern. The sine pattern is modulated in the x direction with the spatial frequency of $f_x = k_x/2\pi$. Assuming the biological tissue is a linear media, for a wave propagating into the tissue the lateral phase and the spatial frequency stays constant as the projected sine pattern. Thus, we have the

fluence rate as

$$\varphi = \varphi_0(z)cos(k_x x + \alpha) \tag{2.5}$$

By taking Equ. 2.4 and Equ. 2.5 into the Equ. 2.3, the 1D second order Helmholtz equation is written as

$$\frac{d^2}{dz^2}\varphi_0(z) - \mu_{eff}'^2\varphi_0(z) = -3\mu_{tr}q_0(z) \tag{2.6}$$

where the scalar attenuation coefficient μ'_{eff} is given as

$$\mu'_{eff} = \sqrt{\mu_{eff}^2 + k_x^2} \tag{2.7}$$

Equ. 2.6 represents scalar photon density wave attenuation via depth z in biological media, equal to the planar illumination for Equ. 2.3. The effective penetration depth l of the sine pattern can be calculated with

$$l = \frac{1}{\mu'_{eff}} \tag{2.8}$$

2.2.2 Inverse method

Using diffusion theory to predict the diffuse reflectance $R_d(f_x)$, i.e. tissue's spatial modulation transfer function (s-MTF), with a known set of (μ_a, μ'_s, g, n) is the forward process. Conversely, solving the optical properties from the $R_d(f_x)$ is the inverse process which is what SFDI targeting to do. The inverse process is in need of a very large database of $R_d(f_x)$ data to recover the optical properties from biological tissue. Two inverse methods are normally considered including the analytical method by applying the boundary condition to the Equ. 2.6 and the look up table (LUT) method.

2.2.2.1 Multi-frequency fitting

The attenuation coefficient μ'_{eff} depends on the spatial frequency f_x and the optical properties of tissue. Adding the derivation of the planer photon density wave reflectance[118], the extended source can be written as

$$q_0(z) = P_0\mu'_s exp(z) - \mu_{tr}z \tag{2.9}$$

where P_0 is the power of the light source. Taking this into the Equ. 2.6, the fluence rate via depth z is

$$\varphi_0(z) = \frac{3P_0a'}{\mu'^2_{eff}/\mu^2_{tr} - 1}exp(-\mu_{tr}z) + Cexp(-\mu'_{eff}z) \tag{2.10}$$

where $a' = \frac{\mu'_s}{\mu_{tr}}$ is the reduced albedo, C is the constant value related to the choice of boundary condition. Following partial current boundary condition the flux j[119] is set proportional to the fluence at the interface z = 0 $j|_{\to 0^+} \equiv \frac{-\nabla|\varphi_{z\to 0^+}}{3\mu_{tr}}$. Then the diffuse reflectance $R_d(f_x)$ is given as

$$R_d(f_x) = \frac{j|_{\to 0^+}}{P_0} = \frac{3Aa'}{(\frac{\mu'_{eff}}{\mu_{tr}} + 1)(\frac{\mu'_{eff}}{\mu_{tr}} + 3A)} \tag{2.11}$$

where the proportionality constant $A = \frac{1-R_{eff}}{2(1+R_{eff})}$, and the effective reflection coefficient: $R_{eff} \approx 0.0636n + 0.668 + \frac{0.710}{n} - \frac{1.440}{n^2}$ where n is the refractive index. Therefore Equ. 2.11 is spatial frequency f_x dependent according to the definition of the μ'_{eff}. Two optical properties μ'_s and the μ_a can be recovered by applying multiple measured $R_d(f_x)$ values and their f_x values to the Equ. 2.11 with a fitting algorithm method.

The Equ. 2.3 also matches the low-pass filter feature of the biological tissue. When the k_x (spatial frequency $f_x = k_x/2\pi$) increases, the ratio between the $\frac{\mu'_{eff}}{\mu_{tr}}$ increases leading to the R_d value decreasing.

2.2.2.2 2D look up table

Another effective inverse method is using a look up table (LUT) with fine grid $R_d(f_x)$ formed by a wide range of reduced scattering μ_s' and absorption μ_a coefficients. As the μ_s' and μ_a is of two degrees of freedom, the LUT is required to be 2D by two different spatial frequencies' R_d. This requires a large number of calculations in advance to predict the $R_d(f_x)$ value. However, this helps significantly in reducing the number of spatial frequencies measurements. The μ_s' and μ_a are then retrieved by pairing two calculated $R_d(f_x)$ values to the 2D look up table as shown in the Fig. 2.5.

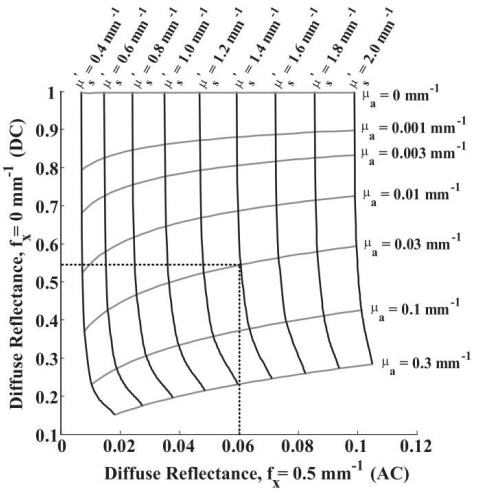

Figure 2.5: There is an example for using the look up table method for recovering the reduced scattering and absorption coefficient. We will pair two R_d values at two f_x to the point in the table and then obtain the optical properties.

As $\mathrm{R}_d(f_x)$ serves as the MTF of the biological tissue, we can predict it via the spatial point spread function (s-PSF) $R_d(\rho)$. Based on the assumption of an infinite width homogeneous tissue, the Fourier transformed s-PSF is the MTF. The impulse response of the biological tissue is easy to obtain with projecting a narrow radius collimated beam onto the tissue in a Monte Carlo simulation. Then $\mathrm{R}_d(k_x)$ ($k_x = 2\pi f_x$) is written as

$$R_d(k_x) = 2\pi \int \rho_i J_0(k_x \rho_i) R_d(\rho_i) d\rho_i \tag{2.12}$$

where the $J_0(k\rho_i)$ is the zeroth-order Bessel function of the first kind. The simulation process is discrete where ρ is binned in the interval $\Delta\rho_i$. Therefore Equ. 2.12 used in practice to calculate $\mathrm{R}_d(k_x)$ is given by

$$R_d(k_x) = 2\pi \sum_{i=1}^{n} \rho_i J_0(k_x \rho_i) R_d(\rho_i) \Delta\rho_i \tag{2.13}$$

2.2.3 Illumination, Acquisition and Calibration

In practice, an ideal sinusoidal intensity profile cannot be projected as it contains negative values. The pattern intensity S in the x direction is formed by

$$S = \frac{S_0}{2}[1 + M_0 cos(2\pi f_x x + \alpha)] \tag{2.14}$$

where the S_0 is the intensity of the light parameter of light source, M_0 is the modulation depth and α is the spatial phase.

The geometry of a SFDI system is shown in the Fig. 2.6, where three phases of sinusoidal pattern for each f_x at 0 rad, $\frac{2\pi}{3}$ rad and $\frac{4\pi}{3}$ are projected onto the top surface of the tissue. The back scattered light from each projection is captured separately as I_0, I_1, I_2. The three phases conduct sampling at every point on the tissue that is illuminated.

The captured back scattered light is the sum of an alternating component (AC) I_{AC} and a direct component (DC) I_{DC}. The I_{AC} can be described as

$$I_{AC} = M_{AC}(x, f_x) cos(2\pi f_x x + \alpha) \tag{2.15}$$

where the M_{AC} is the amplitude of the AC image encoding the biological optical properties which is the key of SFDI measurement. The DC image amplitude, M_{DC}, is the tissue response to the uniform light projection. The M_{AC} can be calculated as

$$M_{AC}(x, f_x) = \frac{\sqrt{2}}{3}\sqrt{(I_1 - I_2)^2 + (I_1 - I_3)^2 + (I_2 - I_3)^2} \tag{2.16}$$

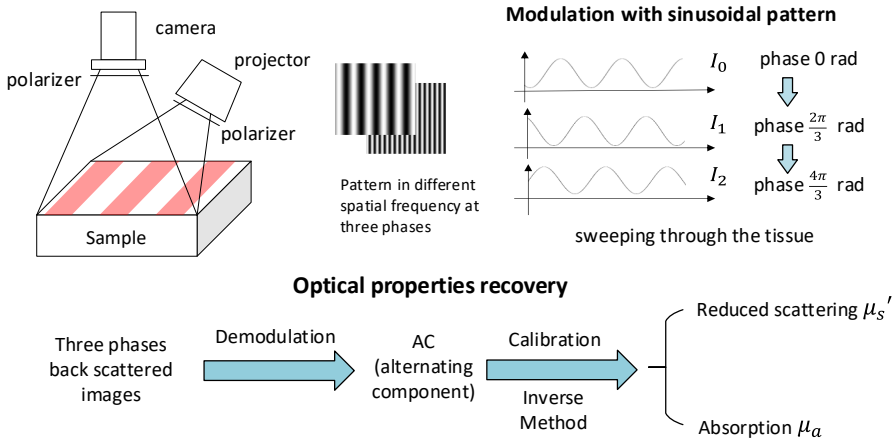

Figure 2.6: (a) The geometry of the SFDI system and data flow of the optical properties recovery.

whereas M_{DC} can be obtained as

$$M_{DC}(x, f_x) = \frac{1}{3}(I_1 + I_2 + I_3) \tag{2.17}$$

In the frequency domain, the M_{AC} is composed of the light source intensity S_0, the MTF_{system} of the imaging system itself and the MTF of the tissue using equivalent theoretical $\mathrm{R}_d(f_x)$ in theory:

$$M_{AC}(x, f_x) = S_0 \cdot MTF_{system} \cdot R_d(x, f_x) \tag{2.18}$$

To obtain the $R_d(f_x)$ of a target sample, a calibration sample with known optical properties is imaged under the same imaging condition and same spatial frequency f_x. The $R_d(f_x)$ of the target biological sample can be obtained by

$$R_d(x, f_x) = \frac{M_{AC}(x, f_x)}{M_{AC,pred}(x, f_x)} R_{d,pred}(x, f_x) \tag{2.19}$$

where the $M_{AC,pred}(x, f_x)$ is calculated from the three-phase image from the calibration sample, and $M_{AC,sample}(x, f_x)$ is calculated from the three-phase image of target sample. The $R_{d,pred}(f_x)$ is predicted by the Monte Carlo method with calibration sample's μ_a and μ_s' value.

2.3 Conclusion

In this chapter, we firstly reviewed the human skin parameters and the light interactions with the biological tissue. The key using the SFDI method to measure the biological tissue is to recover two optical properties: reduced scattering coefficient μ_s' and the absorption coefficient μ_a. Here we learn μ_s' changes the direction of the light propagation while μ_a reduces the intensity. Then we introduce the principle of the SFDI including the analytical and numerical solution behind, the instrumentation design and inverse method. We know the analytical method has more limitations with the prior parameters than the numerical one. In the following chapter, we will use the numerical method to concentrate on SFDI's ability to monitoring the surgical wound.

Chapter 3

Monte Carlo simulation

3.1 Overview

To observe the surgical wound healing process, the structure and optical properties of the tissue are important indicators and studying the time course change of them will provide insight into that wound healing process. For the surgical wound, we also need to consider the impact of the skin and wound interface in the absorption and scattering coefficient measurement to understand how accurately and reliably SFDI can determine the change in the optical properties and structure change.

As discussed in the Chapter 1 and 2, analytical solution for the SFDI is not a suitable approach for our surgical wound imaging purpose as it is limited to the assumption of homogeneous tissue model (when $\mu_s' >> \mu_a$). At the same time, conventional numerical solution for obtaining the diffuse reflectance via the point collimated beam also breaks down, because the Fourier transform from the PSF to MTF is only valid for the homogeneous tissue model.

In order to accurately model the heterogeneity, we will need to select the optimal numerical method. Most commonly the light propagation in has been simulated via Monte Carlo simulation[120] and recently Finite element method (FEM) is adapted to SFDI forward modelling[121, 122].

The Monte Carlo method is a computational tool using repeated random exper-

iments to determine the value expected based on the law of large numbers. The Monte Carlo method was first introduced to solve the laser interactions within biological tissue by Wilson et al[123]. In the simulation, numerous number of photons conduct random walk individually to travel in the biological tissue with the step size and angular deflection statistically selected with random number generator. It was further developed[120, 124, 125, 126, 127, 128] to become a powerful tool for obtaining the numerical solution for light transportation in turbid media. Though with more computational cost, the input tissue parameters can be widely varied to simulate multiple possible tissue conditions.

FEM simulates the light propagating by discretising the diffuse equation by comprising small interconnected tiny sub regions [56, 129]. Proposed by Dehgani et al[122, 130] in 2009, this method has been successfully applied for diffuse optical tomography (DOT) image reconstruction for mapping internal optical properties for breast cancer[131, 132, 133] and brain function imaging[134, 135]. The FEM method is recently adapted to SFDI simulation with projecting the sine pattern directly to the biological tissue by NIRFAST tool[136]. However, future work is required to improve the FEM method in reducing the boundary error in simulation.

Therefore, the Monte Carlo method is with better accuracy and widely applied for the SFDI simulation. Thus, we are utilising the Monte Carlo simulation in this thesis. In this chapter, we apply the Monte Carlo method not only to simulate a homogeneous tissue model for sensitivity testing but also to determine a "pattern" in the result. The sensitivity of SFDI to characterise the difference in the reduced scattering will be investigated with various wound width and optical properties input in the simulation. Based on the results we discuss the strength and limitation of SFDI for wound healing.

3.2 Monte Carlo algorithm

The flow chart for the basic Monte Carlo method[120] is shown in the Fig. 3.1. Each individual photon follows this flow chart propagating within the tissue independently.

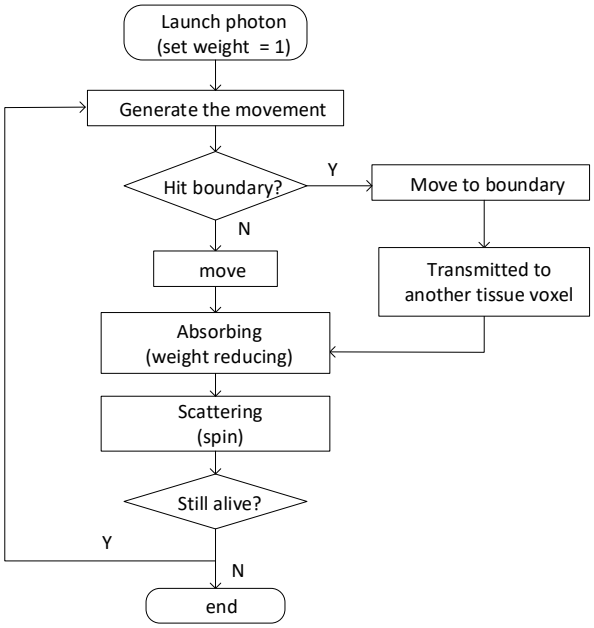

Figure 3.1: The flow chart of the Monte Carlo simulation for individual photon.

The photon is launched at a certain position on the top surface of the tissue assigned with a initial weight $W = 1$ and direction of movement is down in the z direction. In the computing loop, the position of the photon at the current step is (x, y, z). The step size s of each step is calculated based on sampling the probability distribution for the photon free path

$$s = -ln(\xi)/\mu_{tr} \tag{3.1}$$

where ξ is a random number generated uniformly between 0 and 1 (inclusive).

Before the movement of the photon, we check the distance d_b between the photon and the nearest boundary, i.e. the new voxel of the starting position and the

boundary for the tissue. If movement in the next step means the photon will not hit the boundary, it will be moved directly with the distance s. The update for the photon position is

$$\begin{aligned} x &= x + u_x s \\ y &= y + u_y s \\ z &= z + u_z s \end{aligned} \tag{3.2}$$

where the u_x, u_y and u_z are the cosines value of the angle between the direction vector and the coordinate axes. If the boundary is in the way, we move and transmit the photon just across the boundary into the adjacent voxel.

After the movement, the absorption along the path is calculated with

$$\Delta W = W exp(-\mu_a s) \tag{3.3}$$

Then the updated weight of the photon is

$$W = W - \Delta W \tag{3.4}$$

After the tally for the absorption, the photon is scattered with the deflection polar angle θ generated by the Henyey-Greenstein function [137].

$$p(cos\theta) = \frac{1 - g^2}{2(1 + g^2 - 2gcos\theta)^{3/2}} \tag{3.5}$$

As the g value for the biological tissue is normally 0.9, the cosine of the deflection angle θ is

$$cos\theta = \frac{1}{2g}[1 + g^2 - \frac{1 - g^2}{1 - g + 2g\xi}] \tag{3.6}$$

The azimuthal angle ϕ for the photon scattering is sampled uniformly over a range of 0 to 2π by

$$\phi = 2\pi\xi \tag{3.7}$$

where ξ is the generated random number between 0 and 1.

After the scattering process, the new direction vector of the next movement is updated as

$$\begin{aligned} u_x &= \frac{sin\theta(u_x u_z cos\phi - u_y sin\phi)}{\sqrt{1-u_z^2}} + u_x cos\theta \\ u_y &= \frac{sin\theta(u_y u_z cos\phi + u_x sin\phi)}{\sqrt{1-u_z^2}} + u_y cos\theta \\ u_z &= \sqrt{1-u_z^2} sin\theta cos\phi + u_z cos\theta \end{aligned} \tag{3.8}$$

The photon will be checked to see if it is 'alive' based on the position and the final weight after the above process is finished. If the position of the photon is outside the tissue, the photon is 'dead' immediately. When the position of escape is above the top surface, the final weight of it will be collected into the back scattered light $I(x, y)$ where (x,y) is the position the photon escapes at the surface.

While the photon still remains in the tissue, the weight of the photon is compared with a threshold. If the weight is lower than the threshold, the unbiased termination will be utilised on the photon. We play Russian roulette[138] to improve the simulation efficiency but also consider the likelihood a photon might live long but only make a minor contribute to the final results. The photon will be terminated at the probability $\xi > m$ where ξ is the random number between 0 and 1. Otherwise it will have its weight increased by $1/m$ to stay 'alive' representing the likelihood.

$$W \leftarrow \begin{cases} \frac{1}{m}W & \text{if } \xi \leq m \\ 0 & \text{if } \xi > m \end{cases} \tag{3.9}$$

3.3 Homogeneous skin model

In this section we will look at the sensitivity of SFDI in detecting changes in the optical properties in the biological media. We apply the MCCL package[139] (version 4.9.0 Beta, downloaded in 13/03/2020). A point collimated beam is projected onto the infinite one-layer homogeneous tissue. As discussed in the Section 2.2.2.2, diffuse reflectance can be obtained by the Equ. 2.13.

The tissue model is expanded infinitely in the x and y directions with a depth of 16 mm in the z direction applying 3,000,000 photons per simulation. The z depth for the model guarantees the photons cannot escape from the bottom of the tissue while saving on computational cost[93]. The homogeneous skin models are assigned with multiple pairs of μ_s' and μ_a where the μ_s' is changed from 0.473 mm^{-1} to 4.73 mm^{-1} with the linear interval 0.473 mm^{-1}. The refractive index of the biological tissue is set to be fixed at $n = 1.42$ and anistropy $g = 0.9$[24]. The f_x range is from 0.05 mm^{-1} to 0.35 mm^{-1} with a gap of 0.05 mm^{-1} covering the most commonly used spatial frequency ranges in the SFDI method.

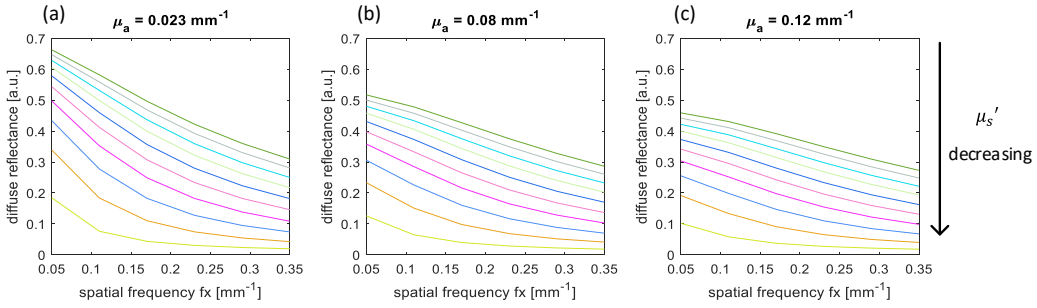

Figure 3.2: The normalised diffuse reflectance at same μ_s' with three μ_a 0.023 mm^{-1}, 0.08 mm^{-1} and 0.12 mm^{-1} separately. The curves from top to bottom are with the μ_s' value decreasing.

The simulations are run for μ_a for 0.023, 0.08 and 0.12 mm^{-1} and their results are demonstrated in the Fig. 3.2. When μ_a increases, the intensity of the diffuse reflectance R_d decreases which matches the Beer-Lambert law. When μ_s' increases, the intensity of the R_d increases. The distance between each curve at the same μ_a

and low f_x value range (approximately < 0.25 mm^{-1}) are not identical indicating the difference of SFDI sensitivity for detecting the changes in μ_s'. The same interval in the μ_s' value yields greater change in the R_d intensity when the reduced scattering is lower. Also, the SFDI is sensitive to the μ_s' change when the f_x is lower in the value. In this way, SFDI can capture the changes in μ_s' more easily when f_x and μ_s' is both low.

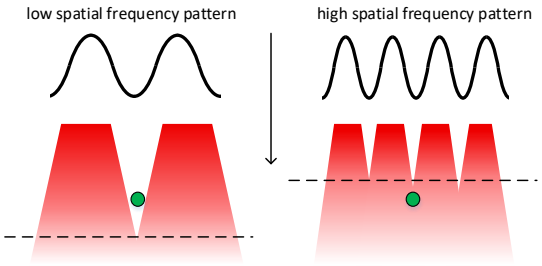

Figure 3.3: The pattern propagation within the low pass filter biological tissue [14]. The different spatial frequency pattern can reach different depth.

In the low f_x value range, the intensity of R_d is always relatively higher due to the low pass filter feature of the biological tissue. As illustrated in the Fig. 3.3, the lower spatial frequency pattern (wide stripe pattern) can penetrate further down in the biological tissue while high spatial frequency pattern (fine stripe pattern) gets blurred at a shallow depth. The back scattered light $I(x, y)$ from the low spatial frequency pattern has better contrast as most of photons are travelling down further. Conversely the back scattered light from the high spatial frequency pattern has low contrast as the photons are more likely to "bounce" back and escape at top surface.

Comparing the Fig. 3.2 (a), (b) and (c), the trends of R_d sensitivity to the μ_s' value change with respect to three μ_a values are similar. The change in the absorption does not add much effect on the trend. As we discussed in the previous chapter, μ_a only reduces the intensity linearly with the value and is easy to predict with the Beer-Lambert law. Also, the μ_a value at 0.12 mm^{-1} is covering the maximum value for the illumination wavelength range (600 nm to 850 nm)[140] we are using for the human skin *in vivo* measurement. At the same time, the reduced scattering

change is non-linear with the value change is highly related to the wound structure. Therefore, we can concentrate on SFDI detection sensitivity change via the μ_s' assuming the absorption is constant. We will discuss this in Section 3.5.

3.4 3D Monte Carlo simulation

For wound modelling, we use the 3D Monte Carlo simulation algorithm in a typical structure of surgical wound model as shown in the Fig. 3.7. Our code is based on the *mcxyz*[127] (version July 22, 2019, downloaded in 10/06/2020) supporting the customized tissue structure assigned with optical properties. To overcome the shortcoming of the analytical and conventional method, obtaining the MTF from PSF, the three phases sine pattern are projected to the top surface of the model directly. Our 3D Monte Carlo simulation is designed to have two outputs. One is the diffuse reflectance R_d (the tissue's MTF) from the three phases back scattered light. This will aid us with obtaining more accurate results from the heterogeneous model. As the 'imaging system' are perfect in the simulation, the AC image intensity I_{AC} calculated from simulation results is equal to the R_d of the tissue.

The other output is recording the photon trajectory within the phantom as shown in the Fig. 3.4. We insert non-destructive detector planes at regular intervals (we use the bin size in z direction for the interval), to record the depth–dependent weight $W_{up}(z)$ and $W_{down}(z)$ within the tissue, as shown in the Fig. 3.4, for the photon moving back up through the tissue or down respectively. The two outputs give the overall trajectory of the photon within the tissue to help with understanding the R_d intensity profiles as well as monitoring the photon behavior at the wound and skin edge. When the photon moves to a new voxel, the weight of the photon will be updated and recorded subsequently by the detector planes. The upward facing detector will record the current weight of the photon travelling down through the tissue, where the cosine value of the angle between the direction vector and z axes

of the coordinate is over 0 (shown in the Fig. 3.4). Similarly, a photon going up will be recorded by the bottom face.

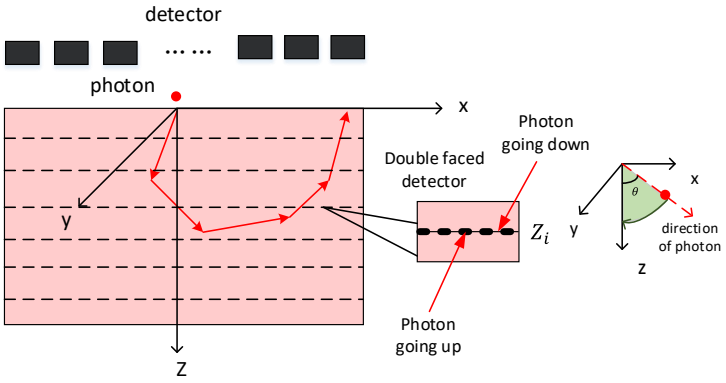

Figure 3.4: The geometry of recording the photon trajectory.

The simulation is conducted in the Cartesian coordinate system. The basic unit of the simulation is a 3D cube-shaped voxel with the assigned bin size in x, y, z direction. The size of the bin is the resolution of the photon movement detection, equal to the pixel in the detector. In this chapter, the bin size is chosen to be 0.02 mm in all three directions to balance the signal noise ratio (SNR) and the computational cost.

3.4.1 Photon propagation

To better understand the result from Section 3.3, we project the sine pattern onto the top surface of the homogeneous tissue model with three μ_s' values of 0.473, 1.42 and 4.73 mm^{-1} separately and at $f_x = 0.25$ mm^{-1}. The absorption is selected as 0.023 mm^{-1} and the refractive index n = 1.42. The wound depth is set as 16 mm as same as in Section 3.3. The $Weight_{up}$ and $Weight_{down}$ are recorded when simulating the back scattered light $I(x, y)$ profile. We slice the yz plane at the x = 0 for the weight profile to observe the photon trajectory as shown in Fig. 3.5 (g). The profiles are shown in depth(z) range from 0 mm to 8 mm to highlight the sine pattern propagation. Their back scattered light images $I(x, y)$, are shown in the Fig. 3.6 for x range -14 mm to 14 mm and y range -10 mm to 10 mm.

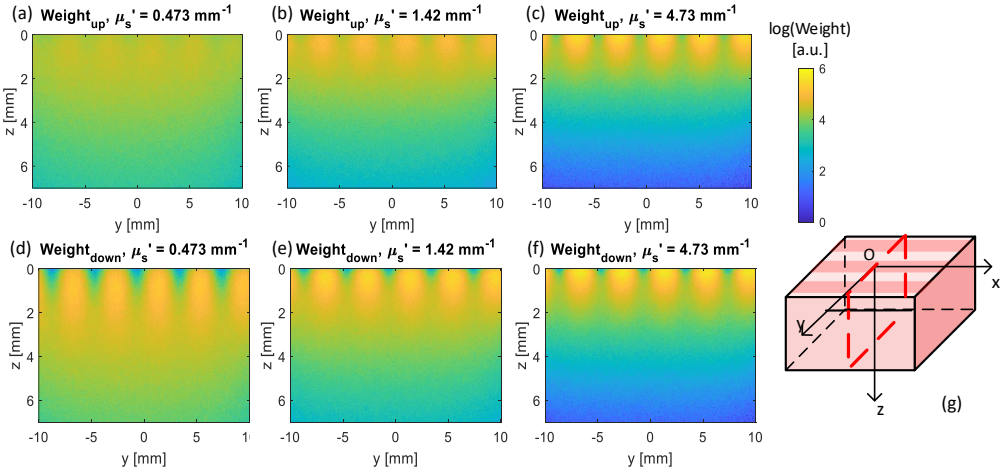

Figure 3.5: The variation of pattern intensity with depth and scattering from photon distribution. (a) and (d) are the low scattering wound yz plane slices; (b) and (e) are the healthy skin yz plane slices; (c) and (f) are the high scattering wound xz plane slices. (g) Slicing the $Weight_{up}$ and $Weight_{down}$ at x = 0 to obtain the profile at yz section.

A photon is capable of travelling further in the lower scattering media while photons keep "bouncing" near the top surface in the high scattering media. With the reduced scattering μ_s' value increasing in the media, the photons are redirected more frequently by short step sizes (reduced mean free path $l' = 1/\mu_s'$) hence reemerging closer to the top surface where they have been launched[98]. Comparing the $Weight_{down}$ for three types of tissue model, the penetration depth of the sine pattern decreases progressively with μ_s' increasing according to Fig. 3.5 (d), (e) and (f) as expected. Consequently, in the $Weight_{up}$ profiles shown in the Fig. 3.5 (a), (b) and (c), there are fewer photons travelling back to the top surface when the μ_s' value is low.

Thus, as shown in the Fig. 3.6, the $I(x, y)$ image of a low scattering media illustrates blurred stripes. Conversely, the high scattering results demonstrate a sharp contrast $I(x, y)$ image. In this way, the high scattering media has a relatively high intensity diffuse reflectance R_d profile matching the simulation results in the Section 3.3.

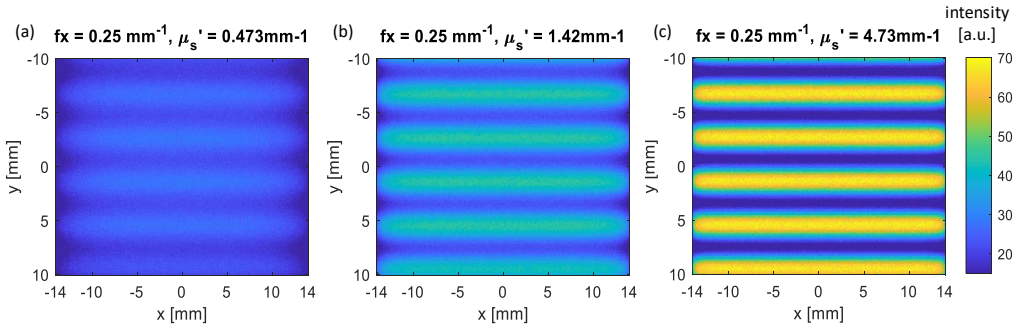

Figure 3.6: The back scattered light $I(x, y)$ of three different μ_s' phantoms.

3.5 Single layer surgical wound model

During surgery, the incision will be made through skin to access the operation site. At the end of the procedure, the skin and underneath tissue is sealed with the suture, steri-strips or glue forming a vertical wound embedded in the tissue. Here we assume both skin and vertical wound are homogeneous in their optical properties, the 3D tissue model is built as shown in the Fig. 3.7.

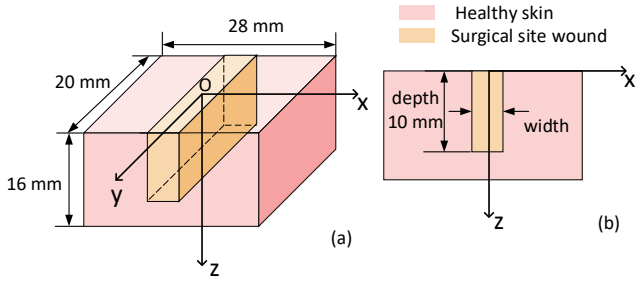

Figure 3.7: (a) The 3D structure of the surgical site wound. (b) The xz section of the tissue.

The healthy skin and the surgical site wound block are assigned with their own optical properties. The height width and the length are chosen as 16 mm, 20 mm and 28 mm. With the bin size of each voxel, the resolution in three dimensions are 800, 1000 and 1400 pixel accordingly. As discussed in the section 3.3, the absorption impact is easy to predict and we are more focused on the change in scattering. The absorption of the wound model is kept the same at 0.023 mm^{-1} from the empirical

skin optical parameters. The anisotropy g is 0.9 as a common value for biological tissue[24]. The skin has the empirical skin μ_s' at 1.42 mm^{-1}[141]. Three phases (0 rad, $\frac{2\pi}{3}$ rad and $\frac{4\pi}{3}$ rad) of sine patterns are projected to the tissue top surface. The AC image intensity I_{AC} of each spatial frequency is calculated utilizing the Equ. 2.15.

In the following text, we are using the AC image instead of R_d to described the diffuse reflectance R_d results obtained from the simulation. In the simulation here, the MTF_{system} is always 1 as it has perfect optical transmission chain from the light source to the tissue surface. In the practice, diffuse reflectance R_d image is calibrated AC image from the SFDI system.

3.5.1 Orientation of the sine pattern projection

In the previous SFDI work, people haven't considered the sine pattern orientation as they assumed the tissue is homogeneous. However, the discontinuity at the wound-skin boundary can affect the photon trajectory hence influence the accuracy of the AC images to map the heterogeneity.

To simplify the observation of changes in wound structure with the intensity of the AC image I_{AC}, here we formulate a 1D AC profile for the wound. When looking at a small wound site area in our model, we can assume the wound and skin region are each locally uniform with respect to their own optical properties. Therefore, we determine $I_{curve,AC}$ by averaging the intensity of the AC image along the y direction as in Equ. 3.10 where N_y is the number of pixel in the y direction which direction the sine pattern is orthogonal to as shown in the Fig. 3.8 (a). This helps to reduce the number of the photons that are launched into the original model as well as averaging random noise in the Monte Carlo method.

$$I_{curve,AC}(x) = \frac{1}{N_y} \sum_{y} I_{AC}(x, y) \tag{3.10}$$

To determine the best orientation to project the sine pattern, we model both parallel and orthogonal sine patterns to the wound as shown in the Fig. 3.8. The two projections are applied to the same wound model and wound widths are selected to be 1 mm or 4 mm with the reduced scattering of the wound area $\mu'_{s,wound} = 0.473\ \text{mm}^{-1}$ and $4.73\ \text{mm}^{-1}$ respectively. The sine pattern with spatial frequency $f_x = 0.15\ \text{mm}^{-1}$ is projected at two direction to the same wound model at three phases separately to obtain the AC images.

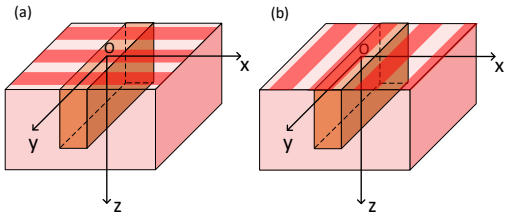

Figure 3.8: The geometry of projecting the sine pattern (a) orthogonal to the wound (b) parallel to the wound.

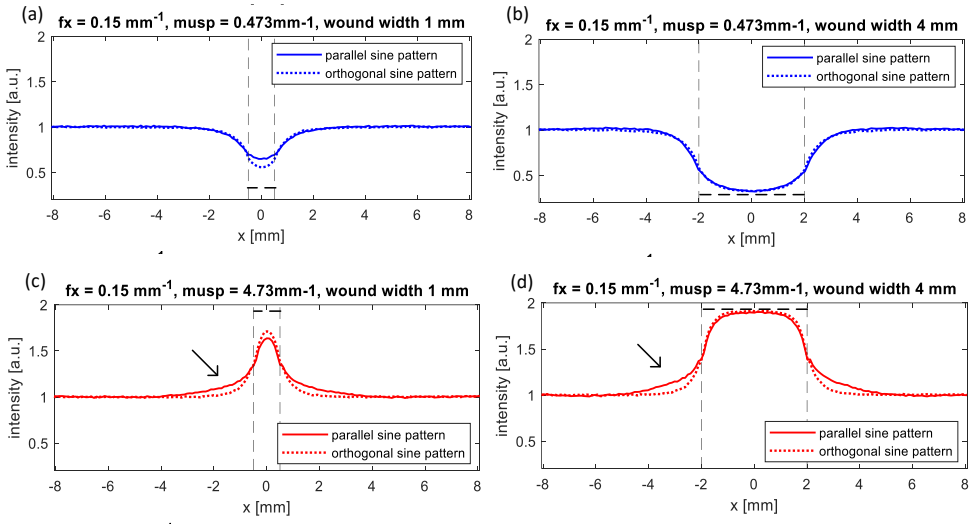

Figure 3.9: The $I_{curve,AC}$ of the wound $\mu'_s = 4.73\ \text{mm}^{-1}$ with two type of projection. The curves are all normalised to the same skin intensity level. Two vertical dashed lines mark the wound area inside. The horizontal dashed line is the ideal intensity of the wound area when the tissue is homogeneous with same μ'_s parameters.

The $I_{curve,AC}$ are calculated and plotted in the Fig. 3.9. For orthogonal pattern, the $I_{curve,AC}$ is calculated by averaging I_{AC} through the y direction and the I_{AC}

of parallel pattern is averaged by x direction. The wound area is located between the black dashed lines. The structure of the wound are both exaggerated in the $I_{curve,AC}$ by the two ways of sine pattern projection. The AC images from the orthogonal sine pattern projection provides a more similar shape to the wound than the parallel sine pattern projection. This matches previous works[5, 99, 142], where the edge response exists and introduces an error in determining the real shape of the heterogeneity. The parallel sine pattern even increases the intensity of the skin area near the wound (see the arrow pointing on in Fig. 3.9). Also the wound centre intensity value from the orthogonal sine pattern, particularly of the 1 mm wound, is much closer to the homogeneous wound level. (The reason behind why the wound centre intensity for the narrow wound is lower than the homogeneous wound model will be discussed in the Section 3.5.3.)

Therefore the orthogonal sine pattern is selected as it better aids in identifying the structure and optical properties. To look into this closely, we track the photon trajectory for the 4 mm wound model with wound $\mu_s' = 4.73$ mm^{-1}. The $Weight_{down}$ profiles sliced in xz section for parallel projection and in yz section for orthogonal projection shown in Fig. 3.10.

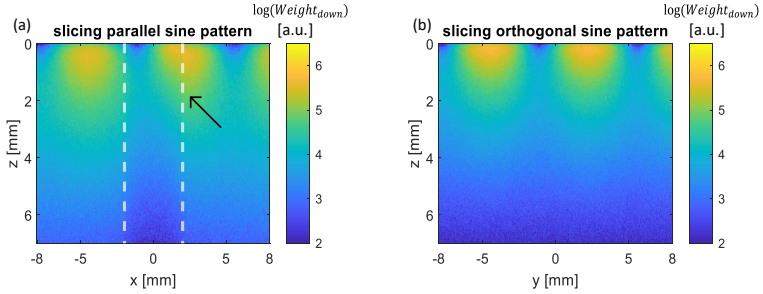

Figure 3.10: (a) The $Weight_{down}$ slicing at y = 0 mm for the parallel sine pattern projection. The white dashed lines indicate the wound inside. (b) The $Weight_{down}$ slicing at x = 0 mm where the $\mu_s' = 4.73$ mm^{-1} (wound area) for the orthogonal sine pattern projection.

The edge effect at the wound-skin boundary in the parallel projection is more evident not only due to the response at the μ_s' discontinuity but also adding on disruption effect to the sine pattern. The distinctive μ_s' change at the wound-

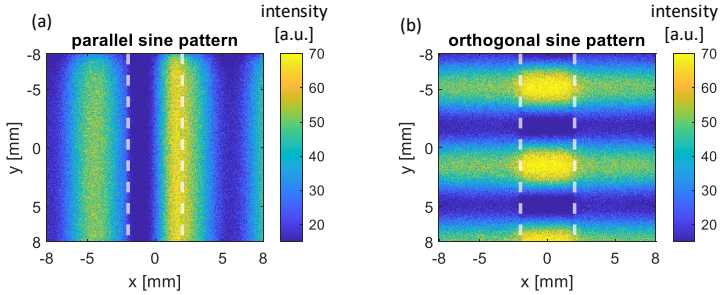

Figure 3.11: The back scattered light of (a) parallel pattern projection (b) orthogonal pattern projection. The spatial frequency f_x for both sine pattern is 0.15 mm^{-1}. The white dashed lines indicate the wound area between them.

skin edge results in more uncertainty to the AC image making the photons have additional horizontal migration. This leads to the exaggeration in the solid line (parallel sine pattern projection) illustrated by the black arrow in the Fig. 3.11. Any other orientation of the sine pattern projection (except the orthogonal one) still suffers from the same effect as it always has the portion contributing to this direction. Thus, the orthogonal sine pattern projection is the optimal projection to measure the wound. In the following wound simulation and validation experiments we will only use the sine pattern projected orthogonally to the wound.

3.5.2 Wound width measurement

From the above section, we notice that SFDI exaggerates the wound shape in the AC images even with the orthogonal pattern offering more efficient sampling. From a conventional SFDI perspective, what SFDI can detect is usually more than the naked eye can. However, to better determine the heterogeneity with SFDI method, a question must be put forward first: how much can people trust the information from the "more than naked eye can see" from the results?

The AC image is the key input factor for the accuracy of the optical properties recovered to help answer our question. If the change in the wound structure cannot be at least illustrated from the intensity change of the AC curve, then the subsequent inverse process will not be able to see any change either. In this sec-

tion, we will focus on the AC result from the wound model to study the SFDI's sensitivity in observing the wound width and the dependence of parameters from both system and the wound model.

3.5.2.1 Error from wound width measurement

For instance, a typical SFDI simulation result is shown in the Fig.3.12 (a) where the AC image result is colour coded for intensity. In this model, the wound width is 2 mm with a spatial frequency of $f_x = 0.15$ mm^{-1}. The wound has a lower reduced scattering coefficient $\mu_s' = 0.71$ mm^{-1} than skin $\mu_s' = 1.42$ mm^{-1}. The wound area, with its lower scattering in this example and therefore lower returned intensity, can clearly be seen as the blue stripe in the centre. From the view in previous SFDI works, the complications are indicated by the difference in the optical properties. The width of wound is measured approximately using imageJ from the intensity difference as the marked on the Fig. 3.12 (a). The result is a width of 2.85 mm compared to the actual wound width 2 mm which significantly overestimate the wound structure by 42.5% demonstrating the partial volume effect.

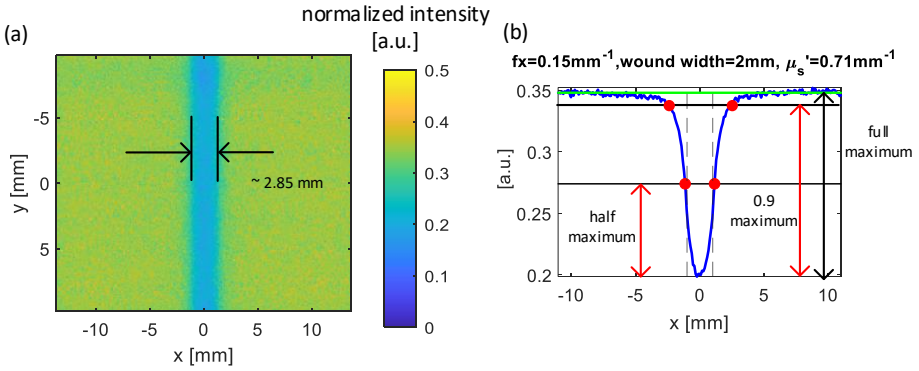

Figure 3.12: The I_{AC} image of 2 mm width wound model with wound $\mu_s' = 0.71$ mm^{-1}. (b) The $I_{curve,AC}$ of the wound model in (a). The green line marks the skin intensity level and two black lines mark the half maximum and 0.9 maximum of the wound intensity. The wound width is measured with the distance between two red points. The vertical dashed line is the real wound area according to the model parameters.

The answer to our question is that we cannot fully trust the SFDI's "more than

the naked eye can see" directly for the heterogeneity observation. Thus we need to look into the SFDI's accuracy in characterising the surgical wound structure change (wound width change). 3D Monte Carlo simulations are utilized for different wound widths, spatial frequencies and wound reduced scattering coefficients. The wound width are selected as 0.5 mm, 1 mm, 1.5 mm, 2 mm, 4 mm, and 6 mm. The interval between 0.5 mm and 2 mm is selected as 0.5 mm to test where the SFDI measurement breaks down as previous work[6] states the SFDI resolution is approximately 1 mm for most homogeneous sample. The four types of the possible wounds and one control type to mimic possible healing status with different reduced scattering μ_s' are listed in the Table. 3.1.

Table 3.1: The reduced scattering μ_s' of four types of wound and one control type.

Tissue Type	Reduced Scattering μ_s' / mm^{-1}
very low scattering wound	0.47
low scattering wound	0.71
no wound (healthy skin)	1.42
high scattering wound	2.84
very high scattering wound	4.73

The $I_{curve,AC}$ of the simulation results is calculated with Equ. 3.10. One of the typical $I_{curve,AC}$ resulting for the wound $\mu_s' = 0.71$ mm^{-1} with 2 mm wound width is presented in the Fig. 3.13 (b). The wound width is measured with the full width half maximum from each of the $I_{curve,AC}$ curves. The error of the measurement is obtained by $width_{measured} - width_{true}$ and plotted in the Fig. 3.13.

The results show a general trend that the error in estimating the wound width is decreased where the wound has a higher scattering coefficient as well as higher spatial frequency (this matches the experimental result from Bassi et al[143]). The relative error is significantly higher for the 0.5 mm and 1 mm wound especially in the low scattering wound model. This matches the previous conclusion that SFDI breaks down at around 1 mm resolution. Though the error when the wound width at 1 mm wound μ_s' is unexpectedly low due to the shape of the $I_{curve,AC}$. It can be seen that for the narrow wounds the error is significantly greater both in

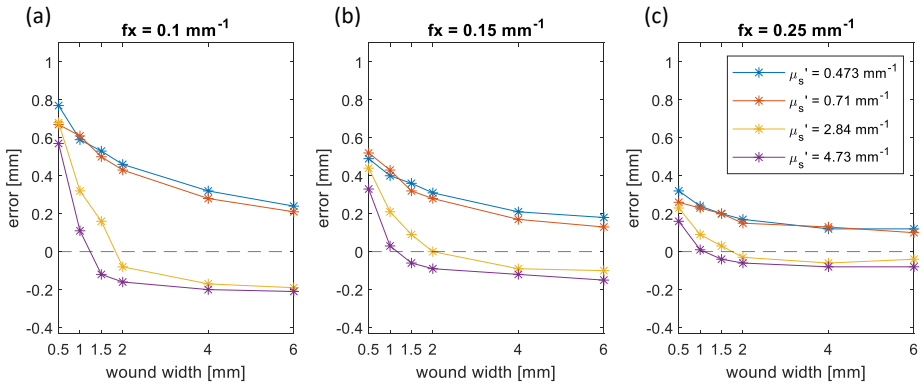

Figure 3.13: The error of the wound width measurement at the full width half maximum level in three spatial frequencies. The dashed line is y = 0.

distance and percentage of the actual wound width. This indicates that the photon interaction between the wound and healthy tissue is adding an effect to the wound structure measurement result. The key factor is the media's reduced scattering difference leading to the change in the ability of "keeping" photons in the same reduced scattering area. We will look further into this in the next section.

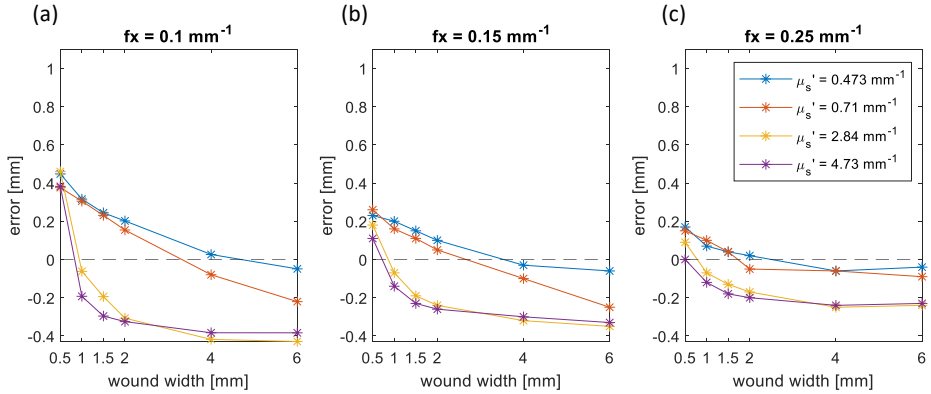

Figure 3.14: The error of the wound width measurement at the full width $\frac{1}{e}$ maximum level in three spatial frequencies. The dashed line is y = 0.

As the SFDI can exaggerate wound shape, then in clinical practice we should keep in mind to add on some compensations for this if possible. The two other ratios $\frac{1}{e}$ and $\frac{1}{\sqrt{e}}$ of the full width maximum are also utilized to estimate the wound width from the $I_{curve,AC}$. The absolute error of the wound width measurement for two

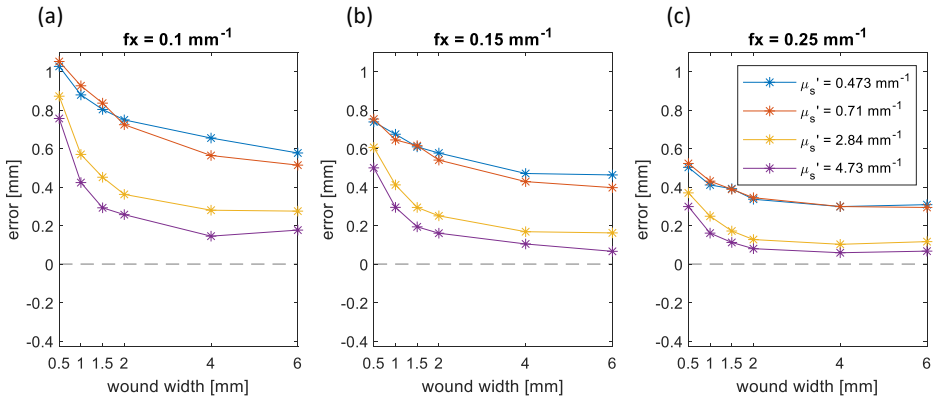

Figure 3.15: The error of the wound width measurement at the full width $\frac{1}{\sqrt{e}}$ maximum level in three spatial frequencies. The dashed line is y = 0.

ratios are shown in the Fig. 3.14 and Fig. 3.15. The ratio $\frac{1}{\sqrt{e}}$ always has largest error among three ratios in measuring the wound width. The $\frac{1}{e}$ provides less error at narrow wound width than full width half maximum. The larger ratio value for measurement results for the wound width are measured at the $I_{curve,AC}$ closer to the skin intensity level (see Fig. 3.12 (b)). Thus the error of the width will be higher as this can overestimate the wound width.

However, the low ratio is not always beneficial to the wound width result. The ratio $\frac{1}{e}$ shows in the Fig. 3.14 resulting in a large error in the original large wound width models. SFDI is already good at characterising the wider wound widths, so the low ratio cannot aid with this situation but in fact add extra uncertainty.

In the practice, one is suggested to select the ratio based on the estimated wound width and the reduced scattering coefficient of the wound area. We suggest to select the ratio 0.5 if the wound width is less than 2 mm, or even less than 0.5 for wound width less than 1 mm visibly. If the wound width is larger than 4 mm, we may suggest a ratio greater 0.5 as the μ_s' is able to present the real width. The larger wound width is, the more reliable the μ_s' map can reflect the wound structure.

3.5.3 Edge response

To examine the edge response (photon behaviour at the vertical interface between the healthy tissue and wound), four typical wound models with two wound widths 0.5 mm and 2 mm, are selected with wound reduced scattering $\mu_s' = 0.473$ mm^{-1} and $\mu_s' = 4.73$ mm^{-1}. The spatial frequency used for these four models is 0.1 mm^{-1}. We slice the $Weight_{down}$ through xz section at y = 0 (see Fig. 3.16 (e)) to view how the edge response contributes to the back scattered light intensity. In the $Weight_{down}$ plots we can only note photons once they have undergone one scattering event.

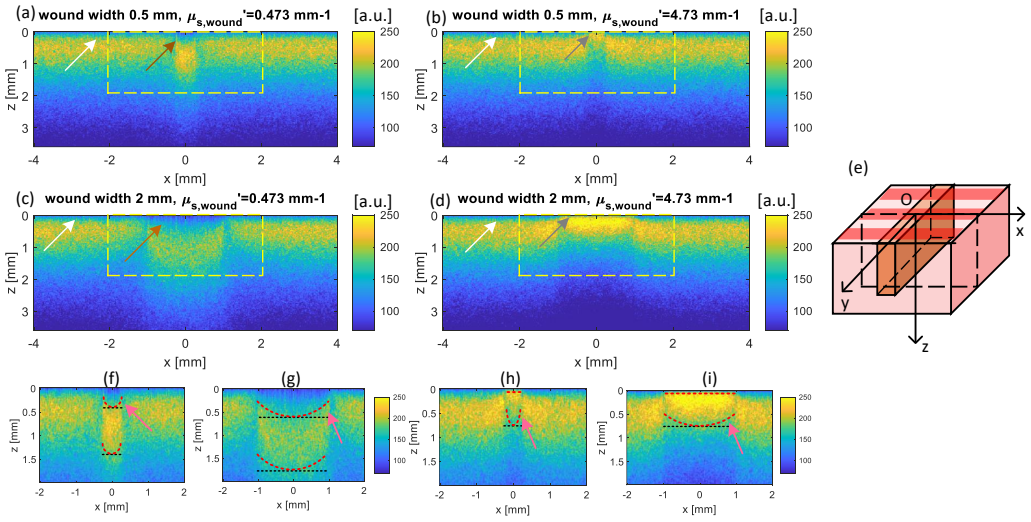

Figure 3.16: (a) - (d) The 3D edge response observed from the xz section of $Weight_{down}$ profile for the wound width 0.5 mm and 2 mm wound at $\mu_{s,\text{wound}}'$ = 0.473 mm^{-1} and $\mu_{s,\text{wound}}'$ = 4.73 mm^{-1}. (e) The slicing method through xz section at y = 0 mm. (g) - (i) is the selected area in plots (a) - (d) shown with the dashed yellow rectangle. The red dashed contour line locates where the intensity is 70% percent of the maximum intensity within the whole wound area. The ideal 70% intensity contour line assuming the wound is infinite homogeneous and with reduced scattering value is indicated with a black dashed line.

In the low scattering wounds, as shown in the Fig. 3.16 (a) and (c), the brown arrows point out the first scattering event occurrences at a significant depth into the tissue. In the skin, the first scattering event occurrence is closer to the top surface pointed out by white arrows. For the high scattering wounds, the first

scattering event occurs at a lower depth than in the low relatively lower scattering healthy skin, as illustrated by the grey arrows in the Fig. 3.16 (c) and (d). As expected, photons penetrate more deeply in the lower scattering tissue. However, there are clear contributions to the profile from the tissue adjacent to the wound which has different scattering values.

To look at this edge response more closely, we plot the the contour line of 70% maximum intensity in Fig. 3.16. If we assume there is an infinite homogeneous wound area, any intensity contour line should be flat. However, all of the contour lines here show a U-shape indicating the influence of the edge effect. For the low scattering wound model, the photons propagate down further in the 2 mm wound than the 0.5 mm wound as the two contour lines are both deeper. Though the absorption reduces the "weight" of the photons, the wider wound has significantly more photons at a greater depth. The photons between the real and ideal contour line as illustrated by the pink arrow in Fig. 3.16 (f) and (g), are the photons entering the wound from the skin. They have less chance of being scattered back to skin so generally travel within the wound resulting in the upper U-shape 70% contour line. There is decreased $weight_{down}$ intensity in the healthy tissue adjacent to the wound where the photons have been lost. The photons scattered into the wound hence have already travelled further when they enter the wound and lose their "weight" at a more shallow depth than the photons in the center forming the lower U-shape 70% contour curve.

Inversely, in the high scattering wound, the first scattering event is near the surface leading to a nearly flat 70% contour curve approximately at the surface for all the wound widths. Photons are scattering out of the wound leading to the higher intensity in the healthy tissue adjacent to the wound. Similarly, the photons entering the healthy tissue, with relatively lower reduced scattering, is less likely to be scattered back. Therefore the intensity is very low between the real and ideal 70% contour line as indicated by the pink arrow in Fig. 3.16 (h) and (i) where photons are lost from the wound to the healthy skin. The influence of the edge

effect is greater for narrower wounds. When comparing the narrow wound with the wide wound for the same scattering properties, the high scattering, narrow wound demonstrates lower intensity while the low scattering wound has higher intensity.

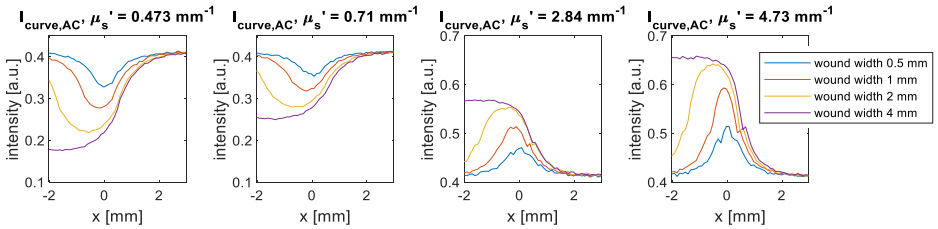

Figure 3.17: Four wound width 0.5, 1, 2, 4 mm $I_{curve,AC}$ are plotted particularly at the range where the curve approaching from the skin level to the centre of the wound area. The $I_{curve,AC}$ are aligned at full width 90% maximum by the 0.5 mm wound at right side.

To verify what we find from the $Weight_{down}$, we align the $I_{curve,AC}$ curves to the full width 90% maximum to compare the transition around the wound-skin boundary area. From Fig. 3.17, the 0.5 mm and 1 mm wound curve are separated from other curves due to the more significant edge response and photons staying in the lower scattering media. The 2 mm and 4 mm wound curves almost overlap at the transition area.

To include as much of the edge response in the $I_{curve,AC}$ as possible, in Fig. 3.18 we plot the calculated wound width using the full width at 90% percent of peak value. Here the high scattering wound always has a more accurate value as the difference in the mean free path between the healthy and wounded tissues is lower

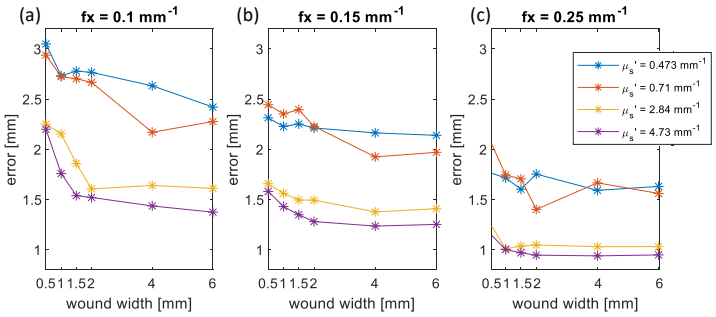

Figure 3.18: The error of the $I_{curve,AC}$ measured at full width 90% maximum.

leading to the reduction of the edge effect.

3.5.4 Can single phase rectangle pattern projection help?

We have demonstrated that three-phase sine wave projection is a feasible method in SFDI to determine the optical change in the wound structure. However, the three-phase imaging takes time hence increasing the chance of target area motion or side effect on the tissue. According to Nadeau et al[144], the single rectangular pattern can also be applied to obtain the back scattered image $I(x, y)$ for optical properties. The calculation complexity increases as the extraction of the AC information requires a 2-D Hilbert transform.

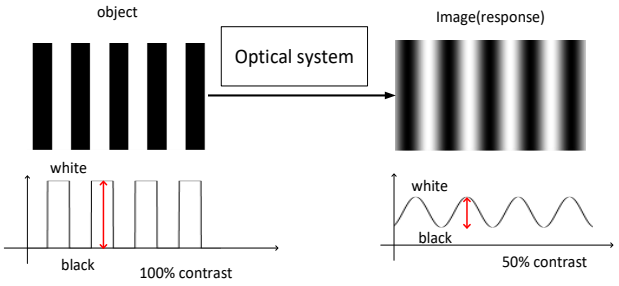

Figure 3.19: The example of the optical system response in our tissue to a periodic rectangle wave pattern.

For our wound monitoring purpose, the change in the wound μ_s' and wound structure are more crucial than obtaining the exact value. As we discussed in Chapter 2.2.2, the R_d is the MTF response of the tissue. The MTF could be obtained in two ways: one is calculating the contrast of the optical system response[145] (see Fig. 3.19 as an example) and the other is Fourier transforming the PSF of the optical system. If we regard the biological tissue as a black box, the contrast calculated from the diffuse reflectance via different spatial frequencies is the MTF of the biological tissue. In this section, we will test the single phase rectangle pattern to figure out if it is capable to detect the change in the optical properties and wound width.

3.5.4.1 MTF curve for different wound conditions

In this subsection, size of the wound model here is Nx = 1400, Ny = 500 and Nz = 800 pixels. The number of pixel in the y direction is reduced as there is no requirement for a number of periods in the x direction. As we have done in the previous sections, we keep the absorption $\mu_a = 0.023$ mm^{-1} and the anistropy $g = 0.9$ of the wound model constant as well. Three wound widths are selected at 1 mm, 2 mm and 4 mm. The spatial frequencies used are 0.1, 0.25, 0.5, 0.8, 1.5 and 2 mm^{-1}. The μ_s' for the wound are 0.473, 0.71, 2.84 and 4.73 mm^{-1} while the skin μ_s' is 1.42 mm^{-1}.

The orientation of the rectangle pattern is only parallel to the y direction (see the 4 mm wound width model example in the Fig. 3.20 (a)) magnifying the the edge response effect at the wound skin boundary. The orthogonal rectangle pattern can not provide sufficient contrast information from the wound and skin as shown in the Fig. 3.20 (b). The averaging result via x direction is the DC information of the wound model eliminating the effect of modulation. The averaging via the y direction mixes the wound and skin optical properties.

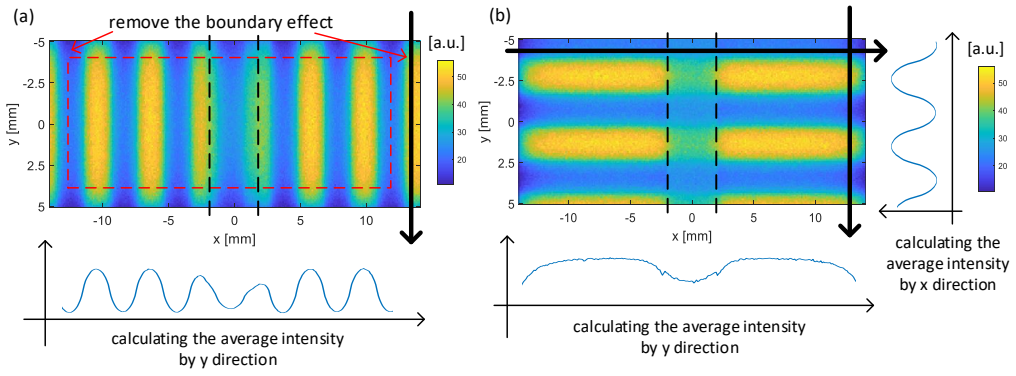

Figure 3.20: The wound width is 4 mm with $\mu_s' = 0.71$ mm^{-1} located at the centre of the wound, indicated by the black dashed lines. The spatial frequency of the pattern is $f_x = 0.25$ mm^{-1}. (a) A example of back scattered light image $I(x, y)$ of the parallel rectangle pattern. The 1D profile curve is calculated by averaging the intensity of the I by y direction. (b) A example of back scattered light image $I(x, y)$ from the rectangle pattern with the same wound model as in the (a). Two curves are averaged by both x and y direction.

Similarly, the back scattered light image $I(x, y)$ is averaged via the y direction to create a 1D profile $I_{curve,rect}$ of the wound model, reducing the noise as well.

$$I_{curve,rect} = \frac{1}{N_y} \sum_{y} I(x, y) \tag{3.11}$$

Then the contrast is calculated by the contrast of $I_{curve,rect}$ as

$$contrast = \frac{max(I_{curve,rect}) - min(I_{curve,rect})}{max(I_{curve,rect}) + min(I_{curve,rect})} \tag{3.12}$$

where the $I(x, y)$ is the back scattered light image from the top surface. The MTF curve is formed with the $I_{curve,rect}$ contrast at each f_x.

The MTF curves for the homogeneous tissue models with μ_s' at 0.473, 0.71, 1.42, 2.84 and 4.73 mm^{-1} are shown in the Fig. 3.21. With the f_x increasing, the MTF curve monotonically decreases, presenting the low pass filter feature of the biological tissue. The higher value in μ_s' leads to the greater contrast of the wound model matching the R_d trend in the Section 3.3 using the PSF to obtain the MTF.

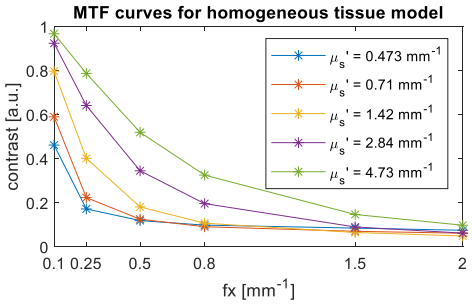

Figure 3.21: The MTF curves for homogeneous tissue model.

The MTF curves for the wound model, with healthy skin as the control group, are demonstrated in the Fig. 3.22. The curve cluster profiles via different wound μ_s can be classified into two group: low scattering wound (Fig. 3.22 (a), (b)) and high scattering wound (Fig. 3.22 (c), (d)). For the low scattering wound, the curve cluster converge at relative low spatial frequency and separate around $f_x = 0.25$ mm^{-1}. However the high scattering wound has the converse trend in

the MTF curve cluster. The MTF curves separates from $f_x = 0.1$ mm^{-1} to $f_x = 0.8$ mm^{-1} and then overlap at the following higher spatial frequency. Therefore the sampling effect from the sine pattern is not always better when the spatial frequency is increasing.

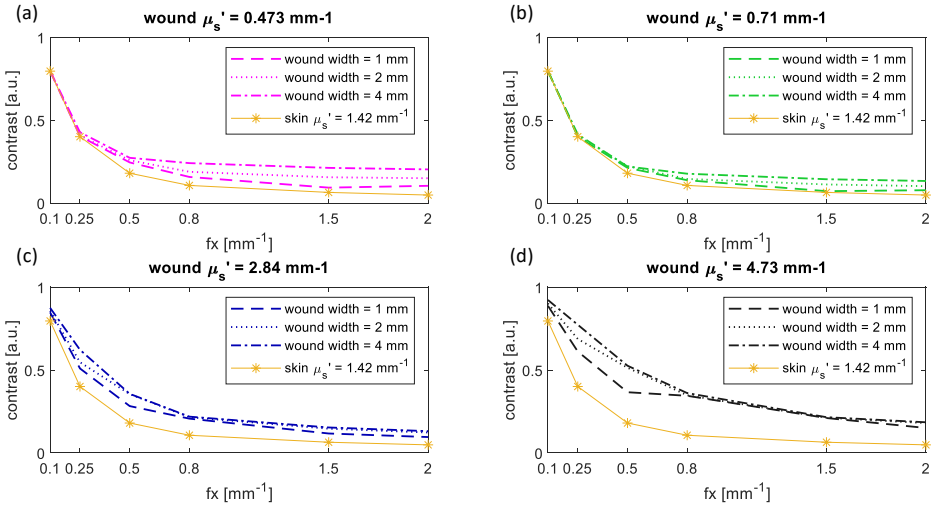

Figure 3.22: The MTF curves different wound width are plotted with same wound reduced scattering μ_s'. The MTF of skin as control group are shown in the yellow curves.

To look into the cluster performance, we plot the $I_{curve,rect}$ of the typical wound model with 1 mm, 2 mm and 4 mm wound width with two typical wound μ_s' 0.71 and 2.84 mm^{-1} applied in the simulation. We also mark the maximum and minimum data points for MTF calculation with hollow and solid circle marker separately on the $I_{curve,rect}$.

In the low scattering wound models (see the blue and red curves in Fig. 3.23 (a), (c) and (e)), all of the maximum values for different f_x are located in the skin area's peak on $I_{curve,rect}$. Due to the edge response, the minimum value there are from the skin area's valley. Therefore, in the Fig. 3.22 (a) and (b), the MTF value from $f_x = 0.1$ mm^{-1} to 0.25 mm^{-1} are presenting the homogeneous skin model which overlaps with the skin's MTF curve. When the spatial frequency increases (see yellow curves in the in Fig. 3.23 (a), (c) and (e)) the valley value in the wound

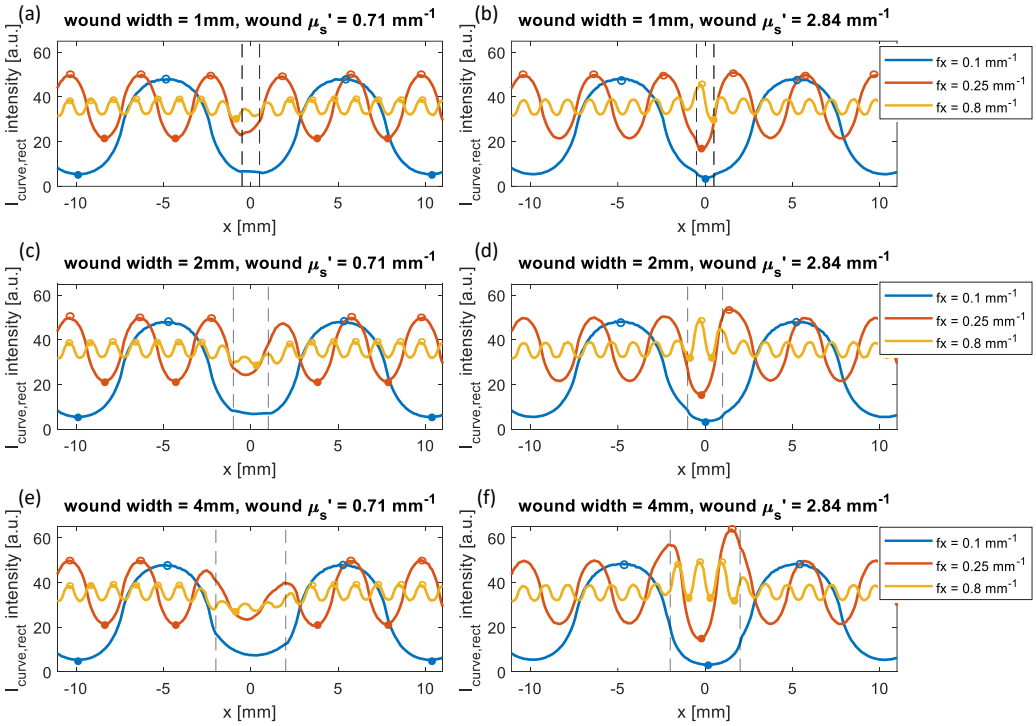

Figure 3.23: The $I_{curve,rect}$ of three wound widths are plotted with same wound reduced scattering μ_s'. The dashed vertical lines in each graph mark the wound area inside them. The hollow circle is the maximum data point in the curve and the solid circle is the minimum data point in the curve.

area becomes lower than the skin area's valley due to elimination of edge response. Thus, the minimum value of the $I_{curve,rect}$ is from the wound area's valley and varies with different wound width. Thus, the MTF curves in the Fig. 3.22 (a) and (b) are separated when f_x is higher than 0.25 mm^{-1}.

In the Fig. 3.23 (b), (d) and (f)), $I_{curve,rect}$'s minimum values are located in the valley of the wound area at f_x at 0.1 mm^{-1} and 0.25 mm^{-1} pairing with various different maximum values from the wound or skin's peak. Thus, the MTF curves in the Fig. 3.22 (c) and (d) are separated at relative low spatial frequency (< 0.8 mm^{-1}). However, with the f_x increasing, the minimum value locates in the skin area's valley while the maximum value always same from the wound area's valley as well. Again, the contrast results (MTF) are identical presenting a homogeneous wound model. Thus, at relatively high spatial frequency ($f_x = 0.8$ mm^{-1}),

the MTF curves overlap in the relatively high f_x range.

The high f_x is able to distinguish the difference in the low scattering wound as edge response buries the lower amplitude feature there but the high spatial frequency can overcome this. The low f_x is capable of demonstrating the difference in the high scattering wound when at least one of the maximum or minimum value is from the wound valley or at the wound-edge boundary. Therefore, we can confirm that the change in the wound model can be seen in the MTF curves.

For the simulation above, the valley of the rectangle pattern is sampling the wound area. More distinctive points might appear when the rectangle pattern's peak is covering the wound area especially for the narrow wounds. Thus, it's important to try shift the pattern to see if the pattern peak aids in detecting the change in the wound. We shift the rectangle pattern phase by π and $\frac{2\pi}{3}$ rad in the projection keeping the same spatial frequencies of pattern. The phase shift in π rad here flips the rectangle pattern to move the pattern peak into the wound. The MTF curve results from shifting two phases are shown in the Fig. 3.24 and 3.25.

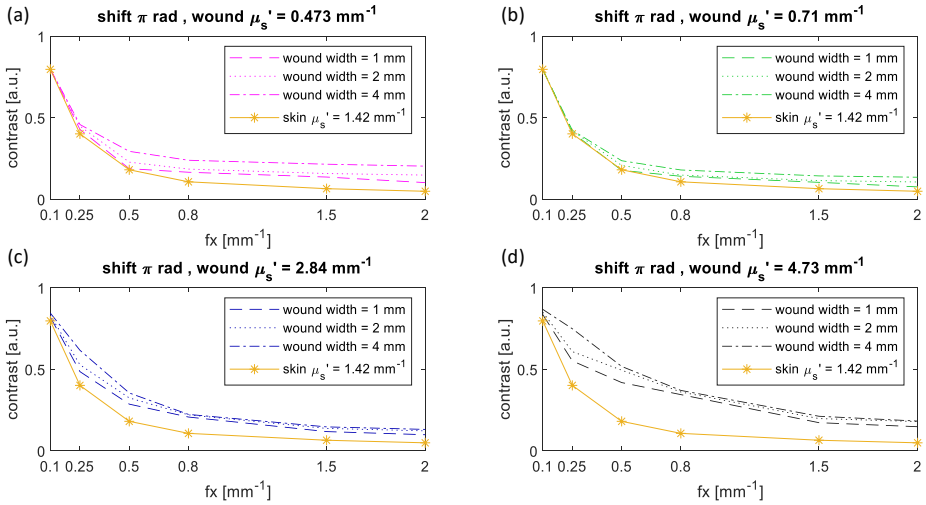

Figure 3.24: The MTF curve results from the rectangle pattern shifted with π rad compared to the Fig. 3.22.

The MTF result for the π and $\frac{2\pi}{3}$ are almost identical in the curve cluster profile. The trend of the curve cluster is similar but few separating points in low scattering

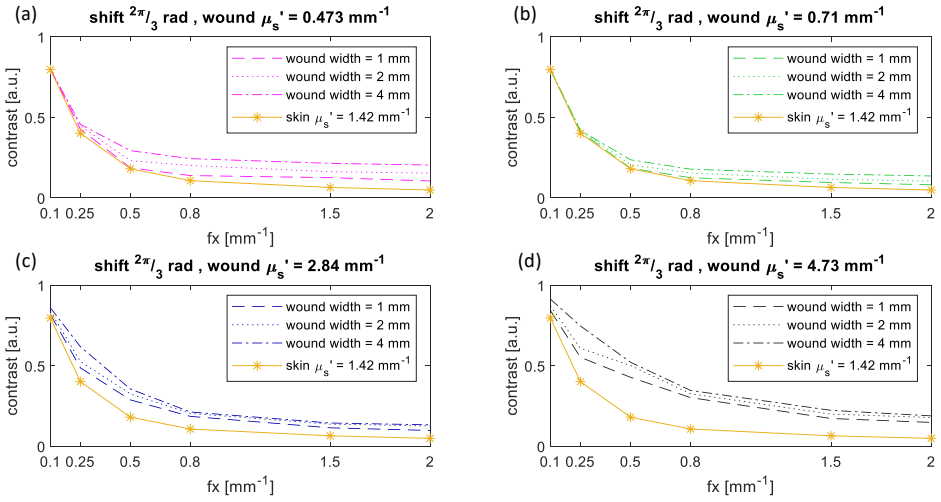

Figure 3.25: The MTF curve results from the rectangle pattern shifted with $\frac{2\pi}{3}$ rad compared to the Fig. 3.22.

wound MTF curves (see Fig. 3.25 (a) and (b)) are slightly different. The reason behind this is that the edge response has impact on projected pattern no matter there is a peak or valley lay on the wound area. In the next section, we will try distinguish the wound change via the shape of the MTF curve.

3.5.4.2 Curve-fitting method to distinguish the wound change

The shape difference clearly demonstrates the change in the wound model. However, we need to know exactly what a curve shape change corresponds to in term of a wound change for clinical application. To modelling the shape of the curve, the least-square fitting method is applied to obtain the regression coefficients of the fitting functions. The data points to use are the MTF curves for the different types of wound from the previous section as well as the homogeneous skin model's MTF curve. The candidate regression models for fitting include: $y = a\exp(bx) + \frac{c}{x}$, $y = \frac{a}{(x+b)}$, and $y = a\exp(\frac{b}{x})$. Here the variable x is the spatial frequency and the response value y is the contrast value from the MTF curves.

As shown in the Fig. 3.26 (d) and Fig. 3.28 (c), both functions $y = a\exp(bx) + \frac{c}{x}$ and $y = \frac{a}{(x+b)}$ are feasible to describe the MTF curve shape as the R^2 values are

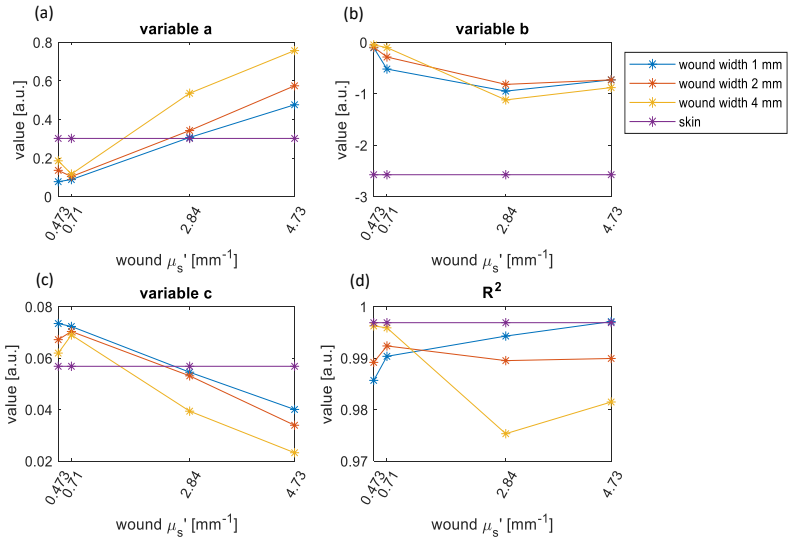

Figure 3.26: The fitting result using the function $f(x) = a\exp(bx) + \frac{c}{x}$. The R^2 is plotted in the (d) in the range 0.97 1.

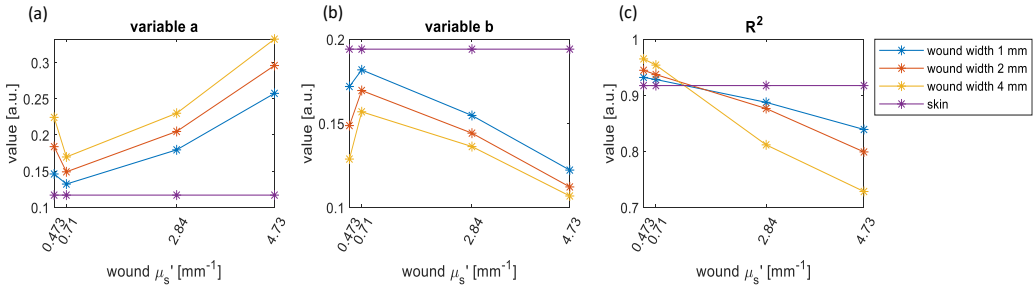

Figure 3.27: The fitting result using the function $f(x) = a\exp(\frac{b}{x})$. The R^2 is plotted in the (c) in the range 0.7 1.

very close to 1. However, in the Fig. 3.26 (a) and (b), the coefficient curves cross or overlap each other making it impossible to distinguish the change in wound width. At the same time, the straight purple curve shows the regression result for the homogeneous skin model (expanding at each μ_s' for comparison) going across the coefficient curves of wound model in the Fig. 3.26 (a) and (c) making the situation worse.

In the Fig. 3.27 (a), (b) and Fig. 3.28 (a), (b), the four curves are separated from each other with both the wound width and scattering change. Nevertheless, the trend of the curve is not monotonically with wound μ_s' meaning it is unlikely

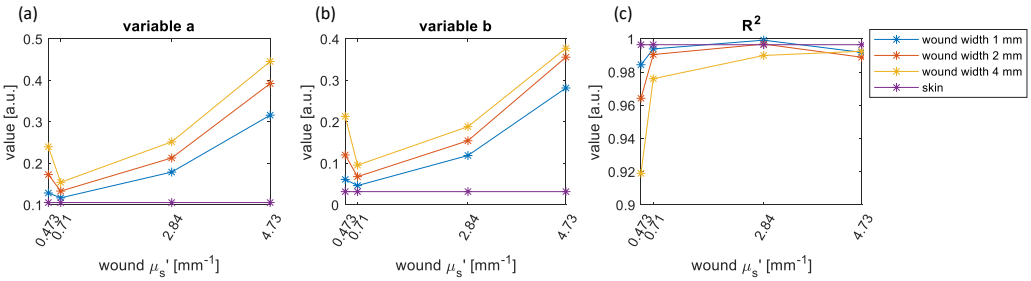

Figure 3.28: The fitting result using the function $f(x) = \frac{a}{(x+b)}$. The R^2 is plotted in the (c) in the range 0.9 to 1.

to determine the wound change with single set of regression coefficients from one wound model. Therefore, the curve-fitting method for the MTF curves is not able to distinguish the change either in wound structure or scattering properties.

3.5.4.3 Discussion

In the conventional three-phase sine pattern projection method to obtain μ_s' and μ_a using a look-up-table, at least six images are required. The rectangle pattern is simple in terms of the MTF calculation and has better accuracy when using a digital light projector. There are two degree of freedom in the change of the wound width and the reduced scattering coefficient. To determine the change in wound, at least three f_x rectangle pattern projections are required. In our simulation, the shape of the MTF curves does reflect the abnormal condition in the target skin area. Therefore, the rectangle pattern could be a swift test method which could be easily embedded with the SFDI instrument control software by comparing the MTF curves of target area with the reference healthy skin area. But for the further observation, the sine pattern is still required for the AC information extraction.

3.6 Conclusion

In this Chapter, we applied the Monte Carlo method to obtain numerical solution of the SFDI method. The sensitivity of SFDI method was discussed with the ho-

mogeneous model with various pairs of optical properties and spatial frequency f_x. SFDI was found to be more sensitive to μ_s' change in the low scattering media with a relatively low spatial frequency pattern. However, to look into the changes within the surgical wound, the sensitivity of detecting the structured changes underneath the wound is also important.

The conventional way of obtaining the diffuse reflectance from the point collimated beam is no longer feasible for the heterogeneous surgical wound model. Therefore we designed a 3D Monte Carlo simulation method to obtain the diffuse reflectance directly from a sine wave projection. The SFDI method was found to always exaggerating the structured changes in images due to the edge response. We also validated the estimated resolution of the SFDI method in the previous research paper. The SFDI's lateral resolution for wound width measurement via reduced scattering coefficient was explored for the first time with a simulated AC image. It is dependent on the spatial frequency, the wound width and the reduced scattering difference between the wound and skin. When these three parameters increase the accuracy of width measurement increases. The edge response was detailed with the $Weight_{down}$ profile with four typical wound model to discuss the reason behind the SFDI lateral resolution trend.

At the end of this Chapter, we explored a snapshot method using a single phase repeated rectangle pattern inspired by Nadeau et al[144] and the definition of MTF. The MTF curve results matches the result generated by the sine pattern. This only aids in a quick test but cannot provide one to one indication for the wound width and scattering change. In the next Chapter, we will conduct phantom imaging experiments to validate the simulation results.

Chapter 4

Instrumentation and phantom validation

In this chapter, we set up the SFDI system to validate the results from the Monte Carlo simulation with phantom imaging. The epoxy resin phantoms with different 'wound' widths and reduced scattering coefficients are designed to mimic the wound model.

4.1 SFDI system setup

4.1.1 Instrumentation

We built an SFDI imaging system based on the OpenSFDI set-up configuration[71, 146]. The geometry of the SFDI system is shown in Fig. 4.1 and the picture of the system is shown in the Fig. 4.2. The light from the 617 nm LED (Thorlabs, M617D2) is collimated and projected onto a digital mirror device (DMD) (Keynote Photonics, LC4500-NIR-EKT) encoded with a sinusoidal pattern. The achromatic lens focuses the pattern to the surface of the resin sample via the mirror. A pair of orthogonally aligned polarisers between the illumination and imaging optics ensures that only back scattered light is imaged by rejecting surface reflections from the sample. A USB camera (BFS-U3-13Y3M-C, Blackfly Camera, Edmund Scientific)

with a 35 mm focal length lens was used to capture the diffuse reflectance image. The field-of-view of the camera is 30 mm × 30 mm smaller than the projected sine pattern area 75 mm × 45 mm. The raw images are taken with a pixel effective size of 20 μm on the sample. The control software for the system is downloaded from the openSFDI website[147] and operated by Labview (version 2018 SP1).

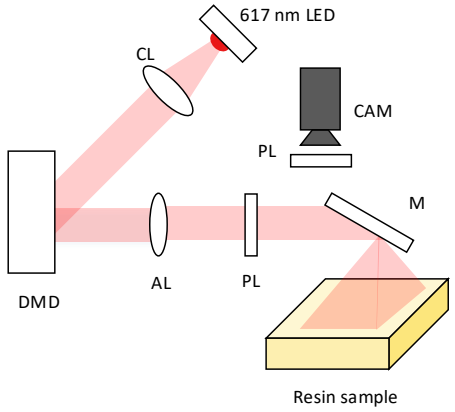

Figure 4.1: The geometry of the SFDI system for resin imaging experiment. CL = collimated lens with focal length 16 mm, AL = achromatic lens with focal length 50 mm, PL = polariser, M = reflective mirror, CAM = camera.

The panel of the control software is shown in the Fig. 4.3. It is an interface for applying the LED, DMD and camera automatically for SFDI three-phase imaging. For the hardware design, an Arduino Uno control board with the LED drivers (3021 buckpuck) switching on and off LEDs. The HDMI cable transfers the projection pattern to the DMD while the USB cable links the camera to take pictures at the set exposure time.

4.2 Resin phantom design

A tissue-simulating phantom is required to test our Monte Carlo simulation results and provide the calibration sample for the SFDI system. The biological simulating phantom is composed of matrix materials, scattering agents and absorption agents.

There are three types of the matrix base, including bulk matrix material, aqueous

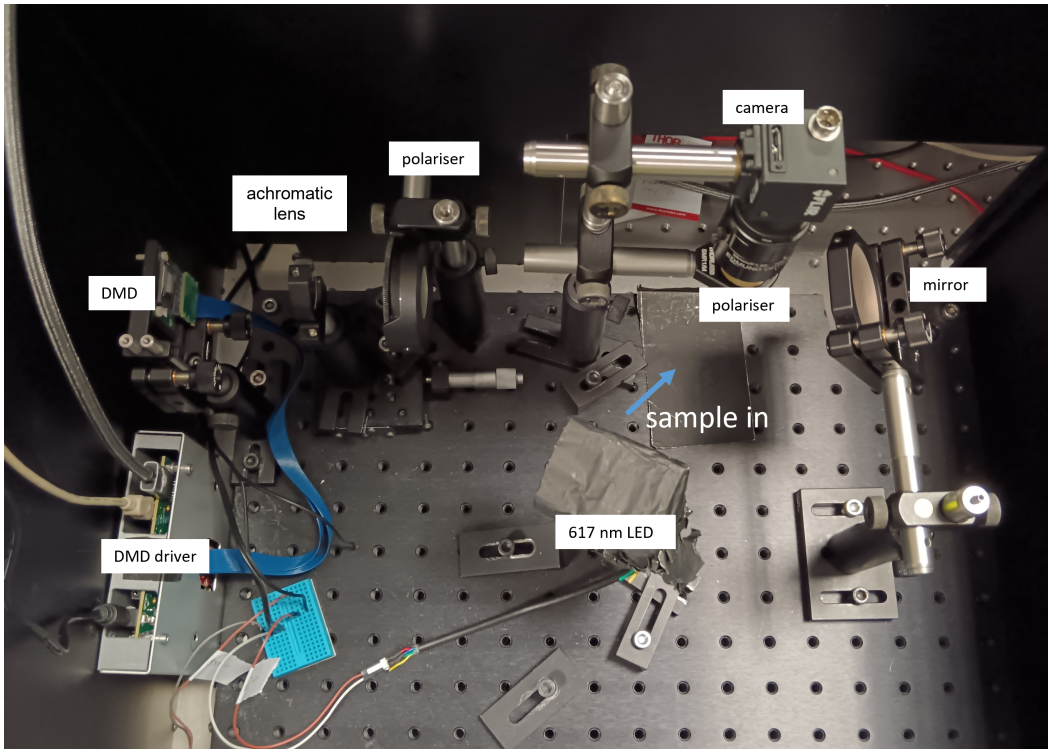

Figure 4.2: The picture of the SFDI system built up in the lab for resin imaging experiment.

suspension phantoms and hydrogel-based phantoms. The bulk matrix materials are always permanent and it is only possible to adjust the absorption and scattering coefficient (but only during casting). However, they are not biological and organic chemical compatible[148]. They are fabricated with polyester or epoxy resin[143, 149] and polyester such as polyvinyl chloride-plastisol[150] and PDMS[151, 94]. The aqueous suspension and hydrogel-based phantoms are compatible to a biological sample[148], e.g. the refractive index is close to biological tissue, but not long-lasting (less than few days). The aqueous suspensions are deionised water, PBS solution and lipid solution[152, 144, 153]. The hydrogel-based phantoms are commonly agarose[154, 155] and gelatin[99].

The commonly used scattering agents are titanium dioxide, TiO_2 powder, aluminum oxide, Al_2O_3 powder and polymer microspheres. The polymer microspheres[156, 98] can provide precise scattering values but are quite expensive to purchase. The TiO_2 and Al_2O_3 are cost-efficient materials. However, the final reduced

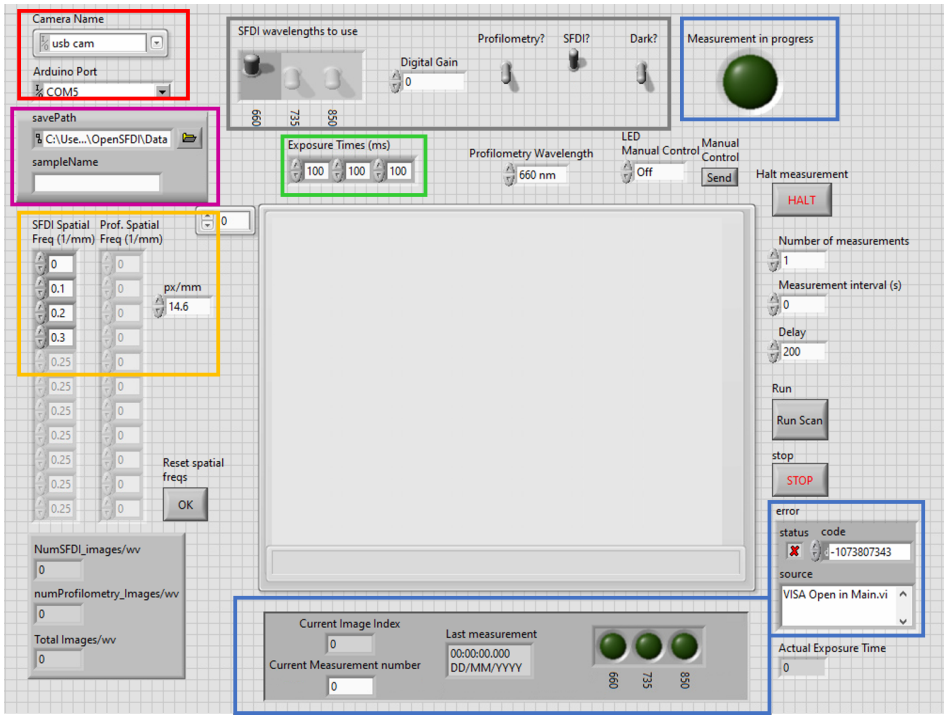

Figure 4.3: The data interface panel of the SFDI system for sine pattern projection and diffuse reflected image capture. Grey: LED control, Green: camera exposure time setting, Red: hardware connection, Purple: save file name and folder, Yellow: sine pattern spatial frequency, Blue: progress status.

scattering coefficient can vary from phantom to phantom even using the same concentration[148]. Clumps are very likely to appear and the suspension is not always adequate or uniform hence people need to measure the scattering properties prior to use. The absorption agents are used in the biological simulating phantom are Indian ink(carbon)[150, 151], whole porcine blood[99], instant coffee powder[157], nigrosine[85] and molecular absorbing dyes[144].

In our case, we wished to make the phantom sample stable in both shape and optical properties to ensure no change over extended time periods either during imaging or storage. Also we are more focused on the scattering changes so absorption is kept constant and low in the phantom. Thus, for the phantom materials we would prefer the material without absorption itself. We should also make sure no fluorescent effect will be introduced to the camera detector spectral range.

To validate the simulation results, we made resin phantoms with a similar structure

to the skin-wound imaging model, as shown in the Fig. 4.4. The healthy tissue part of the phantom was fabricated by epoxy casting resin and hardener (Glasscast50) in a ratio 2:1 by volume to create a transparent base with low visible absorption and scattering. Titanium dioxide (Sigma-Aldrich, 677469) was added to the mixture as a scattering agent, allowing the phantom scattering to be controlled based on the TiO_2 concentration.

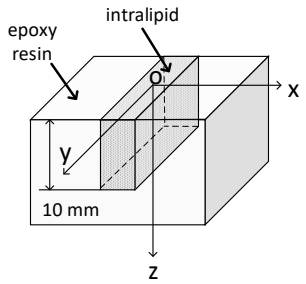

Figure 4.4: The structure of the resin sample containing the "wound" and "skin" part.

The wound width is selected as 2 mm, 4 mm and 8 mm in the resin sample to match the simulation results while 'wound' depth was fixed to 10 mm. Here, we choose wider wound widths for simulation validation as the imaging system is no longer ideal. The 'wound' block was filled with intralipid emulsion (Sigma-Aldrich, 20 emulsion) at various concentrations to create different scattering coefficients. The μ_s' of intralipid was calculated using the Rayleigh-Gans approximation[158] and listed in the Table 4.1. The absorption coefficient of the phantom was homogeneous in the phantom as TiO_2 does not absorb at our wavelength. The μ_a of the intralipid solution is 0.002 mm^{-1} at our wavelength.

Table 4.1: The reduced scattering coefficient μ_s' of the intralipid solution.

tissue type	reduced scattering μ_s' / mm^{-1}
0.5 $\%v/v$ intralipid	0.53
1 $\%v/v$ intralipid	1.01
2.8 $\%v/v$ intralipid	2.21
3.5 $\%v/v$ intralipid	2.84
4.5 $\%v/v$ intralipid	3.35
5 $\%v/v$ intralipid	3.56

The μ_s' and μ_a of the resin 'skin' and calibration resin sample were determined by using the method described in the previous work[15] measuring the optical properties of mouse skin in *vivo* as shown in the Fig. 4.5.

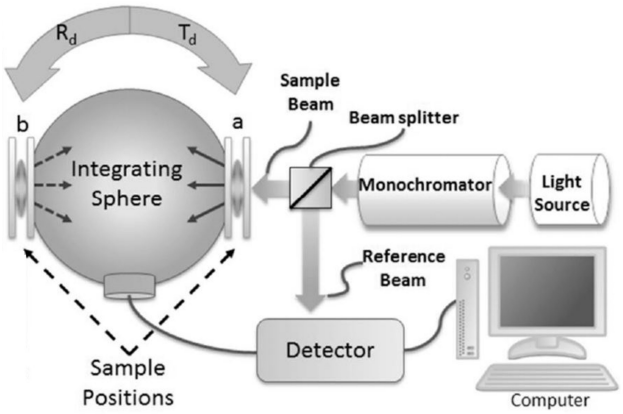

Figure 4.5: The geometry of the system measuring the reduced scattering coefficient and absorption coefficient in the resin sample. The system design is adapted from[15] which originally used to measure the mouse skin optical properties.

The transmission T and the reflectance R are measured by this instrument in our lab. By placing the resin in front of the light beam as in the position a while shut the port b, the transmission T is obtained. For the reflectance measurement, we shifted the sample to the position b. The collimated light source (at wavelength 617 nm) we used for this system is same as we had in the SFDI system.

Using the two-flux KM-model[159, 160], the reduced scattering coefficient μ_s' and absorption coefficient μ_a of resin sample can be calculated by KM coefficient:

$$A_{KM} = (x-1)S_{KM} \tag{4.1}$$

$$S_{KM} = \frac{1}{yD} ln\left[\frac{1-R(x-y)}{T}\right] \tag{4.2}$$

where D is the thickness of the resin sample, x and y can be yield with:

$$x = \frac{1 + R^2 - T^2}{2R} \tag{4.3}$$

$$y = \sqrt{x^2 - 1} \tag{4.4}$$

Using the KM coefficient A_{KM} and S_{KM}, the μ_a and μ_s' can be determined with

$$\mu_a = \frac{1}{2} A_{KM} \tag{4.5}$$

$$\mu_s' = \frac{4}{3} S_{KM} \tag{4.6}$$

With this method, the calculation result of resin 'skin' was $\mu_s' = 2.62$ mm^{-1} and $\mu_a = 0.004$ mm^{-1}. The picture of the resin sample we used in the lab is shown in the Fig. 4.6.

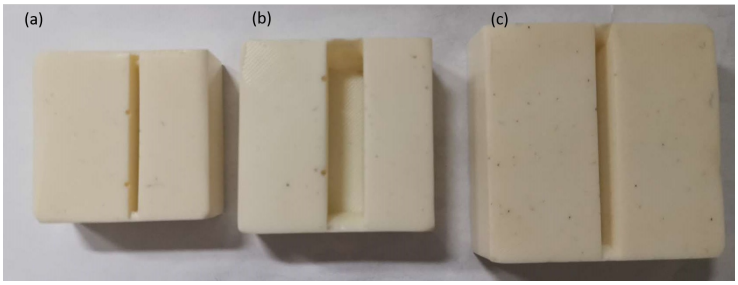

Figure 4.6: The resin samples with (a): 2 mm, (b): 8 mm and (c): 4 mm "wound" width. The outer shapes of the three resin phantom are different because they were made at the same time with different size of moulds. The outer size of the resin blocks are: (a) 35 mm × 35 mm, (b) 40 mm × 40 mm, (c) 45 mm × 45 mm. The width and length of them are guaranteed wider than the imaging system's field of view.

4.3 Phantom optical properties measurement

The spatial frequencies used in the experiment are 0.1 mm^{-1}, 0.2 mm^{-1} and 0.3 mm^{-1}. The SFDI system is calibrated with a homogeneous resin sample of

$\mu_s' = 1.2$ mm^{-1} and $\mu_a = 0.004$ mm^{-1}. The calibration resin sample is also imaged under the same condition to optimise the illumination and remove the systematic noise. The raw images are binned in 5×5 window before processing to improve the signal to noise ratio (SNR) and speed up the image processing without any loss of useful resolution. The appSFDI[71] software is utilized to recover the μ_s' map.

4.4 Orientation of the sine pattern projection

Firstly the experiments are conducted with the same sine pattern orientated parallel, orthogonal and 45 degree orientation sine pattern to the 'wound' in the resin phantom. The spatial frequency used is 0.1 mm^{-1}. The wound areas are filled with two typical 0.5% and 5% concentration of intralipid solution to create the low and high scattering wound model separately. The reduced scattering coefficient μ_s' of the 'wound' here is 0.53 mm^{-1} and 3.56 mm^{-1}. The parallel, orthogonal and 45 degree sine pattern are projected respectively to the resin phantom at a spatial frequency 0.1 mm^{-1}. The wound width of the resin phantom are 2 mm, 4 mm and 8 mm.

The light correction for the resin sample AC image is calculated with

$$I_{AC,correction} = \frac{I_{AC,sample}}{I_{AC,calibration}} \tag{4.7}$$

where the $I_{AC,calibration}$ is the AC image of the calibration resin sample, $I_{AC,sample}$ is the original resin sample's AC image calculated from three-phases diffuse reflectance images. The $I_{curve,AC}$ is then denoised with moving average method and median filter.

The $I_{curve,AC}$ for two types of scattering resin sample are calculated from Equ. 3.10 using the $I_{AC,correction}$ and shown in the Fig. 4.7 and Fig. 4.8. For the same resin phantom, the $I_{curve,AC}$ are aligned with the centre of the wound area. Though the noise removal method effectively remove the noise from the $I_{curve,AC}$, it is still

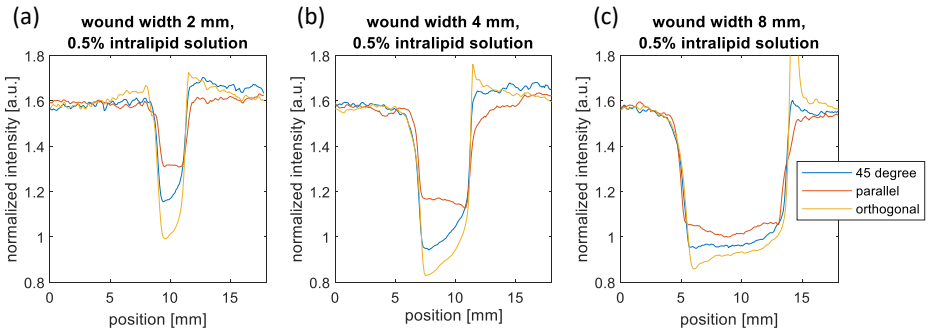

Figure 4.7: The $I_{curve,AC}$ from the resin sample results with low scattering intralipid filling wound.

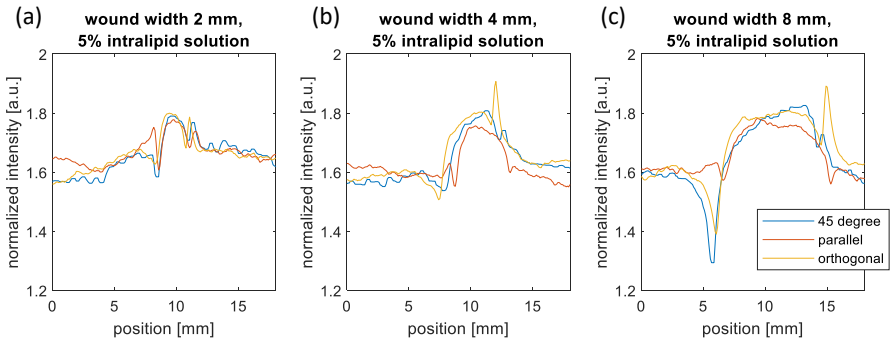

Figure 4.8: The $I_{curve,AC}$ from the resin sample results with high scattering intralipid filling wound.

more noisy than in the simulation. The noise comes from the resin sample's TiO_2 inhomogeneous small lump of scatter, physical 'wound' sharp edges in the resin, the reflectance due to the surface tension in the intralipid solution and the not perfectly even resin surface.

In the low scattering wound models (see Fig. 4.7), the orthogonal projection pattern has the lowest intensity in the wound area while the parallel pattern has the highest intensity. This matches the simulation result in the Section 3.5.1. The 45 degree sine pattern has the moderate intensity in the wound area as expected, partly due to the edge response from the parallel sine pattern projection. When the wound width increases, the intensity of the wound area decreases due to the elimination of the edge response. This agrees well with the simulation result for the relationship between the wound width and the edge response impact.

Similarly, in the high scattering wound model (see Fig. 4.8), the high to low signal intensity order of the wound area is orthogonal pattern, 45 degree and finally parallel pattern. The intensity difference between the three projection models is not obvious comparing to the low scattering wound model. This phenomenon is the same as we learn from the Monte Carlo simulation, SFDI is less sensitive with high scattering coefficient.

In both of the wound models, the orthogonal sine pattern projection is most sensitive to the change in the wound reduced scattering coefficient. Thus, it is most suitable for characterising the wound width. In the following section we will only use the orthogonal pattern for the simulation result validation. And we recommend the surgical wound site imaging with SFDI to project the sine pattern orthogonal to the wound cut.

4.5 Resin wound measurement result

Using the orthogonal sine pattern for the phantom imaging, the AC images are obtained from $f_x = 0.1$, 0.2 and 0.3 mm^{-1}. The wound width is measured from 1D profile of the AC images calculated by Equ. 3.10. Similarly to creating a 1D profile for the wound via $I_{curve,AC}$, we calculate $I_{curve,LUT}$ from

$$I_{curve,LUT} = \frac{1}{N_y} \sum_y \mu_s'(x, y) \tag{4.8}$$

where the $I_{curve,LUT}$ is the recovered μ_s' map image and direction for the averaging is same as for simulated $I_{curve,AC}$.

Hence we measure the wound width at full width half maximum to validate the wound measurement. The error of both measurement is calculated with $error = results - truth$. The error from the AC results and LUT results are compared in the Fig. 4.9. The error plots clearly illustrate the reduced scattering and spatial frequency's influence of the edge effect as the wound width increases. With the

spatial frequency increasing, the wound width measurement error reduces in both AC images and μ_s' maps. The half maximum underestimates the wound width for the wider wound (8 mm) where the edge response reduces. But it is overall a good compromise across the range of wound width.

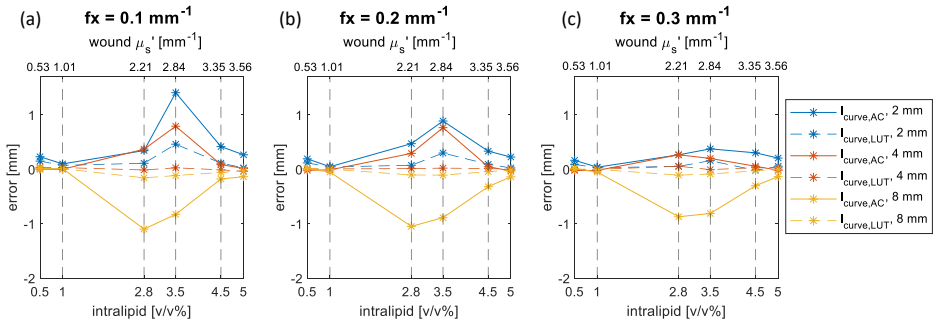

Figure 4.9: The relative error of the resin phantom measurement from full width half maximum level at three spatial frequencies f_x = 0.1, 0.2 and 0.3 mm^{-1} (a) f_x = 0.1 mm^{-1}, (b) f_x = 0.2 mm^{-1}, (c) f_x = 0.3 mm^{-1}. The solid lines are the results from the AC image while the dashed lines from the reduced scattering map.

Looking at the solid lines demonstrating the error from the $I_{curve,AC}$ firstly, there is a vaguely inverted U-shape or U-shaped (due to the negative value) in the line shapes. The peak is around intralipid concentration 3.5% with the greatest uncertainty. This concentration provides value of μ_s' of 2.84 mm^{-1}, very close to skin μ_s' at 2.62 mm^{-1} leading to $I_{curve,AC}$ with a flatter shape. Thus, the error in the width measurement is significantly increased. However, there is no detriment to monitoring the wound with SFDI as the healed wound's μ_s' approaches that of the surrounding tissue. From another perspective, when complication arise in the wound μ_s', deviating from the healthy skin μ_s', it can be measured with less error.

Comparing the dashed lines (from $I_{curve,LUT}$) to the solid lines, the error is much lower in the LUT result. The calibration and LUT method effectively removes the modulation transfer function (MTF) of illumination and imaging system. Also, the full width half maximum method to determine the wound width here may works better for LUT result than $I_{curve,AC}$. The relative error of both measurement is shown in the Fig. 4.10. Though the error seems huge in the Fig. 4.9, the

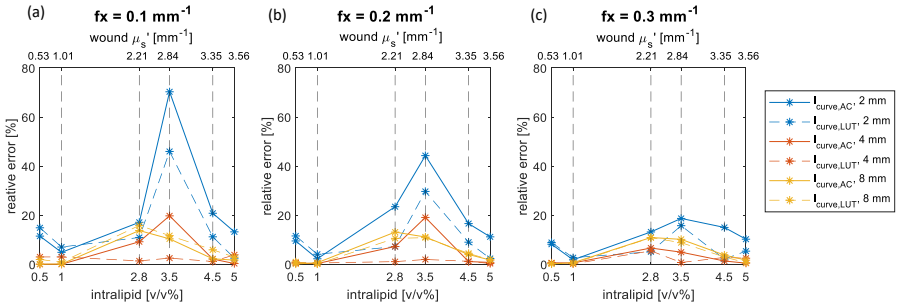

Figure 4.10: The relative error of the resin phantom measurement from full width half maximum level. (a) $f_x = 0.1$ mm^{-1}, (b) $f_x = 0.2$ mm^{-1}, (c) $f_x = 0.3$ mm^{-1}. The solid lines are the results from the AC image while the dashed lines from the reduced scattering map.

wider wound width still has low relative error which benefit wider wound width measurement.

In the Chapter 3, we also use greater and smaller ratios to the full width maximum to measure the wound width from the $I_{curve,AC}$. Here we also take the full width $\frac{1}{e}$ maximum and full width $\frac{1}{\sqrt{e}}$ for measurement as well. The error is shown in the Fig. 4.11 and Fig. 4.12.

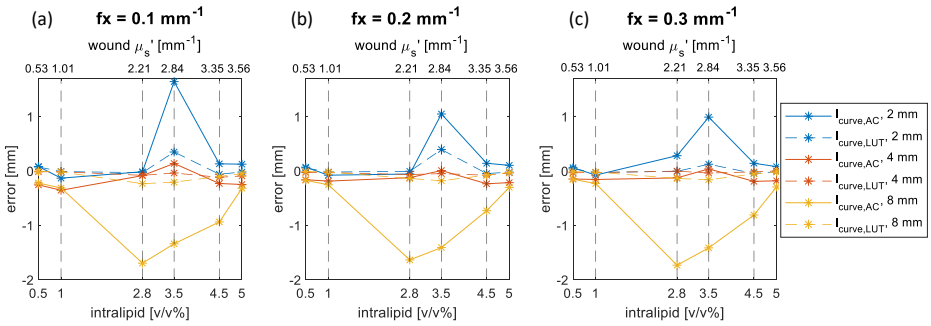

Figure 4.11: The error of the resin phantom measurement from full width $\frac{1}{e}$ maximum level. (a) $f_x = 0.1$ mm^{-1}, (b) $f_x = 0.2$ mm^{-1}, (c) $f_x = 0.3$ mm^{-1}. The solid lines are the results from the AC image while the dashed lines from the reduced scattering map.

Looking at the solid lines first, the ratio $\frac{1}{e}$ of the maximum measurements helps correcting the spill out of wound signal in $I_{curve,AC}$ especially for a narrow wound. The ratio $\frac{1}{\sqrt{e}}$ has the best accuracy for the wide wound (8 mm) measurement as this level of maximum is closest to the skin level. The 4 mm wound model can

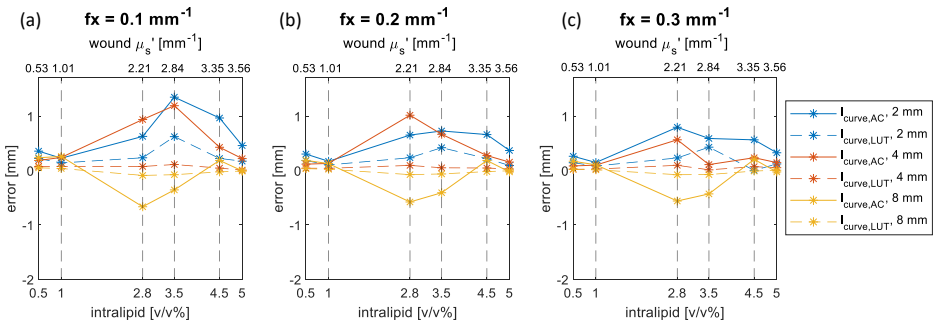

Figure 4.12: The relative error of the resin phantom measurement from full width $\frac{1}{\sqrt{e}}$ maximum level. (a) $f_x = 0.1$ mm^{-1}, (b) $f_x = 0.2$ mm^{-1}, (c) $f_x = 0.3$ mm^{-1}. The solid lines are the results from the AC image while the dashed lines from the reduced scattering map.

have better accuracy than 8 mm wound matching the conclusion in the simulation. This, once again, indicates the importance of selecting the appropriate width measurement to correct the edge response.

Comparing the three ratios of maximum, the measurement error resulting from the μ_s' map are lower than in the AC images. However, the results from $I_{curve,LUT}$ map do not always follow the $I_{curve,AC}$'s trend in error. The reason behind this is that the LUT grid is not linear[6] and the accuracy of interpolation depends on the scattering values and the processed AC image intensity.

Different pairs of the spatial frequency also generate look up tables with different grid shape and interval[96] as shown in the Fig. 4.13. The LUT grid becomes finer where the LUT's resolution decreases with the μ_s' and μ_a increase. The reason behind this is the SFDI's sensitivity reduces in distinguishing the higher μ_s' in AC image intensity. Also, when the absorption from the tissue is very high, fewer photons will back to the surface leading to low SNR signal carrying the tissue information. The looking up method locates four of the adjacent neighbour points for the input R_d. The interpolation is then conducted to recover the μ_s' and μ_a with the pair of value. The larger distance between the four neighbouring points, a more accuracy in optical property recovery can be achieved. Therefore, the measurement error from $I_{curve,LUT}$ map is probably becoming greater when the spatial frequency

is not appropriate for the tissue's optical properties.

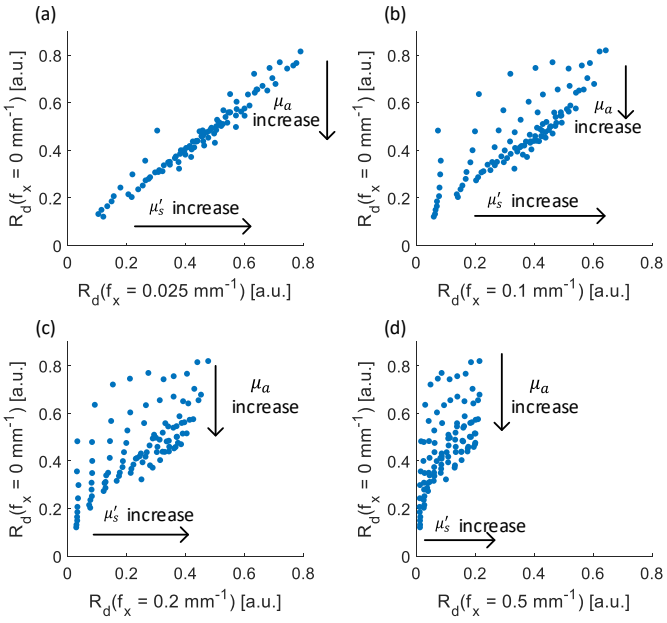

Figure 4.13: The LUT for the different f_x pairs in the same mu_s' range from 0.473 mm^{-1} to 4.73 mm^{-1} and μ_a range from 0.005 mm^{-1} to 0.12 mm^{-1}.

4.6 Discussion and conclusion

In this Chapter, we built up the instrument for the SFDI system in the laboratory for the phantom imaging and the further biological imaging experiments. We reviewed the material and fabrication methods for the biological mimicking phantom. The epoxy resin and the intralipid solution are utilized for the calibration and testing sample in the validation experiment.

Two series of validation experiments are conducted: a) The projection orientation for sine pattern b) wound width measurement with AC image and μ_s' maps. The noise level is clearly higher in the real situation. The orthogonal sine pattern is still the best for the wound characterisation and following wound width measurement are imaged with the orthogonal pattern. The impact of edge response is observed from the simulation appear in the practice again. The ratio of the wound width

measurement maximum level is also related to the accuracy of the results. This is in excellent agreement with the Monte Carlo simulation. In the next Chapter, we will use this system to monitor in vivo human skin for the wound and skin complications.

Chapter 5

In vivo human tissue measurement

In this Chapter we present the results from the human skin imaging experiments. Following the modelling and resin phantom experiment, we are interested in how precisely can SFDI detect the changes in the wound/skin structure, blood content and oxygen level within the wound healing process.

We conducted three *in vivo* experiments in this Chapter including a eczema site monitoring, sodium lauryl sulfate (SLS) skin irritation experiment, and biopsy wound monitoring. They are three typical skin and wound conditions of interest to the clinicians. The eczema site presents chronic skin barrier (stratum corneum) damage to the epidermis, or even to the dermis, which are also a common feature in wound healing. The SLS testing on skin creates an acute skin irritation include inflammation and possible temporary damage to the epidermis. We aimed to see how sensitive is SFDI to this condition by measuring the reduced scattering coefficient μ_s', absorption coefficient μ_a and oxygen saturation StO_2. Both eczema monitoring and SLS testing serve as a preliminary study for the possible wound healing condition. Finally, the biopsy is a typical surgical wound observed, for the first time using SFDI in wound imaging.

All *in vivo* human tissue imaging protocols in this thesis were approved by the

Ethics Committee of Durham University.

5.1 Methodology

5.1.1 Instrumentation

Similarly to the instrument built in the Chapter 4, the optical path design to measure the volunteer's hand is shown in the Fig. 5.1 and the instrument picture is demonstrated in the Fig. 5.2. Here we add one more LED at 850 nm following the guidance of the openSFDI website[146]. The 617 nm LED is kept as this wavelength is sensitive to the hemoglobin[24]. The 850 nm LED is applied providing deeper penetration within the skin at the same time avoiding the water absorption window in the infrared spectral region. The dichroic mirror is placed between two LEDs to reflect the 850 nm light beam to the DMD at the same time passing the 617 nm light beam through the original direction. The spatial frequency was selected as 0.1 mm^{-1} for a deeper penetration measurement.

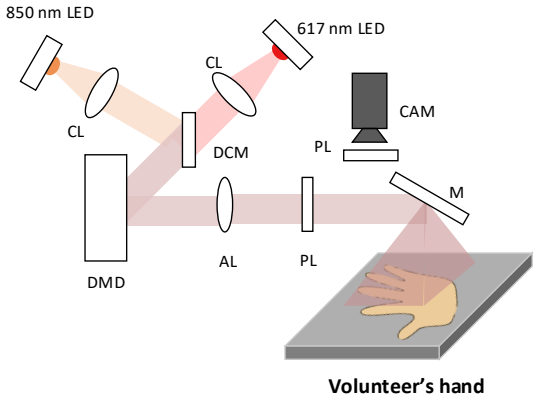

Figure 5.1: The geometry using dual wavelength LEDs to image the biopsy wound on volunteer's hand. The geometry of the SFDI system for resin imaging experiment. CL = collimated lens focal length 16 mm, DCM = dichroic mirrors, AL = achromatic lens focal length 50 mm, PL = polariser, M = reflective mirror, CAM = camera.

As described in Chapter 4, the calibration sample is made with epoxy resin and TiO_2. At 617 nm, the reduced scattering coefficient μ_s' of the resin sample is

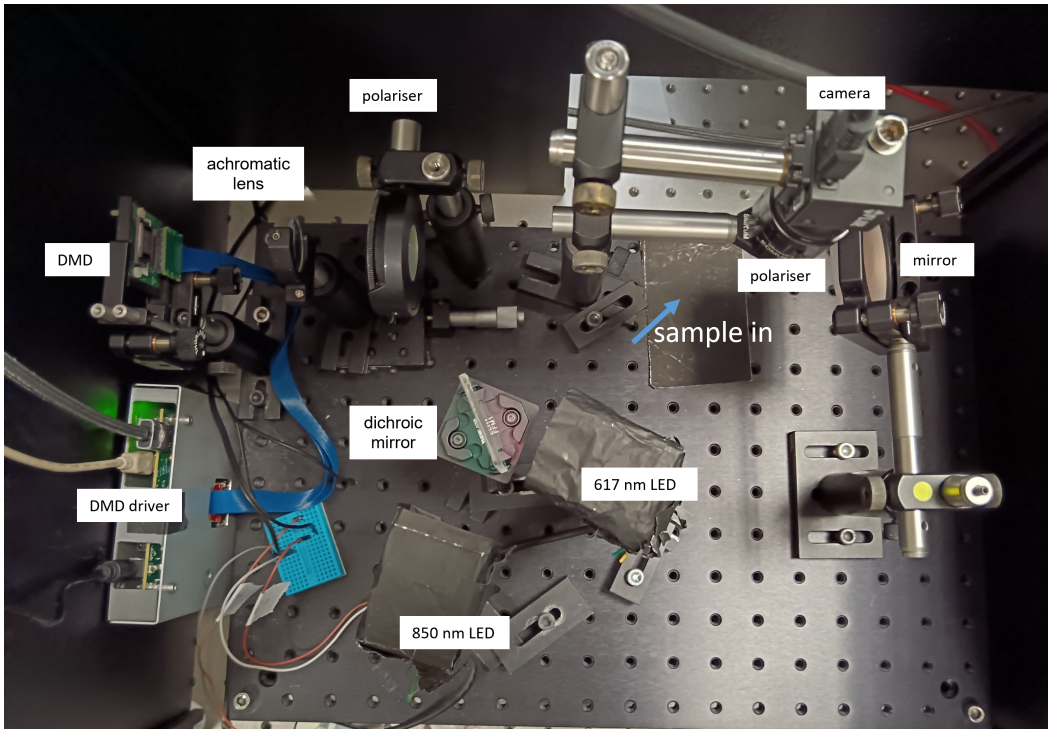

Figure 5.2: The SFDI system built up for skin imaging experiments.

1.2 mm^{-1} and absorption μ_a of the resin sample is 0.004 mm^{-1}. At 850 nm, the resin sample has $\mu_s' = 0.8$ mm^{-1} and $\mu_a = 0.004$ mm^{-1} under the 850 nm wavelength. The calibration sample is imaged under the same conditions as used in the skin imaging.

5.1.2 Hemodynamic monitoring

The relative oxygen saturation (StO_2) of the target area is calculated based on the absorption of the extracted μ_a at two wavelengths.

$$\mu_a(\lambda) = ln(10)[\varepsilon_{HbO_2}(\lambda)c_{HbO_2} + \varepsilon_{Hb}(\lambda)c_{Hb}] + \mu_{a,water}(\lambda) \times 0.7 \qquad (5.1)$$

The HbO_2 is the oxy-hemoglobin and the Hb is the deoxy-hemoglobin. The molar extinction coefficients are $\varepsilon_{HbO_2}(\lambda)$ and $\varepsilon_{Hb}(\lambda)$ correspondingly. c_{HbO_2} is the molar concentration of HbO_2 and c_{Hb} is the c_{Hb} of Hb. The $\mu_{a,water}$ is the absorption of the water at the wavelength λ and we assume the water content of human skin

is 70% to have better accuracy in the hemoglobin results. The oxygen saturation StO_2 is calculated with

$$StO_2 = c_{HbO_2}/(c_{HbO_2} + c_{Hb}) \tag{5.2}$$

Here the molar extinction coefficients for the two wavelengths are listed in the Table. 5.1 from the omlc website[161].

Table 5.1: The molar extinction coefficients for HbO_2 and Hb.

Wavelength	ε_{HbO_2} / $moles \cdot cm^{-1}L^{-1}$	ε_{Hb} / $moles \cdot cm^{-1}L^{-1}$
617 nm	1068	6927.2
850 nm	1058	7136

5.2 Eczema observation

Eczema is a chronic, inflammatory and relapsing skin conditions present in 5 - 10% of the adult population[162]. The common symptoms include skin dryness, red and scaly skin, chapped patches, itchy feeling and even fluid weeping. The incidence of eczema is increased by immune system reaction, filaggrin mutations, environment temperature change, contact with irritant chemicals and allergic reaction with food[163]. The symptoms of eczema vary from erythema, edema papulation, excoriation and lichenification[164], listing in a minor to severe order.

There are a few reported works using optical methods for characterising the condition mainly using Raman spectroscopy[165, 166] to analyse the compound and bio-markers of the eczema area and a healthy skin control group. The water, lipid and collagen content revealed cause a decrease in the Raman spectrum signal and keratin leads to a increased in the signal. Multispectral imaging[167] compared the spectral difference in the eczema area and a healthy skin from 365 nm to 970 nm showing eczema area has a higher reflectance. Optical coherence tomography (OCT) was also utilised to look at the vessel and structural change in the eczema[168, 169].

The thickness of the epidermis was found to increase by approximately 100% and the blood vessel density was found to increase in the eczema area where plexus was observed to be pushed deeper into the skin when the eczema worse. Optoacoustic mesoscopy[170] was also applied to measure epidermis changes and the oxygen level of the lesion area in the eczema. The epidermis thickness measurement there matches the OCT works and hemoglobin and oxygen saturation level both increased.

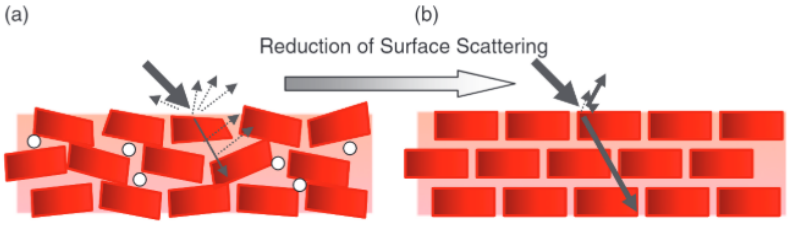

Figure 5.3: When the skin get hydrated, the surface scattering decreases with the 'brick and mortar' model in (a) changing into a well organised structure in (b). The picture adapted from [16].

A dryness patch is a common sign in eczema. The skin scattering coefficient is reported to increase with the dehydration as shown in the Fig. 5.3. SFDI has not yet looked into the eczema condition. Based on the other works reviewed above, the dryness and dehydration in the skin probably demonstrates higher reduced scattering coefficients. The excoriation in the skin may result in a locally lower reduced scattering in value as the epidermis has relatively higher reduced scattering than the dermis[24]. The redness of the patch, indicating a inflammatory response, may introduce more blood cells to the dermis.

In this section, we report applying SFDI to monitor an eczema skin site. It provides a good chance for us to monitor the inflammatory response and the epidermis damage and thickness change in the human skin.

5.2.1 The eczema site information

We recruited a male volunteer with Fitzpatrick skin type 3, aged 26. There are two eczema sites reported on his right hand as shown in the Fig. 5.4 present for 2 months due to contacting an unknown source of allergy and exposure to the dry and cold weather condition in February 2023. The symptom is self-rated as moderate so our volunteer did not choose to have a clinical assessment. During the observation, he started occasional treatment with 'Aesop rind concentrate body balm', a commercial moisture cream, as his hand cream, without prescription. There was no moisture cream applied to the eczema area before our imaging experiments according to the volunteer.

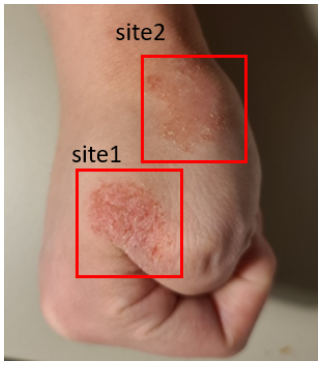

Figure 5.4: The visible (VIS) picture of volunteer's right hand taken at day 0 of observation. The site 1 and site 2 eczema are shown in the red rectangle.

We selected site 1 for observation as it is much flatter in shape than site 2, where curvature will greatly decrease the signal-noise-ratio (SNR) of the optical property maps. As the eczema is a chronic skin condition and our volunteer didn't have a regular treatment for his eczema site, we undertook a 55-day monitoring with our SFDI system. We also had control group imaging with his left hand with healthy skin condition during the whole monitoring period. The absorption and reduced scattering coefficient results in this section are calibrated with the same type of the

control group result to remove the environment influence on the skin with

$$result(day_n) = \frac{\text{raw result}(day_n)}{\text{control result}(day_n)} \times \text{averaged control results} \tag{5.3}$$

where the day_n is the certain day in the measurement period of time, the 'raw result' is the recovered optical properties from the target area, the 'averaged control results' is the averaged control group result for same type of the optical properties.

The timeline is shown in the Fig. 5.5.

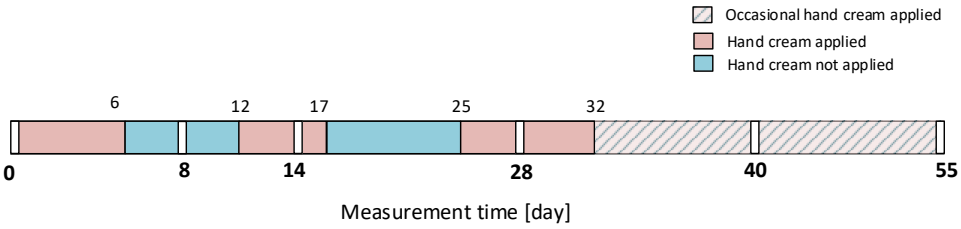

Figure 5.5: The eczema monitoring timeline with the history of applying the hand cream.

We utilised the SFDI system as described in the Section 5.1.1. Unfortunately, the 850 nm LED had poor collimation at the monitoring time making the optical properties map less reliable. We will use the result from 617 nm illumination for the most of this section.

Using the equation for the penetration depth Equ. 2.8, $f_x = 0.1$ mm^{-1} pattern has a penetration depth of 1.4 mm and $f_x = 0.3$ mm^{-1} has penetration depth of 522 μm at 617 nm. The average thickness of our volunteer's epidermis is around 135-148 μm based on his ethnicity and age group[171]. Referring to previous work[169], the eczema epidermis thickness can be up to 270-300 μm in the lesion area. Thus, these two values of f_x are feasible to distinguish the epidermis with higher f_x value and dermis with lower f_x pattern in the eczema area. The detection region is shown in the Fig. 5.6. By using a range of spatial frequencies, it is possible to obtain the average optical properties of the tissue for different depth ranges.

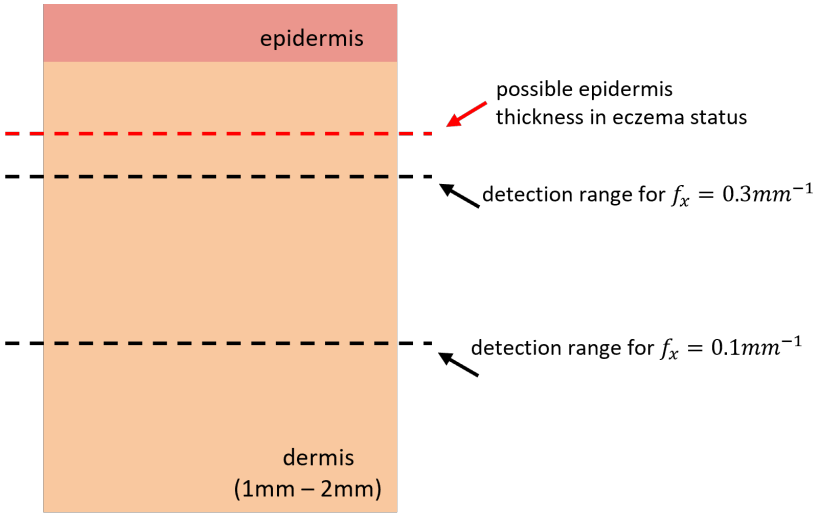

Figure 5.6: The detection range for the two values of f_x. The epidermis and dermis in the diagram is for healthy skin. The possible thicken epidermis in the skin is presented with with red dashed line.

5.2.2 Results

The VIS image, μ_a at 617 nm, μ_s' maps at 617 nm for two values of f_x are shown in Fig. 5.7. Due to the collimation issue in our 850 nm LED during the monitoring time, we are not showing the result from 850 nm illumination in this figure. The reduced scattering is expected to demonstrate a greater value in the dehydrated, chapped and cracked eczema area. The red patch probably introduces a higher μ_a value as the blood flow increases in the capillary.

On day 0, the eczema was relatively severe in condition whilst day 8 and day 14 had moderate eczema condition and dryness in the eczema area. The μ_s' map at f_x = 0.3 mm^{-1} for day 0 has better contrast demonstrating the eczema complications. The 'coarse' grainy high scattering coefficient patterns in both day 0 μ_a and μ_s' map may due to the excoriation, dryness and wear off in stratum corneum, matching the VIS image. Particularly, the high intensity μ_s' spots in the f_x = 0.1 mm^{-1} map may due to the damage in the dermis within the detection depth 1.4 mm. On day 8, the chapped and cracked skin condition in the eczema area is shown with the high reduced scattering pattern at f_x = 0.3 mm^{-1}. There are 'cracked' high

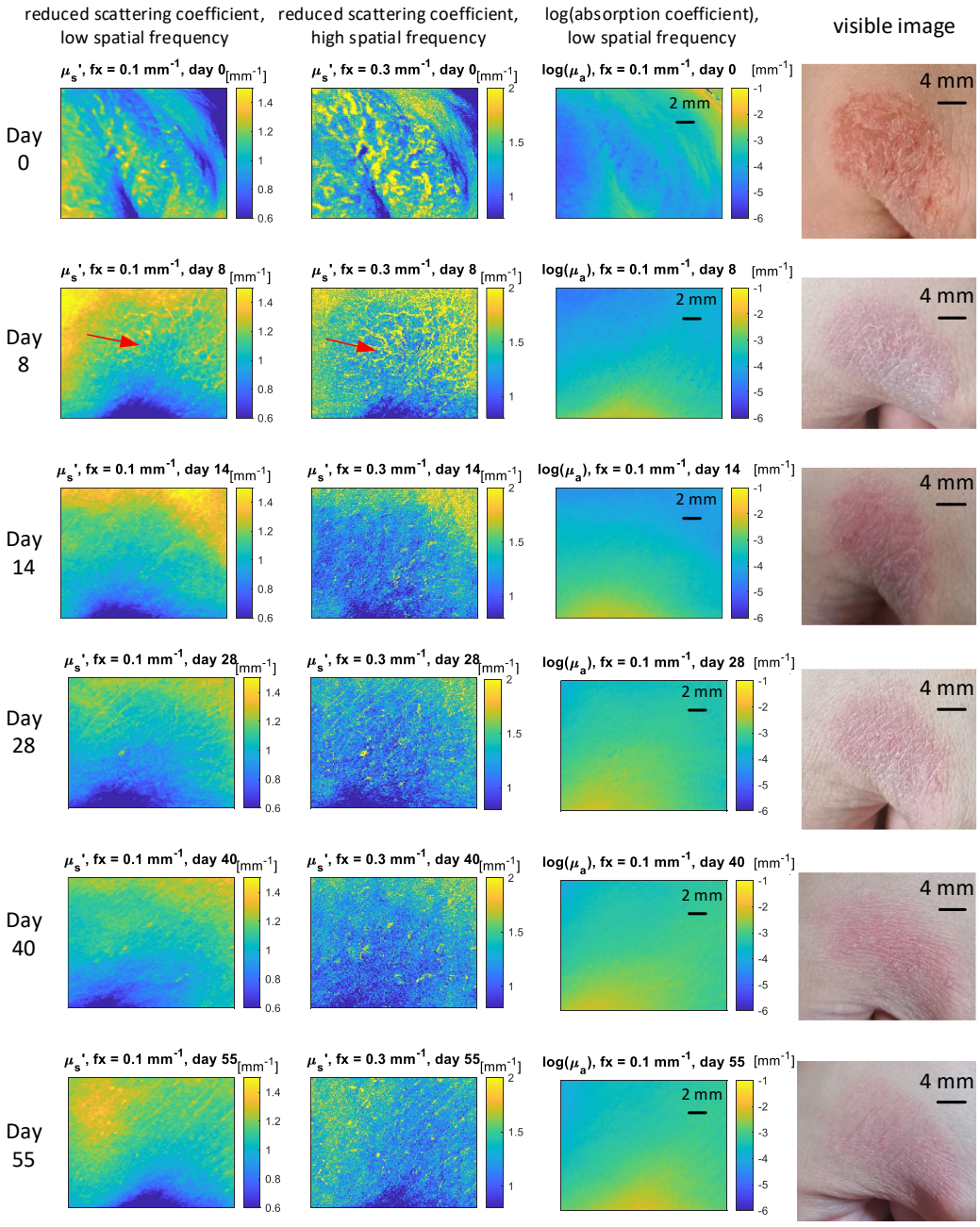

Figure 5.7: The eczema site observation from the day 0 to day 55. The same row is for the same day measurement and same column is the same optical property map. The first and second column from left is the reduced scattering μ_s' map at two spatial frequency $f_x = 0.1$ mm^{-1} and 0.3 mm^{-1}. The third column from left is the absorption μ_a map. The fourth column is the visible image for the eczema site.

scattering pattern in the $f_x = 0.3$ mm^{-1} map with good contrast while $f_x = 0.1$ mm^{-1} map had relatively minor area of meshed shape high scattering pattern. The reason behind might be the top middle area at day 8 had more superficial eczema (see red arrow). After day 8, the μ_s' map of $f_x = 0.1$ mm^{-1} no longer demonstrate noticeable change in eczema area.

The day 14 condition is not easy to estimate from the VIS image. However, the area with the 'cracked' high scattering pattern is reduced to a few tiny high scattering spots, meaning the eczema condition is improving, i.e. less damage in the epidermis. The day 28 showed a little relapsing in the skin condition where the cracks with high scattering μ_s' value are slightly visible. On both day 40 and 55, the eczema area have a mild condition. The day 55 has the best recovery in the skin barrier as shown in the VIS image and the μ_s' maps. There is almost no high scattering cracks in the $f_x = 0.3$ mm^{-1} map. Also the skin demonstrated less redness and better in moisture from the visual inspection. The target area has no cracks on skin from the VIS image and the μ_s' map only demonstrates a few high μ_s' value flakes or wrinkles. In the other way, the average daily temperature of UK rise gradually from 5°C to 12°C during the monitoring period. This hugely relieved the itchy and dryness feeling in the volunteer's skin.

However, the absorption map in 617 nm is not able to reflect the redness in the skin. The absorption μ_a maps only demonstrate evident variation value in the day 0 and appear uniform for the eczema area in the following days. The μ_a is therefore not sensitive to the structural or hydration change in chapped and cracked change in the skin. The average μ_a value increased for the eczema area over time. We will discuss this in the following section.

5.2.2.1 Eczema area scattering features

To have a closer look at the eczema, the exact pixel position of eczema influenced area was selected using imageJ. The histograms of both $f_x = 0.1$ mm^{-1} and

$f_x = 0.3$ mm^{-1} for the eczema area are shown in the Fig. 5.8. Here the occurrence of the certain μ_s' value (calibrated with the reference hand data) are presented with the probability in the histogram. The normalisation here is to avoid the influence from extracted pixel number difference in the different day in comparing the histograms.

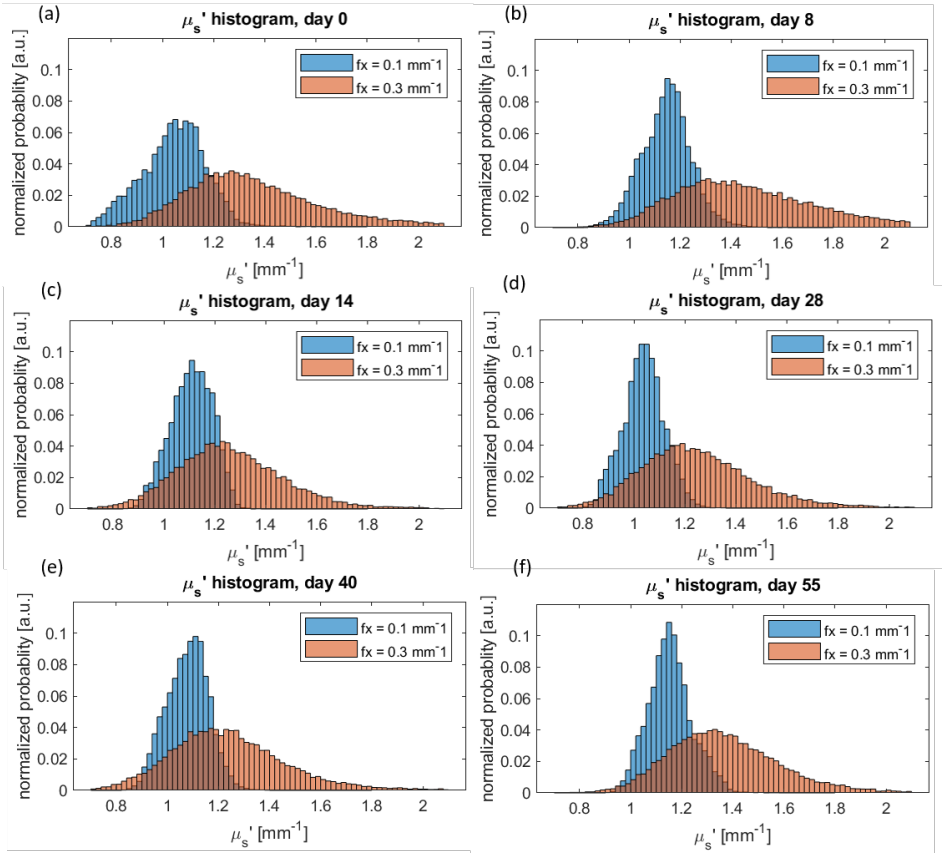

Figure 5.8: The histograms for eczema area μ_s' map at two value of f_x from day 0 to day 55. The normalised counts (probability) in each bar is the count in a class divided by the total number the selected eczema pixels.

On day 0 and day 8 (see Fig. 5.8 (a) and (b)), the peak of both the μ_s' probability distribution at $f_x = 0.3$ mm^{-1} are shifted to right side ($\mu_s' > 1.2$ mm^{-1}) indicating the epidermis is getting thicker in the eczema area. The histogram shapes are both flatter on day 0 and day 8. This indicates the excoriation damage in the epidermis via a lower μ_s' value. At the same time, the area of high μ_s' value in the eczema area is the thicken epidermis. Comparing the $f_x = 0.1$ mm^{-1} histogram, the probability

of the $\mu_s' < 0.9$ mm^{-1} occurrence is relatively higher on day 0 than day 8. This indicates the eczema area is improved in the day 8 where eczema becoming more superficial.

The VIS images on day 8 and day 14 are similar in appearance, causing it to be difficult to compare the condition. However, the histogram shapes for $f_x = 0.3$ mm^{-1} in Fig. 5.8 (b) are flatter than Fig. 5.8 (c). This once again demonstrates that on day 8 our volunteer had a drier and thicker epidermis in the eczema area matching disruption in the treatment from day 6. From day 14 onwards, the shapes of the histogram for both $f_x = 0.1$ mm^{-1} and 0.3 mm^{-1} become narrower meaning the eczema condition is becoming mild. This matches the moisture cream application history in the timeline.

The variance of the measurement σ^2 are calculated to evaluate the variability in the skin μ_s' distribution. The variance σ^2 was obtained from:

$$\sigma^2 = \frac{\sum_{i=1}^{n}(x_i - \bar{x})^2}{N} \tag{5.4}$$

where the x_i is each value in the each day measurement data set, $\bar{x}$ is the mean value of the mean value of the measurement, and N is the number of values in the measurement.

As shown in the Fig. 5.9, the day 0 and day 8 have the greatly higher value in variance which reflect the flatter shape of the histograms. The day 0 has both high variance in two f_x which may be a result of the damage skin exist in epidermis and dermis at the same time. The day 8 has much lower variance value at $f_x = 0.1$ mm^{-1} but high in $f_x = 0.3$ mm^{-1} demonstrating the eczema become more superficial than day 0. The variance value reduces sharply from day 14 and kept until day 55 which represent the eczema condition were significantly improved. Here, the variance curves match our observation in the eczema.

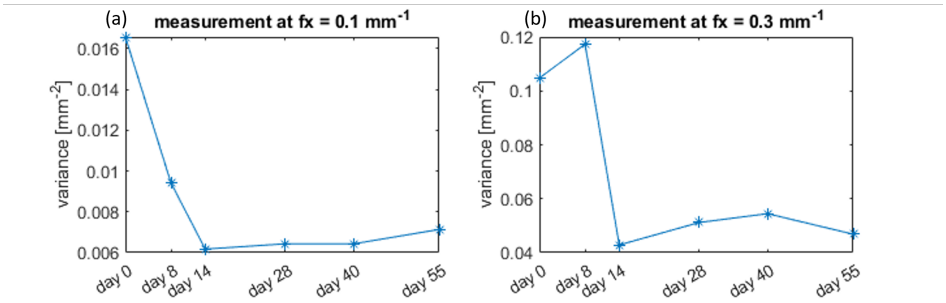

Figure 5.9: The variance calculated for each measurement day at (a) f_x = 0.1 mm^{-1}. (b) f_x = 0.3 mm^{-1} for 617 nm μ_s' map.

5.2.2.2 Eczema area absorption features

Using the eczema exact position, we plot the average eczema μ_a values at 617 nm and their standard deviation as an errorbar for two values of f_x in the Fig. 5.10. The μ_a reference value measured on the left hand is also included in the graph.

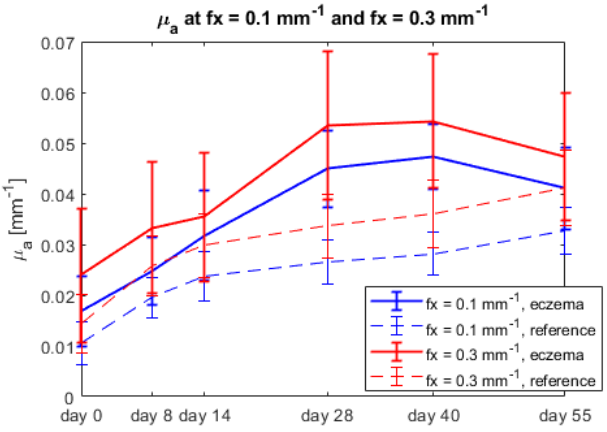

Figure 5.10: The μ_a curves for eczema area and reference at two f_x respectively.

The μ_a curve from the eczema site is always above the reference μ_a curve for both values of f_x. This shows the inflammation was present in the eczema area, matching the redness symptom. All μ_a curves in the graph show a gradual increasing change over time. The reason behind this is that environment temperature increased from the day 0 to day 55 resulting overall blood flow increase in the volunteer's hand.

From day 0 to day 14, the μ_s' indicate the eczema conditions are worse than the following days. However, both μ_a curves have relatively lower values possibly due

to the thicker epidermis making the μ_a harder to detect. The deviation in the eczema site at $f_x = 0.3$ mm^{-1} is largest due to the shallow detection depth and the uneven thickness of the capillary between the dermis and epidermis matching previous results[170].

It should be noticed that the eczema is located at the back of the hand between the thumb and second finger where curvature cannot be ignored. This curvature of the skin can affect the μ_a value detected in the eczema area as we can seen from the Fig. 5.4 and Fig. 5.7. This will slightly increase the average μ_a value of the eczema area.

5.2.3 Oxygen saturation for the eczema area

The oxygen saturation StO_2 value of the eczema area are calculated with the equation in the Section 5.1.2. Due to the collimation issue in our 850 nm LED during the monitoring time, the absorption results at 850 nm are noisy and with low SNR. The StO_2 maps shown in the Fig. 5.11 do not have good contrast. The worst area of eczema on day 0 shows relatively higher O_2 concentration matching the results from previous work[170]. The StO_2 value decreased slightly when the eczema condition became mild. Similarly to the absorption measurement, the thicker epidermis in the eczema area probably introduced an uncertainty in measuring the absorption. The uncertainty in the μ_a at some pixels even failed to recover the concentration of oxy-hemoglobin HbO_2 and deoxy-hemoglobin Hb.

5.2.4 Discussion

Based on our study of a single patient, SFDI method is not very sensitive to eczema. The contrast of the μ_a and μ_s' is only a promising indicator on moderate and severe eczema conditions. When the eczema became mild, the skin baseline condition was hard to control. The daily shower, hand washing or the portion of hand cream

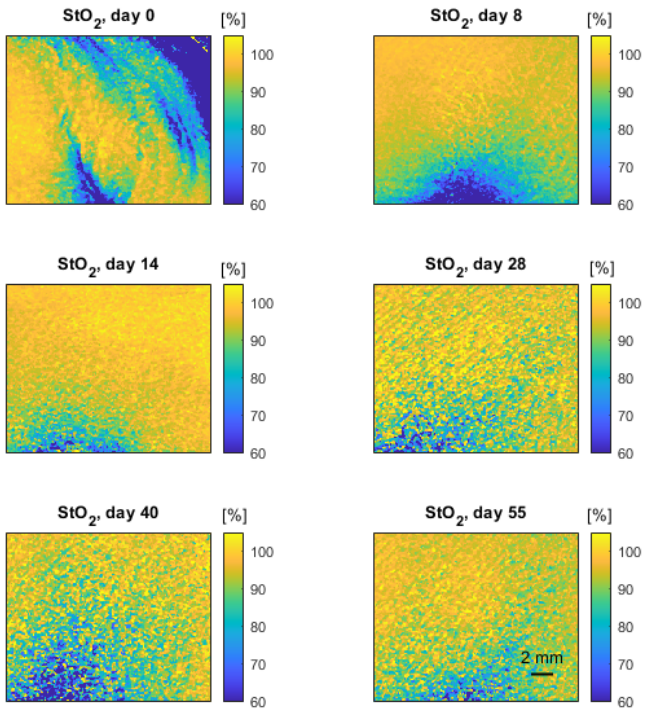

Figure 5.11: The StO_2 maps measured at the eczema area.

applied can vary day by day in our case. Especially for our volunteer who has no prescription or medical advice to follow in reducing the eczema.

SFDI has the potential to detect the variation in epidermis thickness and roughness. It has been used to measure the scars roughness with using a polarisation method[87, 86]. One may consider this in future works to improve characterisation of the eczema surface.

One may seek an improvement in the instrument as part of SFDI method to better aid clinicians. Eczema requires both shorter wavelength illumination, which cannot propagate down as far into the dermis and longer IR band wavelength illumination adding into SFDI system. Selecting a longer IR band is also significant for measuring the water content which is another key criteria in eczema.

5.3 SLS experiment

Sodium lauryl sulfate (SLS) is an anionic surfactant widely used in the personal care, cleaning and cosmetic products. In the dermatology field, acute irritant contact dermatitis (ICD) on skin is experimentally modelled using SLS. Acute ICD is a nonspecific response of the skin to chemical stimuli, e.g. soap, detergents, solvents and oils[172], that releases mediators of inflammation, predominantly from epidermal cells[173].

Exposure to SLS introduces a toxic effect to the keratinocytes leading to disruption of the skin barrier and lipid synthesis[174, 175]. The skin barrier disruption then triggers an immune system response leading to cytokine release from epidermal cells and an inflammatory reaction[176, 172]. Upon this process, the skin barrier begins restoration by proliferating keratinocytes and forming lipids.

The histopathological effects of SLS depends on the concentration, exposure time and target skin area[177]. SLS has cumulative toxic effect on the skin causing the acute irritation which will recover once the SLS exposure is suspended. The SLS exposure is expected to trigger skin symptoms include increasing in the blood flow[178], water loss and irritant response.

We apply a short-time SLS exposure to the dorsum skin that triggering a positive ICD[179] but not into the severe irritant response regime[174]. The SFDI system we built in Section 5.1.1 was used to measure the optical properties of the SLS exposed area as the target area.

5.3.1 Protocol

Here we recruited six volunteers with type 2, 3 and 4 type of skin from ethnicity groups Asian and White Caucasian in the age range 22 to 30. Four male and two females were involved in the experiment. We expected to see the irritant reactions, i.e. erythema, scaling and roughness from the volunteer's skin. Spatial frequencies

f_x of value 0.1 mm^{-1} and 0.3 mm^{-1} were utilised in the SFDI method to recover the reduced scattering μ_s', absorption μ_a maps and relative level of oxygen (StO_2) on the back of their hand. The steps for the imaging experiment are listed as below:

- The volunteers were asked to wash their hands with commercial hand wash liquid for 20 seconds and air dry to remove grease on their hands. The hand pictures were taken with a conventional visible camera and SFDI system before applying any chemicals on the hand.
- 1 ml 2% (m/v) sodium lauryl sulfate (SLS) solution was applied with a cotton bud to the right hand dorsal, covering by the cling film to prevent any vapour from escaping. This was kept on for one hour on the volunteer's hand.
- After the cotton bud and cling film were removed from the hand, the skin site was cleaned and dried with tissues.
- Commercial hand cream was applied to restore the skin water content and we let the volunteer's skin recover for 15 minutes.
- The back of right hand is imaged by the conventional visible camera and SFDI system after 15 minutes.

The volunteers were asked not to wash their hands (at least not the experimental site unless necessary) during the one hour and 15 minutes experiment. They were advised to stay in the room with a stable temperature of around $20°C$ during the experiment. Therefore the room temperature and humidity can be regarded as constant during the experiment. The imaging was only conducted when the SLS exposed area was air dried to avoid the possible hydration of the skin. Spatial frequency $f_x = 0.1$ mm^{-1} and 0.3 mm^{-1} are used for the imaging experiment. The appSFDI[147] was utilised for the μ_s' and μ_a recovery.

5.3.2 Results

The visible (VIS) irritation results and feeling reported by the volunteers are listed in Table. 5.2. The redness reported there were all within the SLS application area demonstrating a well-demarcated erythema pattern. We also added the note in the right column as we had volunteers who had a history of dermatitis on their back of hand.

Table 5.2: The response from the volunteer during the experiment.

Volunteer	after 1 hour	15 minutes recovery	notes
S1	feel itchy redness	feel normal half redness gone	
S2	feel normal no significant change	feel normal	
S3	feel sting redness	feel dry half redness gone	dyshidrotic eczema
S4	feel normal few pores show redness	fully recovered	
S5	feel normal no significant change	fully recovered	
S6	feel normal redness	feel normal 30% redness gone	seasonal eczema

Comparing the irritation response in the skin, four of six volunteers reported redness appearance after one hour of SLS exposure. Two volunteers both felt normal and there was no change in the skin structure or colour. After 15 minutes recovery, the redness for the volunteer S4 was fully recovered. Volunteer S1, S3 and S6 had redness partly relieved visibly. Combining the skin symptoms and the feeling reported, we find the individual feeling is subjective due to people have different pain thresholds. Volunteer S6 had no feeling even with the most severe redness shown on the skin. Thus, we are using the absorption and reduced scattering coefficients and the StO_2 value to observe the change in the volunteers' skin rather than relying entirely on a subject feeling.

5.3.3 Optical property feature

The reduced scattering μ_s' and absorption μ_a maps are recovered for the three sets of imaging of each volunteer. The average μ_s' and μ_a values from two wavelengths and two values of f_x measurement are calculated with SLS exposed area excluding the veins.

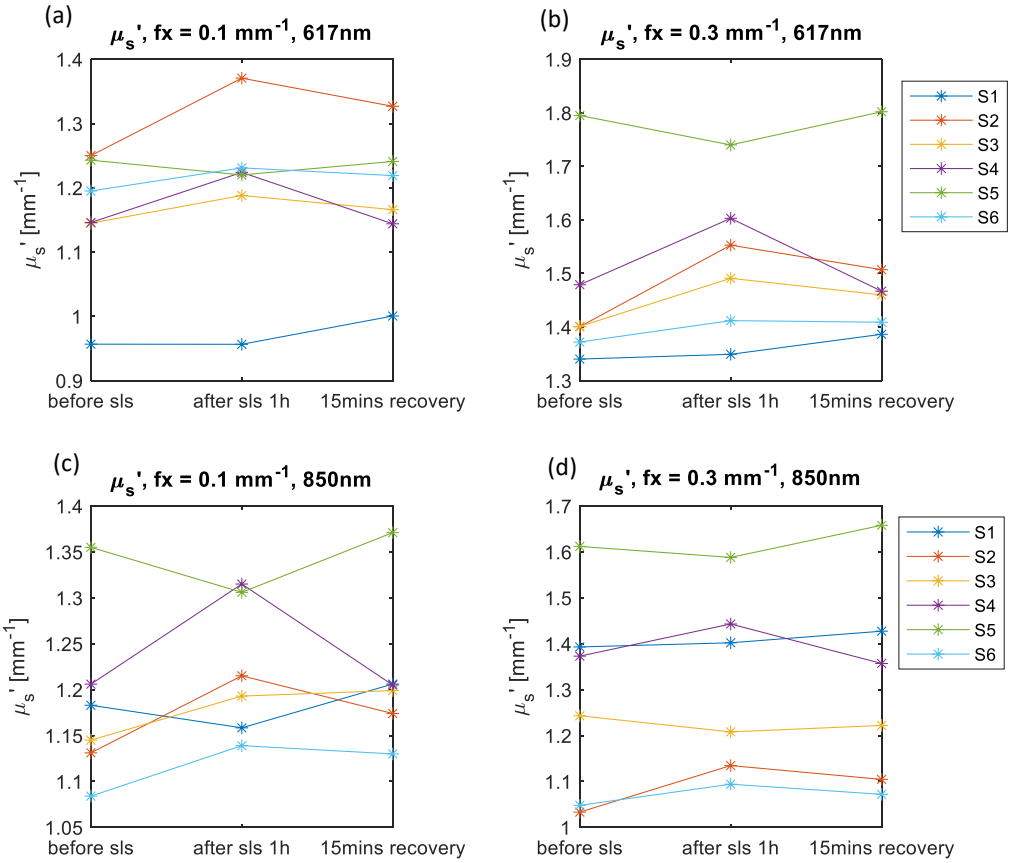

Figure 5.12: The μ_s' results from six volunteers at three states: before the SLS is applied, after the SLS is applied for one hour and recovery for 15 minutes.

The μ_s' average value for three states in the experiment is shown in the Fig. 5.12. Most of the volunteers demonstrate inverted U shape in the μ_s' curve in the 617 nm measurement results with a peak value after SLS application. This may indicate the epidermis is losing water after the SLS exposure. Also, as we introduced in Section 5.2, the μ_s' may increase when the skin becomes dehydrated. Except from the volunteer S5, other volunteers' skin demonstrated an increase in the μ_s' value

after the SLS is applied. The following μ_s' after recovery for 15 minutes drops. The volunteer S5's skin shows a inverse trend when his hand possibly becoming hydrated during the SLS irritation.

In Fig. 5.12, the order of the μ_s' curves on the each graphs are different while the trend with the μ_s' value change via three states is similar for the same volunteer. This may indicate trans-epidermis water loss (TEWL) or the skin permeability varying between the individuals as well as the epidermis thickness. As we discussed in section 5.2, the μ_s' is sensitive to the structural change. The SLS exposure has been reported in previous work to lead to premature keratinization and widen the stratum granulosum's intercellular space[174]. The change within the skin is complex and using μ_s' alone is a long way from being sufficient to characterise the changes.

The μ_a value is shown in the Fig. 5.13. All the curves show a U-shaped trend except from volunteers S2 and S5. This matches their symptoms reported after the SLS exposure of no redness appearing. S5 and S2 both have a straight descending line for the three experimental states. S5's skin demonstrates an inverted trend in the 850 nm measurement result. The trend and the order of the curves of other individuals are almost similar in the Fig. 5.13 (a) - (d). The reason behind this might be that the chromophores, i.e. the hemoglobin and melanin, which are sensitive to the wavelength we use, are within the four detection ranges here. As the wavelengths we use are not sensitive to the water, the water loss due to the SLS will not be shown in the μ_a results.

5.3.4 Hemodynamic observation

Then the oxygen saturation (StO_2) was calculated with the absorption coefficient μ_a at two wavelength as described in Section 5.1.2. As shown in Fig. 5.14, the StO_2 values are much higher when measured by the lower spatial frequency f_x as it can penetrate deeper into the dermis which contains more vessels. The StO_2

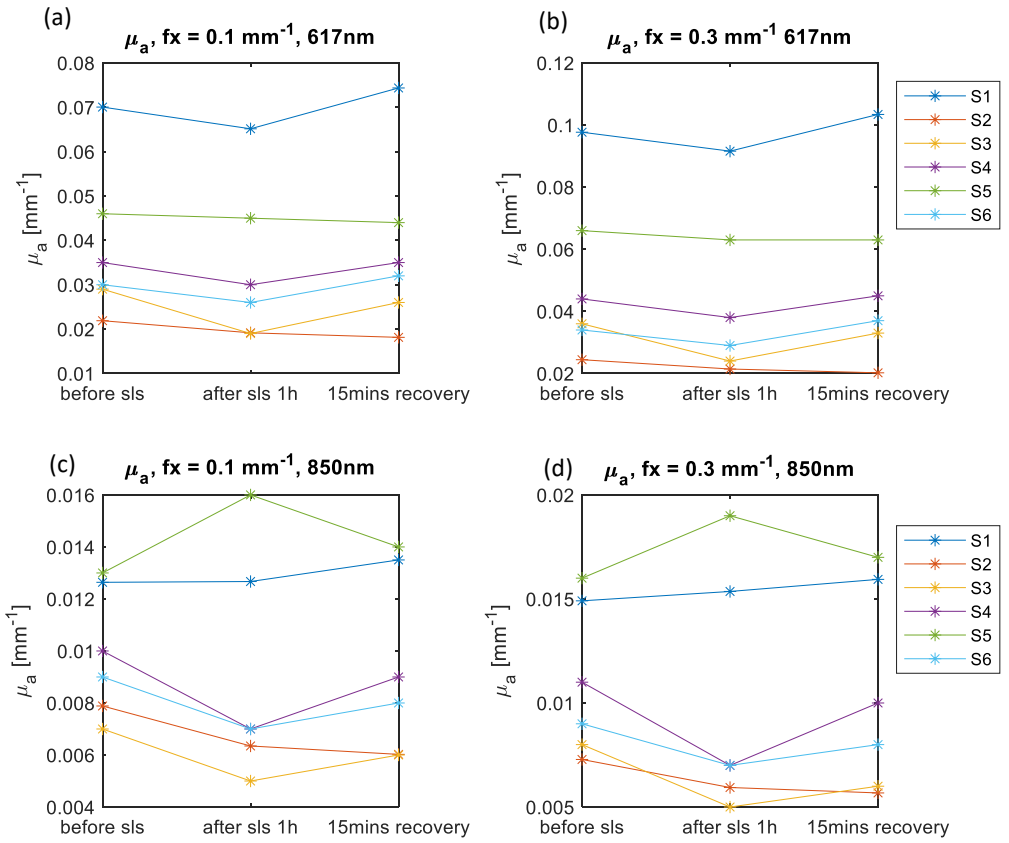

Figure 5.13: The μ_a results from six volunteers at three states: before the SLS is applied, after the SLS is applied for one hour and recovery for 15 minutes.

results at $f_x = 0.1$ mm^{-1} and 0.3 mm^{-1} both demonstrate an increasing trend after the SLS was applied. Then the StO_2 value decreases after the 15 minutes recovery period. This matches the redness relief reported by the volunteers S3, S1 and S6. Also this indicates the immune cell response in the inflammation with the consumption of the oxygen is increased. The volunteer S2's skin showed no significant change in the StO_2 where the inflammation was possibly negligible in his epidermis. The volunteers S4 and S5 reported no redness and normal feeling in the SLS application site but the StO_2 still demonstrates a slightly increasing and decreasing trend through the three states. It is worth noting that volunteer S1 has a type 4 skin meaning the background melanin absorption is significant and make it hard to determine an accurate StO_2 (see Equ. 5.1). Therefore S1's StO_2 value

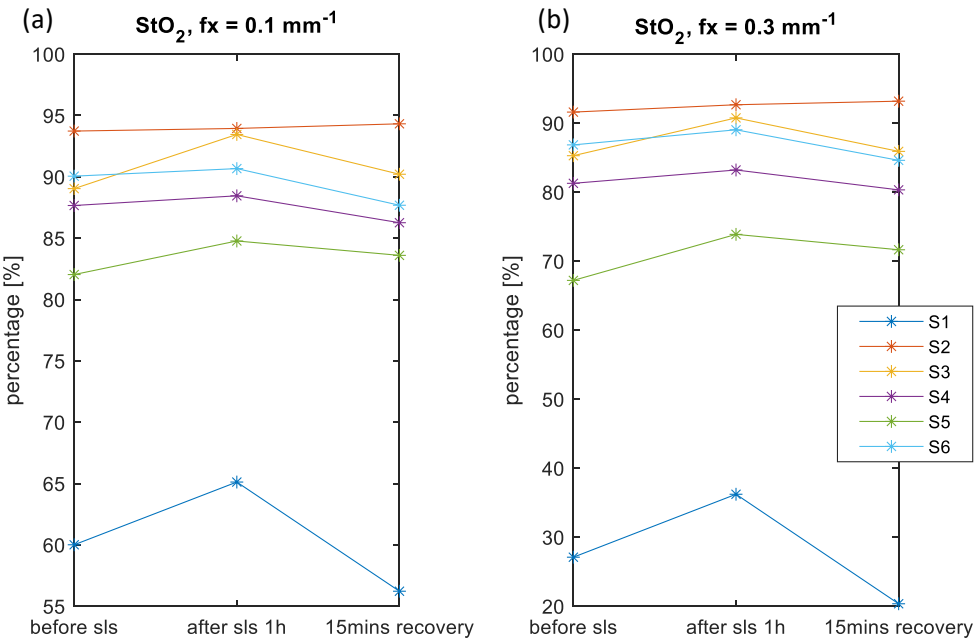

Figure 5.14: The StO_2 calculation results from six volunteers at three states: before the SLS is applied, after the SLS is applied for one hour and recovery for 15 minutes.

is significant lower than other volunteers.

Table 5.3: The StO_2 value [unit: %] difference measured by $f_x = 0.1$ mm^{-1}.

Volunteer	$StO_{2,s1} - StO_{2,s0}$	$StO_{2,s2} - StO_{2,s0}$	$StO_{2,s1} - StO_{2,s2}$
S1	5.1	-3.8	8.9
S2	0.2	0.6	-0.4
S3	4.4	1.2	3.2
S4	0.8	-1.4	2.2
S5	1.5	1.1	0.4
S6	0.6	-2.4	3.0

Table 5.4: The StO_2 value [unit: %] difference measured by $f_x = 0.3$ mm^{-1}.

Volunteer	$StO_{2,S1} - StO_{2,S0}$	$StO_{2,S2} - StO_{2,S0}$	$StO_{2,S1} - StO_{2,S2}$
S1	9.1	-6.7	15.9
S2	1.1	1.6	-0.5
S3	5.5	0.6	4.9
S4	1.9	-1.0	2.9
S5	5.5	3.9	1.6
S6	2.2	-2.2	4.4

To look at the oxygen level closely in the three states in the experiment, we calculate the difference in the StO_2 between states as in the Table 5.3 and Table 5.4. The uncertainty of the StO_2 measurement is around ± 0.3%[180]. The uncertainty of the StO_2 is calculated from repeated back of hand imaging (repeating: put hand in for imaging and then hand take out) for the same target area for 10 times. The StO_2 level in three states here are initialled as: before SLS is $StO_{2,S0}$, after SLS for 1h is $StO_{2,S1}$ and recovery for 15 minutes is $StO_{2,S2}$. The StO_2 rate increasing possibly demonstrates the inflammation condition in the skin after SLS exposure. The higher spatial frequency results have greater difference between the states as the inflammations is happening in the superficial layers.

Looking at the fourth column in the two tables, we find the SLS susceptibility is dependent on the individual. People reported redness in the skin, even very minor redness in the pores, as volunteer S4 stated, showing a high value difference between $S1$ and $S2$. Again, volunteers S5 and S2 have minor inflammation in their skin demonstrating a very small StO_2 change between states. Especially, two volunteers S3 and S6 with reported skin complications demonstrate stronger inflammation response after SLS exposure. This matches the fact that individuals with atopic tendencies are more susceptible to ICD[173]. The recovery in the inflammation validate the fact that SLS has cumulative toxic effect on the skin. When the exposure is removed, the skin inflammation starts to heal.

5.3.5 Discussion

From the experiment results above, SFDI demonstrates a potential to measure the SLS exposure on skin. Using the two wavelengths and two spatial frequencies, we detected the optical features of the skin at different depths. The μ_s' and μ_a curves clusters demonstrate various trends and order which reflect the skin barrier structure and corresponding chromophores are disturbed in different ways. The SFDI aids in detect the inflammation for the oxygen saturation changes.

The response to the SLS exposure varies among the race and skin condition. Genetic factors also play an important role in relation to a cytokine response which is key to the initiation of the inflammatory response[172]. We had three volunteers with positive response and two volunteers with very minor or no response to the SLS exposure. There was also an abnormal individual who showed an inverted trend compared to other volunteers. This may due to his epidermal thickness and his skin barrier condition. The application of the SLS here may create a humid environment for his skin.

The SFDI system here is still not sufficient to completely characterise the SLS exposure as acute ICD is very complex in terms of the immune pathways and inflammatory mediators[181]. Most of the dermatological studies with the SLS utilise trans-epidermal water loss (TEWL) to measure the water loss in the skin and the wavelengths we used are not sensitive to the water changes. Also the SFDI is not able to measure the blood velocity change. We are looking to upgrade our instrument to add wavelengths sensitive to lipid and water[182]. We need further optical methods[183], e.g. laser doppler imaging (LDI) for blood velocity, combine with and upgrade SFDI system as we discussed in the previous section for eczema monitoring.

5.4 Biopsy wound observation

5.4.1 The wound information

We had a volunteer with a incisional biopsy wound due to a suspected skin cancer site on his right hand. The volunteer is a male with Fitzpatrick skin type 2. He was 57 years old with smoking history for 37 years (leads to a higher incidence of wound infection) at the time of measurement. The biopsy area was reported to have a tender feeling.

During the volunteer's skin biopsy, the target area was opened by the scapulae

then the suspected lesion area was sampled. Then the wound was sealed with non-absorbable suture. The biopsy was taken 14 days before we started the imaging experiment. The wound was suspected to get infected on the day 0 of our observation and our volunteer was prescribed to take oral antibiotics for 5 days. We had a 42 day observation of his wound healing progress until his wound was visibly healed for 3 weeks. The timeline for the surgery and the SFDI monitoring is shown in the Fig. 5.15.

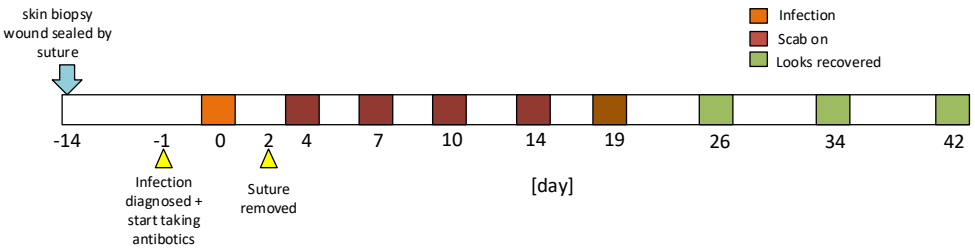

Figure 5.15: Timeline for the wound healing and the monitoring. The wound was monitored every three or four days before the scab came off as the wound condition changed rapidly at this stage. The healed wound area was then imaged with seven day interval as the tissue reformation stage takes place slowly.

The wound area was measured at the centre and the left hand was measured at the same time as a reference and calibration of the daily skin condition which can be influenced by the skin moisture, oil and environment temperature which can change the blood flow[184]). The spatial frequency f_x used for wound imaging was $f_x = 0.1$ mm^{-1} to achieve the 1 to 2 mm depth detection.

5.4.2 Measurement

Prior to the optical properties recovery for the wound area, the AC images are firstly binned with 5×5 window to remove the noise and maintain details for the wound. Then the Scale-invariant feature transform (SIFT)[185] module was applied in the Fiji software for local feature description. The established matches are filtered using the Random Sample Consensus (RANSAC)[186]. Using the matched points, the motion artifact during the two wavelength measurements are registered for

the subsequent inverse method. The absorption and reduced scattering map are recovered from the registered AC image with the appSFDI[147] software. The calculated reduced scattering and absorption coefficients are then calibrated with the Equ. 5.3 to remove the influence of environment.

5.4.3 Infection observation

The wound had been diagnosed with infection on day 0 of our observation. The visible (VIS) picture of the wound on day 0 is shown in the Fig. 5.16 (a), the μ_s' map at 617 nm is shown in Fig. 5.16 (b) and the μ_s' map at 850 nm is shown in Fig. 5.16 (c).

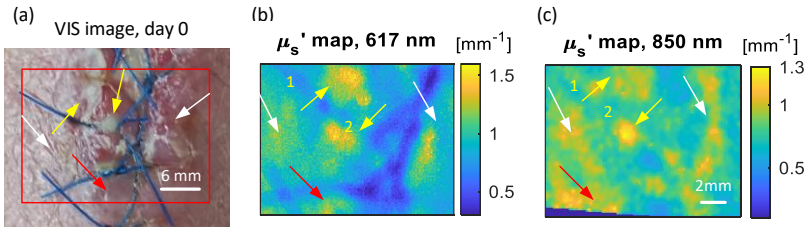

Figure 5.16: (a) The VIS picture taken for same area of the wound at day 0. The red rectangle area is the area shows in the μ_s' maps. (b) The reduced scattering μ_s' map at 617 nm for the wound at day 0. (c) The reduced scattering μ_s' map at 850 nm for the wound at day 0. The yellow arrows shows the pus indicated by the high reduced scattering coefficient. The red arrows show the area potential area with pus hard to be seen by raw eye but can be seen from the μ_s' map. The white arrows point out the area have pus developing underneath can be seen clearly in 850 nm μ_s' map but hard to notice in 617 nm μ_s' map and VIS image.

The wound site demonstrates the pus (in white spots) and redness near the suture sites after the biopsy conducted 2 weeks previously. As pointed out by the yellow arrow, the pus has high scattering coefficients shown in both of the μ_s' maps. The pus is formed by dead bodies of the white blood cells filling the cavity or space created by the breakdown of the tissue. Thus, μ_s' is sensitive to the structure change in the wound due to pus. As indicate by the red arrows, there was pus developing where there were three spots with a high scattering coefficient but only showing redness in VIS image. Thus, SFDI is more sensitive to the infection than

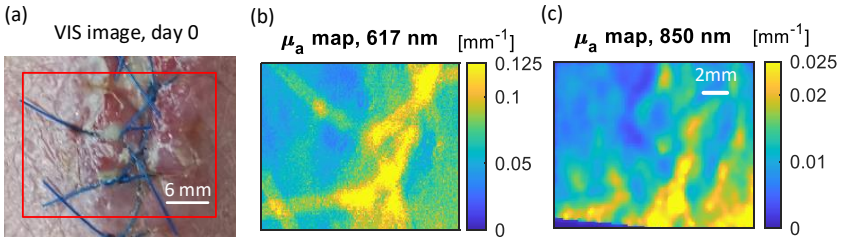

Figure 5.17: (a) The VIS picture taken for same area of the wound at day 0. The red rectangle area is the area shows in the μ_s' maps. (b) The absorption μ_a map at 617 nm for the wound at day 0. (c) The absorption μ_a map at 850 nm for the wound at day 0. The suture had different absorption coefficient at two wavelength.

the naked eye. The area of pus looks larger in the μ_s' maps, i.e. the condition of infection was more severe than the naked eye can see. However, the redness around the wound had no significant sign in the μ_s' map where the μ_s' is not sensitive to the blood flow and vessel changes.

By applying dual wavelengths, we can observe the profile of the wound structure at different depths. The longer wavelength light penetrates deeper into the tissue than the shorter wavelength. The site 1 and site 2 demonstrate similar levels of high intensity in the 617 nm μ_s' map. However, in the 850 nm μ_s' map, site 2 shows greater intensity than site 1. As site 2 formed a deeper cavity with pus so had a worse infection condition than site 1. When the pus is developing underneath, the 850 nm wavelength could sample deeper so the pus site can be seen much earlier as demonstrated with the white arrows. Here the μ_s' map is capable of detecting the structure change within the wound.

In the absorption μ_a maps in Fig. 5.17, the pus area has vaguely lower intensity at both wavelengths. The pus covers a larger area in the μ_a maps than in the μ_s' maps. The difference in the healthy skin and infection site is not evident compared to the μ_s' maps. Thus, the μ_a maps are not sufficient to characterise the infection in the wound. We will discuss the application of μ_a maps later in the Section 5.5.2. Therefore, the SFDI is feasible to detect the infection developing in the early stage using μ_s' and μ_a.

5.5 Wound healing progress

The μ_a map, μ_s' map and VIS image for the wound area are shown in the Fig. 5.18. From the VIS images, at day 4 of observation, the wound area looks red in appearance. This indicates the capillaries were forming with the dermal replacement. The scab gets thicker from day 7 to day 10 shown by both VIS picture and relatively higher absorption value in the absorption maps. The low reduced scattering coefficient in the wound area indicates the collagen fibre are dissolved in the wound healing progress. The edge of the wound area always has a high reduced scattering due to re-epithelialization. With time passing, the low scattering area shrinks day by day, showing the wound was healing in the right direction and contracting gradually.

Particularly, on the day 14, the scab had lifted around the edge of the wound. The VIS images are not able to show the progress as the scab is not transparent to the naked eye. The SFDI method could get through the scab, though it had a relatively high reduced scattering coefficient and absorption coefficient. The reduced scattering recovery is still able to provide a reliable result as the scab is thin. The accuracy of the absorption recovery may decrease[6] as the absorption value is always a much lower value (around 10 to 100 times less) than the reduced scattering. When the scab lifted at the edge, the incident light is reflected several times in the thin air layer between the scab and skin. Therefore, the absorption coefficient demonstrates a high value in the area. Hence, SFDI aids in earlier detection for the wound healing progress than the naked eye's capability. When the scab had fallen off from the wound from day 19 to day 42, the regeneration was ongoing. Specially, in day 26 and 34, there are few high reduced scattering spots at the edge of wound in μ_s' map at 617 nm may due to the formation of the suture scar. The high scattering value indicates the collagen fibres are growing and transforming in type.

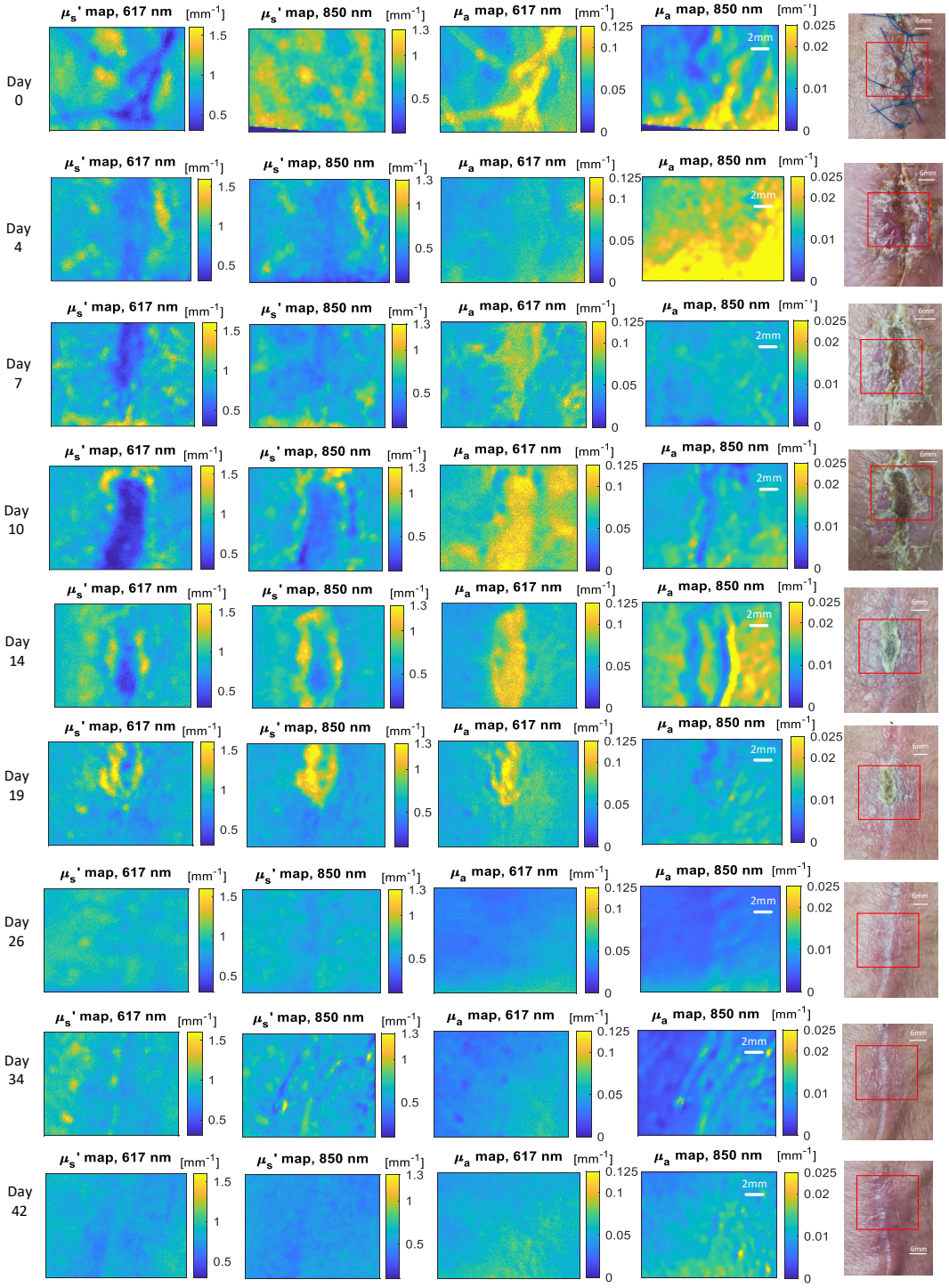

Figure 5.18: The wound healing pictures from the day 0 to day 42. The same row is for the same day measurement and same column is the same optical property map. The first to forth column from left is the recovered optical properties map at two wavelength.The fifth column from left is the VIS picture for the whole area of the wound site. The red rectangle is the area imaged in the optical property maps.

5.5.1 Physiological observations

The percentage of wound healing is defined as[187]:

$$percent\ healing = \frac{original\ wound\ area\ -\ wound\ area}{original\ wound\ area} \tag{5.5}$$

Using this equation, the wound recovery process measured by the VIS image, 617 nm and 850 nm reduced scattering map is plotted in the Fig. 5.19 for day 0 to day 19. The wound area from the 617 nm and 850 nm scattering maps are selected from the lower scattering area of the wound centre.

After processing the images, it was noticed that the interested wound area in day 7 was not all recorded in the SFDI output images. Therefore, we need the visible image to determine the unrecorded area. We assumed the wound area in VIS image and μ_s' map is similar, then the measures of two alike wound corresponding area are proportional. We obtained the the ratio of the area both VIS and μ_s' have in part of wound. We therefore scaled the interested area in VIS image to estimate the corresponding missed area in the μ_s' map. This estimation provides a data point that fit smoothly on the healing area count in the Fig. 5.19 and was believed to be a suitable approach to the problem.

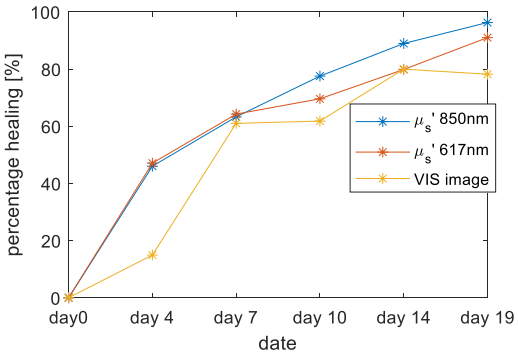

Figure 5.19: The percentage of healing measured from the VIS image, 617 nm reduced scattering map and 850 nm reduced scattering map.

The VIS image indicates slowest healing rate while the 850 nm illustrates the fastest healing rate. The 617 nm and 850 nm μ_s' map determine the wound has been

healed in right direction deeper than naked eye can see. With the SFDI method, one can detect the healing progress earlier and at different depths by changing the wavelength. The 617 nm and 850 nm scattering map healing results overlapped from day 0 to day 7 and then separate till the wound is visibly healed. The split point here is also the day we observed the scab started to appear in the wound site which marks proliferation, the third phase, of wound healing. As the wound contracts from the edge to the centre while from bottom to the top forming a triangle/trapezoid shape matching the Fig. 1.4 in the Section 1.2 and the diagram in the Fig. 5.20.

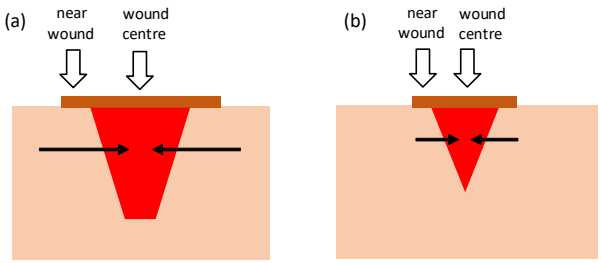

Figure 5.20: The wound healing progress model[4] showing the wound contraction in the wound healing from (a) to (b) when wound healing in the right direction. The actually wound margin (red area) underneath is narrower than the wound margin seen by the naked eye (dark brown area). The wound centre and the tissue around wound for measurement area shown by the arrows to be observed closely with the optical properties.

Looking closely, we select the wound centre to look at the average absorption coefficient μ_a and reduced scattering coefficient μ_s'. As shown in the Fig. 5.18, the wound centre is located from the relative low μ_s' area in the centre of the wound. The μ_a variation with time for two wavelength is shown in the Fig. 5.21 and the μ_s' is shown in Fig. 5.22. The error bar is calculated with the standard deviation of optical properties value in the selected area.

Unfortunately, μ_a for 850 nm had no significant change in the value through the wound healing process as the main chromophores all have a low μ_a value at this wavelength matching the knowledge in Chapter 2. The 617 nm has a greater μ_a for same concentration of both oxy-hemoglobin (HbO_2) and deoxy-hemoglobin

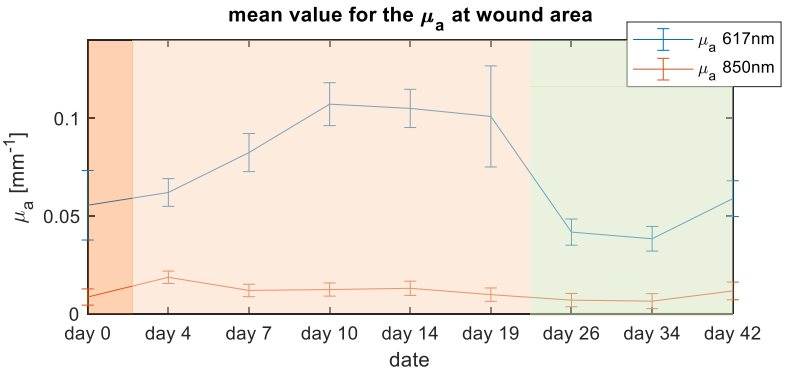

Figure 5.21: The absorption coefficient μ_a at 617 nm and 850 nm at the wound centre. Three phases of the wound healing is marked with orange: infection, light orange: inflammation and proliferation, green: visible healed with the scab off.

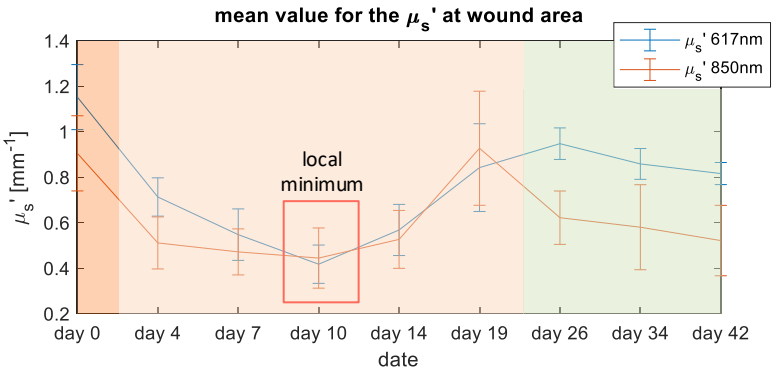

Figure 5.22: The reduced scattering coefficient μ_s' at 617 nm and 850 nm at the wound centre. The errorbar is the standard deviation. Three phases of the wound healing is marked with orange: infection, light orange: inflammation and proliferation, green: visible healed with the scab off.

(Hb) than 850 nm. As the volunteer had a light-colored skin (volume fraction of the melanin around 1%[24]) which aids in reducing the absorption effect by the melanin. At the same time, the water absorption coefficient is negligible at 617 nm wavelength and we can assume the melanin is uniform in the target area. Thus, the μ_a value at 617 nm presents the total hemoglobin concentration (HbO_2 + Hb) indicating blood content in the skin with good signal noise ratio (SNR).

The absorption coefficient μ_a at 617 nm gradually elevates from the day 0 to day 7 when there are capillaries and vessels growing in the wound area to increase the

blood volume. The μ_a value stays stable from day 10 to day 19 probably due to the scab dominating the absorption. After day 19, the scab came off from the wound site showing the wound is visibly healed and into the final stage of the wound healing process. The decreasing in μ_a value at 617 nm shows the decline in the new vessel generation in the final stage of wound healing as this wavelength is sensitive to the hemoglobin.

Correspondingly, the reduced scattering coefficient μ_s' has a trend with both wavelengths matching the μ_a change. The low scattering coefficient indicates the collagen disposition inside the wound site. Both scattering curves decrease and approach the local minimum at the day 10 where the the absorption curve at 617 nm reaches the local maximum. The results together may illustrate the beginning of the third phase of wound healing, i.e. proliferation. Also there is a gradual changes in the distance between the two curves showing the speed of wound healing with depth is different, matching the 3D model of wound healing. The errorbar is greater than others in day 19 as most of scab is lifted off from the wound site making the margin of the wound blurred on the μ_s' maps. Both scattering curve rise from the day 10 to day 19 as the wound contracted and turns into the remodelling phase (third phase) of wound healing. The distance between the two curves becomes fairly equal from day 19 showing the structure change underneath occurring synchronously.

To compare the optical properties between the wound and the tissue around the wound, the tissue around the wound area is selected with approximately a 1 mm width, is selected as shown in the Fig. 5.20. As the 850 nm wavelength has lower μ_a with hemoglobin than 617 nm, we only plot μ_a for the wound area and around the wound area at 617 nm in the same graph in Fig. 5.23. The reduced scattering at two wavelengths for the area near the wound is shown in the Fig. 5.24.

In the Fig. 5.23, the value of μ_a near the wound is lower than μ_a in the centre of the wound from day 4 to day 26. The difference between the value $\mu_{a,617nm} - \mu_{a,850nm}$ increases until day 10 and stays stable until day 19. The two curves reach the local maximum and start dropping synchronously.

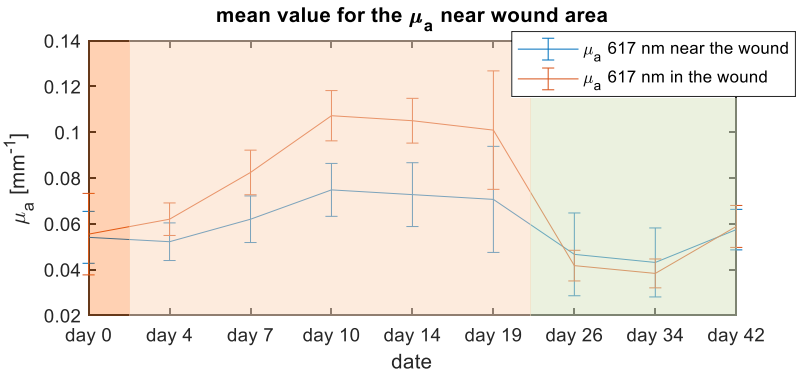

Figure 5.23: The absorption coefficient at 617 nm comparing the wound centre and around wound area. The errorbar is the standard deviation. Three phases of the wound healing is marked with orange: infection, light orange: inflammation and proliferation, green: visible healed with the scab off.

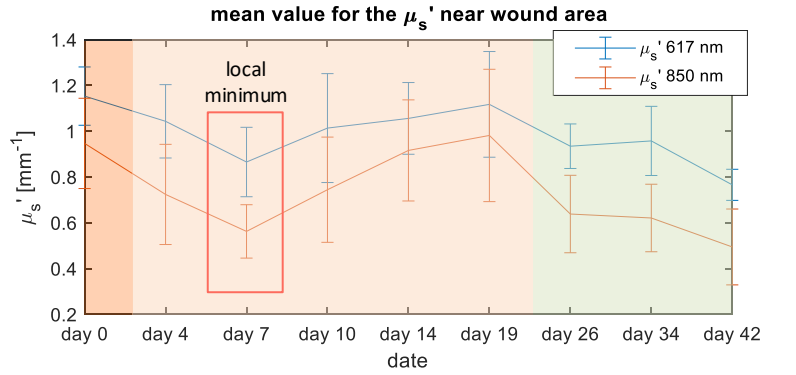

Figure 5.24: The reduced scattering coefficient at 617 nm and 850 nm at the wound centre. The errorbar is the standard deviation. Three phases of the wound healing is marked with orange: infection, light orange: inflammation and proliferation, green: visible healed with the scab off.

In the Fig. 5.24, the trend for the μ_s' is similar for the two wavelengths. The distance between the two curves is more constant than in the Fig. 5.22. The local minimum is reached at day 7, earlier than the μ_s' curves for wound centre (at day 10). This fits with the wound healing model in the Fig. 5.20 that the wound is healing from the outside to the inside.

5.5.2 Hemodynamic measurement

The oxygen supply plays a vital role in successfully wound healing. The numerous biological processes demand an adequate oxygen supply, for example proliferation, pathogen patrol and protein synthesis. The appropriate oxygen level also triggers the tissue healing response[188, 189]. Therefore, along with the structure change and blood supply in the wound, we also observe the hemodynamic profiles in the wound site with the method described in the Section 5.1.2. This will also aid clinicians in understanding the progress in the wound healing.

The maps for the StO_2 are shown in the Fig. 5.25. On day 0, the oxygen level at the infection site is very high indicating huge oxygen consumption by the inflammation cells defending against the bacteria. The wound area near the sutures are relatively low matching the hypoxia in the inflammation phase. This is probably also an indicator of the delay in wound healing. When a surgical wound is formed, the disruption and damage in vessels creates a hypoxic environment due to the consumption of the metabolically active cells. This relatively low oxygen level status initiates the wound healing process where the fibrin is formed. At this stage, the tissue stays hypoxic, however if this condition remained the wound will become chronic.

From day 4 to day 7, the area around the wound has relatively high oxygen saturation as the wound healing requires an adequate blood supply from the margin of the wound. When it came to day 10 until day 19, the scab fully formed and became thick where oxygen saturation had an unexpected low value under the scab. There is supposed to be tissue proliferation and vessel rebuild as we learnt in Section 1.2. However, the scab is thick with strong absorption that blocks the sine pattern from going underneath. The absorption map here is not capable of recovering the oxygen saturation there. From the area surrounding the wound, the temporary hypoxia happened again to stimulate the grow factor[188] as an initiator for the angiogenic and re-epidermisation. On day 14, as predicted by the μ_s' maps, the wound con-

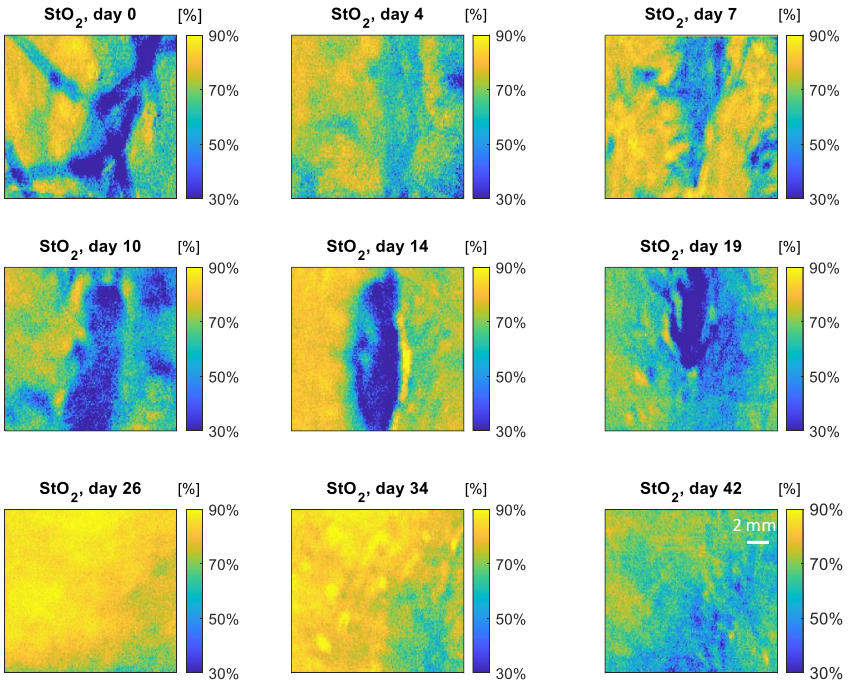

Figure 5.25: The oxygen saturation maps for the wound from day 0 to day 42.

traction is happening increase the demand on oxygen. Therefore, the oxygen level is high in the area surrounding the wound.

After the wound is visibly healed, turning into the last wound healing phase, the oxygen saturation is high observed in day 26 and day 34 when wound was in remodelling phase. At this time, the type 3 collagen was being replaced by type 1 which is dependent on the sufficient oxygen[188]. When the collagen replacement was done, the oxygen saturation decreased to the normal level.

5.5.3 Discussion

In this section, we report the first case study of using the SFDI method to observe surgical wound healing. This is a first, single case, but reveals the potential of applying SFDI method for wound imaging.

We find SFDI is capable of monitoring early infection signs, pus developing underneath, more timely and accurately than the naked eye. It is suggested that two

wavelengths should be used for obtaining the depth profile of pus. The structured change in the wound, i.e. the wound size and the collagen fibre change, can be present in the μ_s' maps. The μ_s' at both wavelengths is not influenced by the scab on the top of the wound area. However, the μ_s' is not sensitive to the inflammation in the wound site and the blood flow.

According to our modelling in Chapter 3, the larger difference between the μ_s' in the neighboring structures, the easier it is to detect the difference. This matches our observation that pus at day 0 demonstrates a good contrast with double the μ_s' value of the surrounding skin. Here the partial volume effect exists in that SFDI overestimates the wound width in a vertical structured wound. The wound area from the μ_s' map probably has a smaller size than indicated by lower μ_s' value, especially for the days 14 to 19. However, μ_s' here still presents the real size of the wound more accurately than the naked eye.

The μ_a map at 617 nm is a suitable tool to measure the blood supply change by measuring the chromophores: hemoglobin. Aided by the 850 nm wavelength illumination, we can calculate the StO_2 map to monitor the wound in another aspect. However, when the scab is fully formed, the μ_a and StO_2 measurement are limited in our case of study. As the scab thickness varies from skin condition and wound type, other surgical wounds might be feasible to be measured through the scab. Or one may consider using a longer wavelength to penetrate through the scab.

The uncertainty in the SFDI for wound healing should be noted. The curvature in the target area can distort the optical property recovery results. This has been report in other works[106, 67, 96]. The convex surface tends to have greater results while concave surface provides lower result in the optical properties.

5.6 Conclusion

In this Chapter, we explored the SFDI method for *in vivo* measurement for three clinical interesting skin complications include chronic eczema condition, acute skin irritation generated by SLS and biopsy wound healing. The first two skin complications have similar symptoms, i.e. epidermis damage and inflammation, which may occur in the wound healing process. They served as the preliminary studies for the wound healing monitoring.

Both SLS irritation and the eczema target areas suffered from the water loss and skin barrier damage. For the eczema imaging, SFDI system is able to distinguish the severe condition of the eczema condition with the epidermis damage by μ_s' histogram. The μ_a value may indicate the inflammation in the skin area by quantifying the hemoglobin content. For the SLS experiment, SFDI is able to aid in detecting the oxygen level change in the SLS experiment by measuring the μ_a. The μ_s' was found not sensitive to the inflammation in the skin.

However, the current SFDI system we used is not sufficient and sensitive enough for measuring and distinguish the details for these two skin conditions. We suggest the improvement in the SFDI system in the wavelength, e.g. 940 nm, for water content detection and combining the polarisation for the roughness assessment. Other optical techniques such as HSI and LDI could also be accompanied with the SFDI instrument.

To demonstrate the SFDI's potential, we conducted a pilot study using SFDI for monitoring *in vivo* surgical wound using the μ_s', μ_a and StO_2. The μ_s' is capable of monitoring the structure change for possible pus under the infection, re-epithelialization, and collagen fibre remodelling earlier than the naked eye. The μ_a calculation for the wound area is limited to the scab covering influencing the measurement of oxygen underneath. The scab is too thick here in the biopsy wound to obtain the oxygen level underneath. But the StO_2 values when the scab is thin or

lifted and around the wound area. Our results matches our biological knowledge of the wound healing.

In the three cases of study, we focused more on the relative change in the optical properties and the oxygen level. This is more of interests than the absolute value. Also, we find the structure curvature can introduce the uncertainty in the optical properties result as previous work[190]. One may consider a rough 3D shaped measurement combined with the SFDI measurement.

In summary, the SFDI method here demonstrates great potential for developing a optical technique aiding in the clinical skin monitoring. At the same time, one has to bear in mind that human tissue optical features vary from tissue position, person and time, even the same person. There is still a long way to go for SFDI to apply in the real life conditions.

Chapter 6

Conclusion and future work

Chapter 1 and Chapter 2

The first two chapters served as an comprehensive introduction for the reader in the SFDI field of skin imaging. In chapter 1, we reviewed the use of SFDI on skin related application and the wound healing knowledge. There have been several clinical cases successfully imaged utilising SFDI but the surgical wound has not been explored yet. We believe the SFDI has the potential for surgical wound imaging.

In the chapter 2, we reviewed the mathematical principles behind the conventional SFDI method. The step by step method using SFDI for measuring the reduced scattering and the absorption coefficient was introduced. The weakness and strength of the conventional SFDI method was discussed.

Chapter 3

In the Chapter 3, we proposed the vertical heterogeneous model for mimicking the surgical wound structure. The 3D Monte Carlo simulations provided numerical solutions to explore SFDI's lateral resolution on determining the wound structural change for the first time. With photon tracking in the Monte Carlo simulation, we were able to discover that the edge response is the key factor in wound width measurement. The wound width measurement accuracy is dependent on the spatial frequency, wound width and the wound reduced scattering coefficient. The 3D

Monte Carlo simulation here provided a flexible solution and customised design for photon propagation in the biological tissue.

Our numerical model for the photon tracking is feasible to apply for photon dynamic therapy (PDT)[191, 192]. We are looking to have a numerical model combining the time-solved drug diffusion and photon tracking to calculate the optimal laser power and the dose of the drug for better treatment. The absorption of each bin in the tissue model will have a dynamic change with each photon visitation. The photon bleaching efficiency will be calculated via the simulation. The biological model will be built with real biological data and typical drug parameters. The tissue model structure utilised in the simulation can be further detailed, subject to the real conditions.

Chapter 4

In the Chapter 4, we built up the SFDI system for phantom testing and human skin imaging. A resin phantom was made for validating the dependence of the wound width measurement error with spatial frequency, wound width and wound reduced scattering coefficient. However, the resin phantom is not always sufficient for testing the feasibility of current SFDI system for imaging the surgical wound. The animal model is a better option for preliminary experiments before imaging the *in vivo* human skin.

Due to the Covid-19 situation during the PhD, we didn't have a chance to conduct the animal experiments as we planned. The animal model is easier for us to control the parameters: the position of the wound, the type of bacteria causing the infection and the depth of the wound.

The rat will be an ideal animal for surgical wound healing imaging experiment[193] due to the physiological similarity to the human and wide availability. We will have two groups of the rats for the imaging experiment. One is the control group and the other is the infection group. The incision will be applied to the same position and depth to each rat. Referring to the previous work in burn wound infection[82],

one group of rats will be given an inoculation with a typical bacteria culture to create a infection. Then the wound infection and following wound recovery process will be measured and compared for two group using the SFDI instrument.

Chapter 5

In the Chapter 5, we conducted three clinical interest human skin imaging experiments. We found that SFDI has great potential for detecting the structural change in the epidermis and collagen fibres. Absorption is a promising indicator for the oxygen level and total hemoglobin concentration. The instrument itself needs an improvement along with the SFDI method in two main aspects.

One is to upgrade the current SFDI system with polarisation[86, 87], and adding further IR wavelength[182] illumination to the optical path to measure lipids and water content.

The other aspect is combining other optical imaging techniques including hyperspectral imaging (HSI) and the Laser Doppler imaging (LDI). HSI has been reported as measuring the water content in a dynamic way[194, 78, 195]. This will aid in measuring the water loss in eczema and the SLS experiment. The LDI is for measuring the blood flow change within the target area[196, 197].

In terms of a weakness we observed from the three *in vivo* experiments, we may consider measuring and calibrating the curvature of the target area in advance to eliminate this measurement error.

Outlook

In this thesis, we built up both numerical models and an SFDI instrument for wound healing monitoring applications. It is worth noting that there has been a commercial SFDI research platform (Reflect RS^{TM}) from the Modulim company[5] integrating the acquisition, processing and the visualisation functions. The system is composed of a DMD, a single-monochrome camera and 9 wavelengths of LEDs from the VIS to the NIR region. However, the biological tissue is always complex and different clinical conditions require specific design of the instrument. There is

still a great number of topics in the diffuse imaging field waiting to explore to fill in the gap between laboratory experiment and clinical applications.

We will look for suitable surgical wound under our biological tissue license and collaborating with the clinicians. Here we only have two specific clinical skin cases which are not adequate for us to provide a systematic report on SFDI for surgical wound imaging. For example, we are also interested in the abdominal surgery's open wound which have the incidence of infection at 35%. The abdominal area of the skin is relatively flat in the shape. Also we are interested in utilising SFDI as an non-contact method for assessing the neonatal intubation to aid with the infant treatment.

Bibliography

[1] Anatomy of the Skin, 2019. URL https://www.stanfordchildrens.org/en/topic/default?id=anatomy-of-the-skin-85-P01336.

[2] Sabine A. Eming, Paul Martin, and Marjana Tomic-Canic. Wound repair and regeneration: Mechanisms, signaling, and translation. *Science Translational Medicine*, 6(265), 2014. doi: 10.1126/scitranslmed.3009337.

[3] What is wound healing?, 2019. URL https://synergapharma.eu/en/dermatology/wounds-stratamed-alkaderma/.

[4] Yuji Shirakata, Rina Kimura, Daisuke Nanba, Ryo Iwamoto, Sho Tokumaru, Chie Morimoto, Koichi Yokota, Masanori Nakamura, Koji Sayama, Eisuke Mekada, Shigeki Higashiyama, and Koji Hashimoto. Heparin-binding EGF-like growth factor accelerates keratinocyte migration and skin wound healing. *Journal of Cell Science*, 118(11):2363–2370, 2005. doi: 10.1242/jcs.02346.

[5] Sylvain Gioux; Amaan Mazhar ;David J. Cuccia. Spatial frequency domain imaging in 2019: principles, applications, and perspectives. *Journal of Biomedical Optics*, 18(3):035001–7, 2019. doi: 10.1117/1.

[6] David J. Cuccia, Frederic Bevilacqua, Anthony J. Durkin, Frederick R. Ayers, and Bruce J. Tromberg. Quantitation and mapping of tissue optical proper-

ties using modulated imaging. *Journal of Biomedical Optics*, 14(2):024012, 2009. doi: 10.1117/1.3088140.

[7] JM Schmitt. Optical measurement of blood oxygenation by implantable telemetry. *Technical Report G558-15*, 1986.

[8] Mahmood Kamali Moaveni. *A multiple scattering field theory applied to whole blood*. University of Washington, 1970.

[9] Scott Prahl. Tabulated molar extinction coefficient for hemoglobin in water. URL `https://omlc.org/spectra/hemoglobin/summary.html`.

[10] Dmitry Yudovsky and Laurent Pilon. Rapid and accurate estimation of blood saturation, melanin content, and epidermis thickness from spectral diffuse reflectance. *Applied Optics*, 49(10):1707–1719, 2010. doi: 10.1364/AO.49.001707.

[11] R. L.P. van Veen, H. J.C.M. Sterenborg, A. Pifferi, A. Torricelli, and R. Cubeddu. Determination of VIS- NIR absorption coefficients of mammalian fat, with time- and spatially resolved diffuse reflectance and transmission spectroscopy. *Optics InfoBase Conference Papers*, pages 1–3, 2004. doi: 10.1364/bio.2004.sf4.

[12] Kent F. Palmer and Dudley Williams. Optical properties of water in the near infrared*. *Journal of the Optical Society of America*, 64(8):1107, 1974. doi: 10.1364/josa.64.001107.

[13] Seraphin A. Sullivan. Experimental study of the absorption in distilled water, artificial sea water, and heavy water in the visible region of the spectrum*. *Journal of the Optical Society of America*, 53(8):962, 1963. doi: 10.1364/josa.53.000962.

[14] Alistair D. Bounds and John M. Girkin. Early stage dental caries detection using near infrared spatial frequency domain imaging. *Scientific Reports*, 11 (1):3–11, 2021. doi: 10.1038/s41598-021-81872-7.

[15] Caetano P. Sabino, Alessandro M. Deana, Tania M. Yoshimura, Daniela F.T. da Silva, Cristiane M França, Michael R Hamblin, and Martha S Ribeiro. The optical properties of mouse skin in the visible and near infrared spectral regions. *Journal of Photochemistry and Photobiology B: Biology*, 160:72–78, 7 2016. doi: 10.1016/j.jphotobiol.2016.03.047.

[16] Z.-X. Jiang and J. DeLaCruz. Appearance benefits of skin moisturization. *Skin Research and Technology*, 17(1):51–55, feb 2011.

[17] Joshua Phillip Totty, Joe William Edward Moss, Erin Barker, Stuart James Mealing, John William Posnett, Ian Clifford Chetter, and George Edward Smith. The impact of surgical site infection on hospitalisation, treatment costs, and health-related quality of life after vascular surgery. *International Wound Journal*, 18(3):261–268, 2021. doi: 10.1111/iwj.13526.

[18] David J Leaper, Harry van Goor, Jacqueline Reilly, Nicola Petrosillo, Heinrich K Geiss, Antonio J Torres, and Anne Berger. Surgical site infection - a European perspective of incidence and economic burden. *International Wound Journal*, 1(4):247–273, 12 2004. doi: 10.1111/j.1742-4801.2004.00067.x.

[19] Julian F. Guest, Graham W. Fuller, and Peter Vowden. Cohort study evaluating the burden of wounds to the UK's National Health Service in 2017/2018: Update from 2012/2013. *BMJ Open*, 10(12):1–15, 2020. doi: 10.1136/bmjopen-2020-045253.

[20] Wilfredo Lopez-ojeda, Amarendra Pandey, Mandy Alhajj, and Amanda M Oakley. Anatomy , skin (integument), 2022. URL `https://ncbi.nlm.nih.gov/books/NBK441980/#:~:text=Theepidermisisfurtherdivided,%2Clackingthestratumlucidum)`.

[21] Elli Angelopoulou. The Reflectance Spectrum of Human Skin. *(Technical Report MS-CIS-99-29)*, (December):1–14, 1999.

[22] Paul A. J. Kolarsick, Maria Ann Kolarsick, and Carolyn Goodwin. Anatomy and Physiology of the Skin. *Journal of the Dermatology Nurses' Association*, 3(4):203–213, 7 2011. doi: 10.1097/JDN.0b013e3182274a98.

[23] Thomas M Brown and Karthik Krishnamurthy. Histology , Dermis Histochemistry and Cytochemistry, 2022. URL `https://www.ncbi.nlm.nih.gov/books/NBK535346/`.

[24] Tom Lister, Philip A. Wright, and Paul H. Chappell. Optical properties of human skin. *Journal of Biomedical Optics*, 17(9):0909011, 2012. doi: 10.1117/1.jbo.17.9.090901.

[25] Carla Stecco, Warren Hammer, Andry Vleeming, and Raffaele De Caro. *Subcutaneous Tissue and Superficial Fascia*. Elsevier, 2015. doi: 10.1016/B978-0-7020-4430-4.00002-6.

[26] Tomaz Velnar, T. Bailey, and V. Smrkolj. The wound healing process: An overview of the cellular and molecular mechanisms. *Journal of International Medical Research*, 37(5):1528–1542, 2009. doi: 10.1177/147323000903700531.

[27] Gregory S Schultz, Gloria A Chin, and Robert F Diegelmann. Principles of Wound Healing, 2011. URL `https://www.ncbi.nlm.nih.gov/books/NBK534261/`.

[28] Sabine A. Eming, Thomas Krieg, and Jeffrey M. Davidson. Inflammation in wound repair: Molecular and cellular mechanisms. *Journal of Investigative Dermatology*, 127(3):514–525, 2007. doi: 10.1038/sj.jid.5700701.

[29] Shomita S. Mathew-Steiner, Sashwati Roy, and Chandan K. Sen. Collagen in wound healing. *Bioengineering*, 8(5), 2021. doi: 10.3390/bioengineering8050063.

[30] Matthew H Kanzler, David C Gorsulowsky, and Neil a Swanson. Basic Mechanisms in the Healing. *The Journal of dermatologic surgery and oncology*, 12 (11):1156–1164, 1986.

[31] Heather A. Wallace and Patrick M. Zito. Wound Healing Phases, 2019. URL http://www.ncbi.nlm.nih.gov/pubmed/29262065.

[32] Ning Xu Landén, Dongqing Li, and Mona Ståhle. Transition from inflammation to proliferation: a critical step during wound healing. *Cellular and Molecular Life Sciences*, 73(20):3861–3885, 2016. doi: 10.1007/s00018-016-2268-0.

[33] Omar Skalli; Giulio Gabbiani. *The Biology of the Myofibroblast Relationship to Wound Contraction and Fibrocontractive Diseases*, volume 69. 8 1998.

[34] R. A.F. Clark. Regulation of fibroplasia in cutaneous wound repair. *American Journal of the Medical Sciences*, 306(1):42–48, 1993. doi: 10.1097/00000441-199307000-00011.

[35] Surgical wounds and preventing infections. URL https://www.guysandstthomas.nhs.uk/health-information/surgical-wounds-and-preventing-infections#:~:text=Most%20surgical%20wound%20infections%20are,from%20different%20types%20of%20germs.

[36] Caring for your surgical wound information leaflet. URL https://www.liverpoolwomens.nhs.uk/media/3524/caring-for-your-surgical-wound-information-leaflet.pdf.

[37] C. D. Owens and K. Stoessel. Surgical site infections: epidemiology, microbiology and prevention. *Journal of Hospital Infection*, 70(SUPPL. 2):3–10, 2008. doi: 10.1016/S0195-6701(08)60017-1.

[38] Matthew Wynn. The impact of infection on the four stages of acute wound healing: An overview. *Wounds UK*, 17(2):26–32, 2021.

[39] Emily S. Petherick, Jane E. Dalton, Peter J. Moore, and Nicky Cullum. Methods for identifying surgical wound infection after discharge from hos-

pital: A systematic review. *BMC Infectious Diseases*, 6, 2006. doi: 10.1186/1471-2334-6-170.

[40] Shuxin Li, Paul Renick, Jon Senkowsky, Ashwin Nair, and Liping Tang. Diagnostics for Wound Infections. *Advances in Wound Care*, 10(6):317–327, 2021. doi: 10.1089/wound.2019.1103.

[41] K.F. Cutting and K.G. Harding. Criteria for identifying wound infection. *Journal of Wound Care*, 3(4):198–201, 1994. doi: 10.12968/jowc.1994.3.4.198.

[42] Keith F Cutting and Richard White. Defined and refined: criteria for identifying wound infection revisited. *British Journal of Community Nursing*, 9 (Sup1):S6–S15, 3 2004. doi: 10.12968/bjcn.2004.9.Sup1.12495.

[43] Maria Elisa Smith, Natanya Robinowitz, Patrick Chaulk, and Kristine Johnson. Comparison of chronic wound culture techniques: Swab versus curetted tissue for microbial recovery. *British Journal of Community Nursing*, 19(9 0):S22–S26, 2014. doi: 10.12968/bjcn.2014.19.Sup9.S22.

[44] Phyllis A. Bonham. Swab cultures for diagnosing wound infections: A literature review and clinical guideline. *Journal of Wound, Ostomy and Continence Nursing*, 36(4):389–395, 7 2009. doi: 10.1097/WON.0B013E3181AAEF7F.

[45] Elizabeth Jane Gothard. *Wound healing, a multidisciplinary approach: combining mathematical models and biological experiments.* PhD thesis, University of York, 2016.

[46] Maanasa Jayachandran, Suset Rodriguez, Elizabeth Solis, Jiali Lei, and Anuradha Godavarty. Critical Review of Noninvasive Optical Technologies for Wound Imaging. *Advances in Wound Care*, 5(8):349–359, 2016. doi: 10.1089/wound.2015.0678.

[47] David Huang, Eric A Swanson, Charles P Lin, Joel S Schuman, William G Stinson, Warren Chang, Michael R Hee, Thomas Flotte, Kenton Gregory,

Carmen A Puliafito, et al. Optical coherence tomography. *science*, 254(5035): 1178–1181, 1991.

[48] Piotr Targowski, Maciej Wojtkowski, Andrzej Kowalczyk, Tomasz Bajraszewski, Maciej Szkulmowski, and Iwona Gorczyńska. Complex spectral oct in human eye imaging in vivo. *Optics Communications*, 229(1-6): 79–84, 2004.

[49] Michael Pircher, Christoph K Hitzenberger, and Ursula Schmidt-Erfurth. Polarization sensitive optical coherence tomography in the human eye. *Progress in retinal and eye research*, 30(6):431–451, 2011.

[50] Mark C Pierce, Robert L Sheridan, B Hyle Park, Barry Cense, and Johannes F De Boer. Collagen denaturation can be quantified in burned human skin using polarization-sensitive optical coherence tomography. *Burns*, 30(6): 511–517, 2004.

[51] Kwan S. Park, Woo June Choi, Shaozhen Song, Jingjiang Xu, and Ruikang K. Wang. Multifunctional in vivo imaging for monitoring wound healing using swept-source polarization-sensitive optical coherence tomography. *Lasers in Surgery and Medicine*, 50(3):213–221, 2018. doi: 10.1002/lsm.22767.

[52] Adam J Singer, Zhenguo Wang, Steve A McClain, and Yingtian Pan. Optical coherence tomography: a noninvasive method to assess wound reepithelialization. *Academic Emergency Medicine*, 14(5):387–391, 2007.

[53] Michael J Cobb, Yuchuan Chen, Robert A Underwood, Marcia L Usui, John Olerud, and Xingde Li. Noninvasive assessment of cutaneous wound healing using ultrahigh-resolution optical coherence tomography. *Journal of biomedical optics*, 11(6):064002–064002, 2006.

[54] Shyam M Srinivas, Johannes F de Boer, Hyle Park, Kourosh Keikhanzadeh, Huai-en L Huang, Jun Zhang, Woong Qyu Jung, Zhongping Chen, and J Stu-

art Nelson. Determination of burn depth by polarization-sensitive optical coherence tomography. *Journal of biomedical optics*, 9(1):207–212, 2004.

[55] Paul Beard. Biomedical photoacoustic imaging. *Interface focus*, 1(4):602–631, 2011.

[56] Xosé Luís Deán-Ben and Daniel Razansky. Optoacoustic imaging of the skin. *Experimental Dermatology*, 30(11):1598–1609, nov 2021. doi: 10.1111/exd.14386.

[57] Murad Omar, Mathias Schwarz, Dominik Soliman, Panagiotis Symvoulidis, and Vasilis Ntziachristos. Pushing the optical imaging limits of cancer with multi-frequency-band raster-scan optoacoustic mesoscopy (rsom). *Neoplasia*, 17(2):208–214, 2015.

[58] Avihai Ron, Xosé Luís Deán-Ben, Sven Gottschalk, and Daniel Razansky. Volumetric optoacoustic imaging unveils high-resolution patterns of acute and cyclic hypoxia in a murine model of breast cancer. *Cancer research*, 79 (18):4767–4775, 2019.

[59] Zhongwen Cheng, Haigang Ma, Zhiyang Wang, and Sihua Yang. In vivo volumetric monitoring of revascularization of traumatized skin using extended depth-of-field photoacoustic microscopy. *Frontiers of Optoelectronics*, 13: 307–317, 2020.

[60] Yasuyuki Tsunoi, Shunichi Sato, Satoko Kawauchi, Hiroshi Ashida, Daizoh Saitoh, and Mitsuhiro Terakawa. In vivo photoacoustic molecular imaging of the distribution of serum albumin in rat burned skin. *Burns*, 39(7):1403–1408, 2013.

[61] Hao F Zhang, Konstantin Maslov, George Stoica, and Lihong V Wang. Imaging acute thermal burns by photoacoustic microscopy. *Journal of biomedical optics*, 11(5):054033–054033, 2006.

[62] Laetitia Vionnet, Jerome Gateau, Mathias Schwarz, Andreas Buehler, Volodymir Ermolayev, and Vasilis Ntziachristos. 24-mhz scanner for optoacoustic imaging of skin and burn. *IEEE transactions on medical imaging*, 33(2): 535–545, 2013.

[63] Ali Hariri, Fang Chen, Colman Moore, and Jesse V Jokerst. Noninvasive staging of pressure ulcers using photoacoustic imaging. *Wound Repair and Regeneration*, 27(5):488–496, 2019.

[64] Tamar Harary, Michael Nagli, Nathan Suleymanov, Ilya Goykhman, and Amir Rosenthal. Large-field-of-view optical-resolution optoacoustic microscopy using a stationary silicon-photonics acoustic detector. *Journal of Biomedical Optics*, 29(S1):1–11, 2024. doi: 10.1117/1.jbo.29.s1.s11511.

[65] David J. Cuccia, Frederic Bevilacqua, Anthony J. Durkin, and Bruce J. Tromberg. Modulated imaging: quantitative analysis and tomography of turbid media in the spatial-frequency domain. *Optics Letters*, 30(11):1354, 2005. doi: 10.1364/ol.30.001354.

[66] Craig Weinkauf, Amaan Mazhar, Kairavi Vaishnav, Auon A. Hamadani, David J. Cuccia, and David G. Armstrong. Near-instant noninvasive optical imaging of tissue perfusion for vascular assessment. *Journal of Vascular Surgery*, 69(2):555–562, 2019. doi: 10.1016/j.jvs.2018.06.202.

[67] Amr Yafi, Fuad K. Muakkassa, Tejasvi Pasupneti, Judy Fulton, David J. Cuccia, Amaan Mazhar, Kimberly N. Blasiole, and Eliot N. Mostow. Quantitative skin assessment using spatial frequency domain imaging (SFDI) in patients with or at high risk for pressure ulcers. *Lasers in Surgery and Medicine*, 49(9):827–834, 2017. doi: 10.1002/lsm.22692.

[68] Anahita Pilvar, Aarohi M. Mehendale, Kavon Karrobi, Fatima El-Adili, Andreea Bujor, and Darren Roblyer. Spatial frequency domain imaging for the

assessment of scleroderma skin involvement. *Biomedical Optics Express*, 14 (6):2955, 2023. doi: 10.1364/boe.489609.

[69] Amaan Mazhar, Steve Saggese, Alonda C. Pollins, Nancy L. Cardwell, Lillian Nanney, and David J. Cuccia. Noncontact imaging of burn depth and extent in a porcine model using spatial frequency domain imaging. *Journal of Biomedical Optics*, 19(8):086019, 8 2014. doi: 10.1117/1.JBO.19.8.086019.

[70] John Quan Nguyen, Christian Crouzet, Tuan Mai, Kathleen Riola, Daniel Uchitel, Lih-Huei Liaw, Nicole Bernal, Adrien Ponticorvo, Bernard Choi, and Anthony J. Durkin. Spatial frequency domain imaging of burn wounds in a preclinical model of graded burn severity. *Journal of Biomedical Optics*, 18(6):066010, 2013. doi: 10.1117/1.jbo.18.6.066010.

[71] Matthew B. Applegate, Kavon Karrobi, Joseph P. Angelo, Wyatt M. Austin, Syeda M. Tabassum, Enagnon Aguénounon, Karissa Tilbury, Rolf B. Saager, Sylvain Gioux, and Darren M. Roblyer. OpenSFDI: an open-source guide for constructing a spatial frequency domain imaging system. *Journal of Biomedical Optics*, 25(01):1, 2020. doi: 10.1117/1.jbo.25.1.016002.

[72] M. D. STERN. In vivo evaluation of microcirculation by coherent light scattering. *Nature*, 254:56–58, 3 1975. ISSN 0028-0836. doi: 10.1038/254056a0.

[73] T.J.H. Essex and P.O. Byrne. A laser doppler scanner for imaging blood flow in skin. *Journal of Biomedical Engineering*, 13(3):189–194, 1991. ISSN 0141-5425. doi: https://doi.org/10.1016/0141-5425(91)90125-Q.

[74] Henk Hoeksema, Karlien Van de Sijpe, Thiery Tondu, Moustapha Hamdi, Koenraad Van Landuyt, Phillip Blondeel, and Stan Monstrey. Accuracy of early burn depth assessment by laser doppler imaging on different days post burn. *Burns*, 35(1):36–45, 2009.

[75] AJA Holland, HCO Martin, and DT Cass. Laser doppler imaging prediction of burn wound outcome in children. *Burns*, 28(1):11–17, 2002.

[76] Georgios N Stamatas, Costas J Balas, and Nikiforos Kollias. Hyperspectral image acquisition and analysis of skin. In *Spectral Imaging: Instrumentation, Applications, and Analysis II*, volume 4959, pages 77–82. SPIE, 2003.

[77] David T Dicker, Jeremy Lerner, Pat Van Belle, DuPont Guerry, 4th, Meenhard Herlyn, David E Elder, and Wafik S El-Deiry. Differentiation of normal skin and melanoma using high resolution hyperspectral imaging. *Cancer biology & therapy*, 5(8):1033–1038, 2006.

[78] Maximilian Dietrich, Sebastian Marx, Maik von der Forst, Thomas Bruckner, Felix CF Schmitt, Mascha O Fiedler, Felix Nickel, Alexander Studier-Fischer, Beat P Müller-Stich, Thilo Hackert, et al. Hyperspectral imaging for perioperative monitoring of microcirculatory tissue oxygenation and tissue water content in pancreatic surgery—an observational clinical pilot study. *Perioperative Medicine*, 10(1):1–12, 2021.

[79] Shicheng Hao, Ying Xiong, Sisi Guo, Jing Gao, Xiaotong Chen, Ruoyu Zhang, Lihui Liu, and Jianfeng Wang. Development and performance validation of a low-cost algorithms-based hyperspectral imaging system for radiodermatitis assessment. *Biomedical Optics Express*, 14(9):4990, 2023. doi: 10.1364/boe.500067.

[80] Feng Gao, Qun Wang, Junyu Dong, and Qizhi Xu. Spectral and spatial classification of hyperspectral images based on random multi-graphs. *Remote Sensing*, 10(8):1–20, 2018. doi: 10.3390/rs10081271.

[81] Wenjing Lv and Xiaofei Wang. Overview of Hyperspectral Image Classification. *Journal of Sensors*, 2020, 2020. doi: 10.1155/2020/4817234.

[82] Thu T.A. Nguyen, Jessica C. Ramella-Roman, Lauren T. Moffatt, Rachel T. Ortiz, Marion H. Jordan, and Jeffrey W. Shupp. Novel application of a spatial frequency domain imaging system to determine signature spectral differences

between infected and noninfected burn wounds. *Journal of Burn Care and Research*, 34(1):44–50, 2013. doi: 10.1097/BCR.0b013e318269be30.

[83] Rolf B. Saager, Rebecca A. Rowland, Melissa L. Baldado, Gordon T. Kennedy, Nicole P. Bernal, Adrien Ponticorvo, Robert J. Christy, and Anthony J. Durkin. Impact of hemoglobin breakdown products in the spectral analysis of burn wounds using spatial frequency domain spectroscopy. *Journal of Biomedical Optics*, 24(02), 2019. doi: 10.1117/1.jbo.24.2.020501.

[84] R. B. Saager, D. J. Cuccia, S. Saggese, K. M. Kelly, and A. J. Durkin. A Light Emitting Diode (LED) Based Spatial Frequency Domain Imaging System for Optimization of Photodynamic Therapy of Nonmelanoma Skin Cancer: Quantitative Reflectance Imaging. *Lasers in Surgery and Medicine*, 45(4):207–215, 4 2013. doi: 10.1002/lsm.22139.

[85] Ashley M. Laughney, Venkataramanan Krishnaswamy, Elizabeth J. Rizzo, Mary C. Schwab, Richard J. Barth J, David J. Cuccia, Bruce J. Tromberg, Keith D. Paulsen, Brian W. Pogue, and Wendy A. Wells. Spectral discrimination of breast pathologies in situ using spatial frequency domain imaging. *Breast Cancer Research*, 15(4), 2013. doi: 10.1186/bcr3455.

[86] Pejhman Ghassemi, Jeffrey W. Shupp, Lauren T. Moffatt, and Jessica C. Ramella-Roman. A novel spectral imaging system for quantitative analysis of hypertrophic scar. *Photonic Therapeutics and Diagnostics IX*, 8565(March 2013):85650U, 2013. doi: 10.1117/12.2006096.

[87] Pejhman Ghassemi, Taryn E. Travis, Lauren T. Moffatt, Jeffrey W. Shupp, and Jessica C. Ramella-Roman. A polarized multispectral imaging system for quantitative assessment of hypertrophic scars. *Biomedical Optics Express*, 5(10):3337, 2014. doi: 10.1364/boe.5.003337.

[88] Bin Yang, John Lesicko, Manu Sharma, Michael Hill, Michael S. Sacks, and James W. Tunnell. Polarized light spatial frequency domain imaging for non-

destructive quantification of soft tissue fibrous structures. *Biomedical Optics Express*, 6(4):1520, 2015. doi: 10.1364/boe.6.001520.

[89] Jessie R. Weber, David J. Cuccia, and Bruce J. Tromberg. Modulated imaging in layered media. *Annual International Conference of the IEEE Engineering in Medicine and Biology - Proceedings*, pages 6674–6676, 2006. doi: 10.1109/IEMBS.2006.260918.

[90] Jessie R. Weber, David J. Cuccia, Anthony J. Durkin, and Bruce J. Tromberg. Noncontact imaging of absorption and scattering in layered tissue using spatially modulated structured light. *Journal of Applied Physics*, 105 (10), 2009. doi: 10.1063/1.3116135.

[91] Sean T. Horan, Adam R. Gardner, Rolf Saager, Anthony J. Durkin, and Vasan Venugopalan. Recovery of layered tissue optical properties from spatial frequency-domain spectroscopy and a deterministic radiative transport solver. *Journal of Biomedical Optics*, 24(07):1, 11 2019. doi: 10.1117/1.JBO.24.7.071607.

[92] Anouk L. Post, Dirk J. Faber, and Ton G. van Leeuwen. Model for the diffuse reflectance in spatial frequency domain imaging. *Journal of Biomedical Optics*, 28(04):024012, 4 2023. doi: 10.1117/1.JBO.28.4.046002.

[93] Carole K. Hayakawa, Kavon Karrobi, Vivian Pera, Darren Roblyer, and Vasan Venugopalan. Optical sampling depth in the spatial frequency domain. *Journal of Biomedical Optics*, 24(07):1, 2018. doi: 10.1117/1.jbo.24.7.071603.

[94] Dmitry Yudovsky, John Quan M. Nguyen, and Anthony J. Durkin. In vivo spatial frequency domain spectroscopy of two layer media . *Journal of Biomedical Optics*, 17(10):107006, 2012. doi: 10.1117/1.jbo.17.10.107006.

[95] Vivian Pera, Kavon Karrobi, Syeda Tabassum, Fei Teng, and Darren Roblyer. Optical property uncertainty estimates for spatial frequency domain imaging. *Biomedical Optics Express*, 9(2):661, 2018. doi: 10.1364/boe.9.000661.

[96] Syeda Tabassum, Yanyu Zhao, Raeef Istfan, Junjie Wu, David J. Waxman, and Darren Roblyer. Feasibility of spatial frequency domain imaging (SFDI) for optically characterizing a preclinical oncology model. *Biomedical Optics Express*, 7(10):4154, 10 2016. doi: 10.1364/BOE.7.004154.

[97] Nico Bodenschatz, Arnd Brandes, André Liemert, and Alwin Kienle. Sources of errors in spatial frequency domain imaging of scattering media. *Journal of Biomedical Optics*, 19(7):071405, 2014. doi: 10.1117/1.jbo.19.7.071405.

[98] Tim A. Erickson, Amaan Mazhar, David Cuccia, Anthony J. Durkin, and James W. Tunnell. Lookup-table method for imaging optical properties with structured illumination beyond the diffusion theory regime. *Journal of Biomedical Optics*, 15(3):036013, 2010. doi: 10.1117/1.3431728.

[99] Ashley M. Laughney, Venkataramanan Krishnaswamy, Tyler B. Rice, David J. Cuccia, Richard J. Barth, Bruce J. Tromberg, Keith D. Paulsen, Brian W. Pogue, and Wendy A. Wells. System analysis of spatial frequency domain imaging for quantitative mapping of surgically resected breast tissues. *Journal of Biomedical Optics*, 18(3):036012, 2013. doi: 10.1117/1.jbo.18.3.036012.

[100] Dennis Wirth, Mira Sibai, Jonathan Olson, Brian C. Wilson, David W. Roberts, and Keith Paulsen. Feasibility of using spatial frequency-domain imaging intraoperatively during tumor resection. *Journal of Biomedical Optics*, 24(07):1, 2018. doi: 10.1117/1.jbo.24.7.071608.

[101] Marine Soret, Stephen L. Bacharach, and Irène Buvat. Partial-Volume Effect in PET Tumor Imaging. *Journal of Nuclear Medicine*, 48(6):932–945, 6 2007. doi: 10.2967/jnumed.106.035774.

[102] Peter Santago and H. Donald Gage. Statistical Models of Partial Volume Effect. *IEEE Transactions on Image Processing*, 4(11):1531–1540, 1995. doi: 10.1109/83.469934.

[103] Miguel Ángel González Ballester, Andrew P. Zisserman, and Michael Brady. Estimation of the partial volume effect in MRI. *Medical Image Analysis*, 6 (4):389–405, 2002. doi: 10.1016/S1361-8415(02)00061-0.

[104] Mohammad Torabzadeh, Patrick A. Stockton, Gordon T. Kennedy, Rolf B. Saager, Anthony J. Durkin, Randy A. Bartels, and Bruce J. Tromberg. Hyperspectral imaging in the spatial frequency domain with a supercontinuum source. *Journal of Biomedical Optics*, 24(07):1, 2019. doi: 10.1117/1.jbo.24.7.071614.

[105] Soren D. Konecky, Chris M. Owen, Tyler Rice, Pablo A. Valdés, Kolbein Kolste, Brian C. Wilson, Frederic Leblond, David W. Roberts, Keith D. Paulsen, and Bruce J. Tromberg. Spatial frequency domain tomography of protoporphyrin IX fluorescence in preclinical glioma models. *Journal of Biomedical Optics*, 17(5):056008, 2012. doi: 10.1117/1.jbo.17.5.056008.

[106] Jingxuan Ren, Gabriel A. Ramirez, Ashley R. Proctor, Tong Tong Wu, Danielle S. W. Benoit, and Regine Choe. Spatial frequency domain imaging for the longitudinal monitoring of vascularization during mouse femoral graft healing. *Biomedical Optics Express*, 11(10):5442, 2020. doi: 10.1364/boe.401472.

[107] D. F. Swinehart. The Beer-Lambert law. *Journal of Chemical Education*, 39 (7):333–335, 1962. doi: 10.1021/ed039p333.

[108] Bruce Hapke. Theory of Reflectance and Emittance Spectroscopy. *Theory of Reflectance and Emittance Spectroscopy, Second Edition*, 9780521883:1–513, 1 2012. doi: 10.1017/CBO9781139025683.

[109] Steven L. Jacques. Erratum: Optical properties of biological tissues: A review (Physics in Medicine and Biology (2013) 58). *Physics in Medicine and Biology*, 58(14):5007–5008, 2013. doi: 10.1088/0031-9155/58/14/5007.

[110] George Zonios, Aikaterini Dimou, Ioannis Bassukas, Dimitrios Galaris, Argyrios Tsolakidis, and Efthimios Kaxiras. Melanin absorption spectro-

scopy: new method for noninvasive skin investigation and melanoma detection. *Journal of Biomedical Optics*, 13(1):014017, 2008. doi: 10.1117/1.2844710.

[111] Simon Alaluf, Derek Atkins, Karen Barrett, Margaret Blount, Nik Carter, and Alan Heath. Ethnic variation in melanin content and composition in photoexposed and photoprotected human skin. *Pigment Cell Research*, 15 (2):112–118, 2002.

[112] Michaela Taylor-Williams, Graham Spicer, Gemma Bale, and Sarah E. Bohndiek. Noninvasive hemoglobin sensing and imaging: optical tools for disease diagnosis. *Journal of Biomedical Optics*, 27(08), 2022. doi: 10.1117/1.jbo.27.8.080901.

[113] J. A. McGrath, R. A. J. Eady, and F. M. Pope. *Anatomy and Organization of Human Skin*, chapter 3, pages 45–128. John Wiley Sons, Ltd, 2004. ISBN 9780470750520. doi: https://doi.org/10.1002/9780470750520.ch3.

[114] Yu Shimojo, Takahiro Nishimura, Hisanao Hazama, Toshiyuki Ozawa, and Kunio Awazu. Measurement of absorption and reduced scattering coefficients in Asian human epidermis, dermis, and subcutaneous fat tissues in the 400- to 1100-nm wavelength range for optical penetration depth and energy deposition analysis. *Journal of Biomedical Optics*, 25(04):1, 2020. doi: 10.1117/1.jbo.25.4.045002.

[115] Huafeng Ding, Jun Q. Lu, William A. Wooden, Peter J. Kragel, and Xin Hua Hu. Refractive indices of human skin tissues at eight wavelengths and estimated dispersion relations between 300 and 1600 nm. *Physics in Medicine and Biology*, 51(6):1479–1489, 2006. doi: 10.1088/0031-9155/51/6/008.

[116] Daichi Fukutomi, Katsunori Ishii, and Kunio Awazu. Determination of the scattering coefficient of biological tissue considering the wavelength and ab-

sorption dependence of the anisotropy factor. *Optical Review*, 23(2):291–298, 2016. doi: 10.1007/s10043-015-0161-y.

[117] T. Durduran, R. Choe, W. B. Baker, and A. G. Yodh. Diffuse optics for tissue monitoring and tomography. *Reports on Progress in Physics*, 73(7), 2010. doi: 10.1088/0034-4885/73/7/076701.

[118] Lars O. Svaasand, Thorsten Spott, Joshua B. Fishkin, Tuan Pham, Bruce J. Tromberg, and Michael W. Berns. Reflectance measurements of layered media with diffuse photon-density waves: A potential tool for evaluating deep burns and subcutaneous lesions. *Physics in Medicine and Biology*, 44(3):801–813, 1999. doi: 10.1088/0031-9155/44/3/020.

[119] Richard C. Haskell, Lars O. Svaasand, Tsong-Tseh Tsay, Ti-Chen Feng, Bruce J. Tromberg, Matthew S. McAdams, Lars O. Svaasand, Bruce J. Tromberg, Richard C. Haskell, Matthew S. McAdams, and Ti-Chen Feng. Boundary conditions for the diffusion equation in radiative transfer. *Journal of the Optical Society of America A*, 11(10):2727, 10 1994. doi: 10.1364/josaa.11.002727.

[120] Lihong V. Wang, Steven L. Jacques, and Liqiong Zheng. MCML-Monte Carlo modeling of light transport in multi-layered tissues. *Computer Methods and Programs in Biomedicine*, 47(2):131–146, 1995. doi: 10.1016/0169-2607(95)01640-F.

[121] Ben O.L. Mellors and Hamid Dehghani. A pixel-dependent finite element model for spatial frequency domain imaging using nirfast. *Photonics*, 8(8), 2021. doi: 10.3390/photonics8080310.

[122] Hamid Dehghani, Subhadra Srinivasan, Brian W Pogue, and Adam Gibson. Numerical modelling and image reconstruction in diffuse optical tomography. *Philosophical Transactions of the Royal Society A: Mathematical, Physical and Engineering Sciences*, 367(1900):3073–3093, 2009.

[123] B. C. Wilson and G. Adam. A Monte Carlo model for the absorption and flux distributions of light in tissue. *Medical Physics*, 10(6):824–830, 11 1983. doi: 10.1118/1.595361.

[124] Yoshihisa Aizu, Takaaki Maeda, Tomohiro Kuwahara, and Tetsuji Hirao. Spectral reflectance fitting based on Monte Carlo simulation using a multi-layered skin tissue model. *Optics InfoBase Conference Papers*, 17(3):223–229, 2011. doi: 10.1117/12.889626.

[125] Michele Martinelli, Adam Gardner, David Cuccia, Carole Hayakawa, Jerome Spanier, and Vasan Venugopalan. Analysis of single Monte Carlo methods for prediction of reflectance from turbid media. *Optics Express*, 19(20):19627, 2011. doi: 10.1364/oe.19.019627.

[126] Anh Phong Tran and Steven L. Jacques. Modeling voxel-based Monte Carlo light transport with curved and oblique boundary surfaces. *Journal of Biomedical Optics*, 25(02):1, 2020. doi: 10.1117/1.jbo.25.2.025001.

[127] Steven L. Jacques. Coupling 3D Monte Carlo light transport in optically heterogeneous tissues to photoacoustic signal generation. *Photoacoustics*, 2 (4):137–142, 2014. doi: 10.1016/j.pacs.2014.09.001.

[128] Adam R. Gardner and Vasan Venugopalan. Accurate and efficient Monte Carlo solutions to the radiative transport equation in the spatial frequency domain. *Optics Letters*, 36(12):2269, 6 2011. doi: 10.1364/OL.36.002269.

[129] Wenqi Lu, Jinming Duan, David Orive-Miguel, Lionel Herve, and Iain B. Styles. Graph- and finite element-based total variation models for the inverse problem in diffuse optical tomography. *Biomedical Optics Express*, 10(6): 2684, 2019. ISSN 2156-7085. doi: 10.1364/boe.10.002684.

[130] Michael Jermyn, Hamid R. Ghadyani, Michael A. Mastanduno, Wesley D. Turner, Scott C. Davis, Hamid Dehghani, and Brian W. Pogue. Fast segmentation and high-quality three-dimensional volume mesh creation from medical

images for diffuse optical tomography. *Journal of Biomedical Optics*, 18(8): 086007, 2013. doi: 10.1117/1.JBO.18.8.086007.

[131] Lei Xi, Xiaoqi Li, Lei Yao, Stephen Grobmyer, and Huabei Jiang. Design and evaluation of a hybrid photoacoustic tomography and diffuse optical tomography system for breast cancer detection. *Medical physics*, 39(5):2584–2594, 2012.

[132] Reheman Baikejiang, Wei Zhang, and Changqing Li. Diffuse optical tomography for breast cancer imaging guided by computed tomography: A feasibility study. *Journal of X-ray Science and Technology*, 25(3):341–355, 2017.

[133] Ravi Prasad K Jagannath and Phaneendra K Yalavarthy. Approximation of internal refractive index variation improves image guided diffuse optical tomography of breast. *IEEE transactions on biomedical engineering*, 57(10): 2560–2563, 2010.

[134] Adam T Eggebrecht, Silvina L Ferradal, Amy Robichaux-Viehoever, Mahlega S Hassanpour, Hamid Dehghani, Abraham Z Snyder, Tamara Hershey, and Joseph P Culver. Mapping distributed brain function and networks with diffuse optical tomography. *Nature photonics*, 8(6):448–454, 2014.

[135] Anna Custo, David A. Boas, Daisuke Tsuzuki, Ippeita Dan, Rickson Mesquita, Bruce Fischl, W. Eric L. Grimson, and Williams Wells. Anatomical atlas-guided diffuse optical tomography of brain activation. *NeuroImage*, 49 (1):561–567, 2010. doi: https://doi.org/10.1016/j.neuroimage.2009.07.033.

[136] NIRFAST: Open source software for multi-modal optical molecular imaging. URL `https://milab.host.dartmouth.edu/nirfast/`.

[137] L. C. Henyey and J. Greenstein. Diffuse radiation in the Galaxy. *Astrophysical Journal*, 147(3733):70–83, 1940. doi: 10.1086/144246.

[138] J. S. Hendricks and Thomas Edward Booth. *MCNP variance reduction overview*. 1985. doi: 10.1007/bfb0049037.

[139] Carole K. Hayakawa, Lisa Malenfant, Janaka C. Ranasinghesagara, David J. Cuccia, Jerome Spanier, and Vasan Venugopalan. MCCL: an open-source software application for Monte Carlo simulations of radiative transport. *https://doi.org/10.1117/1.JBO.27.8.083005*, 27(8):083005, 4 2022. doi: 10.1117/1.JBO.27.8.083005.

[140] Takahiro Kono and Jun Yamada. In Vivo Measurement of Optical Properties of Human Skin for 450–800 nm and 950–1600 nm Wavelengths. *International Journal of Thermophysics*, 40(5):1–14, 2019. doi: 10.1007/s10765-019-2515-3.

[141] Thinh Phan, Rebecca Rowland, Adrien Ponticorvo, Binh C Le, Robert H Wilson, Seyed A Sharif, Gordon T Kennedy, Nicole P. Bernal, and Anthony J Durkin. Characterizing reduced scattering coefficient of normal human skin across different anatomic locations and Fitzpatrick skin types using spatial frequency domain imaging. *Journal of Biomedical Optics*, 26(02):1–11, 2021. doi: 10.1117/1.jbo.26.2.026001.

[142] Gloria M. Spirou, Alexander A. Oraevsky, I. Alex Vitkin, and William M. Whelan. Optical and acoustic properties at 1064 nm of polyvinyl chloride-plastisol for use as a tissue phantom in biomedical optoacoustics. *Physics in Medicine and Biology*, 50(14), 2005. doi: 10.1088/0031-9155/50/14/N01.

[143] Andrea Bassi, Cosimo D'Andrea, Gianluca Valentini, Rinaldo Cubeddu, and Simon Arridge. Detection of inhomogeneities in diffusive media using spatially modulated light. *Optics Letters*, 34(14):2156, 2009. doi: 10.1364/ol.34.002156.

[144] Kyle P. Nadeau, Tyler B. Rice, Anthony J. Durkin, and Bruce J. Tromberg. Multifrequency synthesis and extraction using square wave projection patterns for quantitative tissue imaging. *Journal of Biomedical Optics*, 20(11): 116005, 2015. doi: 10.1117/1.jbo.20.11.116005.

[145] Charles S. Williams and Orville A. Becklund. *Introduction to the Optical Transfer Function*. SPIE, 9 2002. ISBN 9780819443366. doi: 10.1117/3.2265056.

[146] openSFDI: Step-by-step instructions for building an SFDI system. URL `https://opensfdi.org/`.

[147] appSFDI, 2019. URL `https://opensfdi.org/appsfdi/`.

[148] Brian W. Pogue and Michael S. Patterson. Review of tissue simulating phantoms for optical spectroscopy, imaging and dosimetry. *Journal of Biomedical Optics*, 11(4):041102, 2006. doi: 10.1117/1.2335429.

[149] M. Firbank and D. T. Delpy. A phantom for the testing and calibration of near infra-red spectrometers. *Physics in Medicine and Biology*, 39(9):1509–1513, 1994. doi: 10.1088/0031-9155/39/9/015.

[150] Sreyankar Nandy, Atahar Mostafa, Patrick D Kumavor, Melinda Sanders, Molly Brewer, and Quing Zhu. Characterizing optical properties and spatial heterogeneity of human ovarian tissue using spatial frequency domain imaging. *Journal of Biomedical Optics*, 21(10):101402, 2016. doi: 10.1117/1.jbo.21.10.101402.

[151] Frederick Ayers, Alex Grant, Danny Kuo, David J. Cuccia, and Anthony J. Durkin. Fabrication and characterization of silicone-based tissue phantoms with tunable optical properties in the visible and near infrared domain. *Design and Performance Validation of Phantoms Used in Conjunction with Optical Measurements of Tissue*, 6870:687007, 2008. doi: 10.1117/12.764969.

[152] Hugo J. van Staveren, Christian J. M. Moes, Jan van Marie, Scott A. Prahl, and Martin J. C. van Gemert. Light scattering in lntralipid-10% in the wavelength range of 400–1100 nm. *Applied Optics*, 30(31):4507, 1991. doi: 10.1364/ao.30.004507.

[153] Andrea Bassi, David J. Cuccia, Anthony J. Durkin, and Bruce J. Tromberg. Spatial shift of spatially modulated light projected on turbid media. *Journal of the Optical Society of America A*, 25(11):2833, 11 2008. doi: 10.1364/JOSAA.25.002833.

[154] Lindokuhle Ntombela, Bamise Adeleye, and Naven Chetty. Low-cost fabrication of optical tissue phantoms for use in biomedical imaging. *Heliyon*, 6 (3), 3 2020. doi: 10.1016/J.HELIYON.2020.E03602.

[155] Huub Vermeulen. Investigation of the Influence of the Scattering Coefficient on Acousto-Optic Modulation Efficiency. page 20, 2012.

[156] M. Firbank, M. Oda, and D. T. Delpy. An improved design for a stable and reproducible phantom material for use in near-infrared spectroscopy and imaging. *Physics in Medicine and Biology*, 40(5):955–961, 1995. doi: 10.1088/0031-9155/40/5/016.

[157] Rolf B. Saager, Clement Kondru, Kendrew Au, Kelly Sry, Frederick Ayers, and Anthony J. Durkin. Multilayer silicone phantoms for the evaluation of quantitative optical techniques in skin imaging. *Design and Performance Validation of Phantoms Used in Conjunction with Optical Measurement of Tissue II*, 7567(February 2010):756706, 2010. doi: 10.1117/12.842249.

[158] Alexey N. Bashkatov, Elina A. Genina, Vyacheslav I. Kochubey, and Valery V. Tuchin. Effects of scattering particle concentration on light propagation through turbid media. *Optical Biopsy III*, 3917(April 2000): 256–263, 2000. doi: 10.1117/12.382742.

[159] Paul Kubelka. Ein beitrag zur optik der farbanstriche. *Z. tech. Phys*, 12: 593–601, 1931.

[160] Suresh N Thennadil. Relationship between the kubelka-munk scattering and radiative transfer coefficients. *JOSA A*, 25(7):1480–1485, 2008.

[161] Optical absorption of hemoglobin. URL `https://omlc.org/spectra/hemoglobin/`.

[162] Amy Stanway. Atopic dermatitis, 2004. URL `https://dermnetnz.org/topics/atopic-dermatitis`.

[163] Atopic Dermatitis. URL `https://www.niams.nih.gov/health-topics/atopic-dermatitis`.

[164] The Eczema Area and Severity Index-A Practical Guide. *Dermatitis : contact, atopic, occupational, drug*, 33(3):187–192, 2022. doi: 10.1097/DER.0000000000000895.

[165] Sunil Kalia, Haishan Zeng, Tashmeeta Ahad, Jianhua Zhao, and Harvey Lui. Using spectroscopy to study skin conditions. In *Photonics in Dermatology and Plastic Surgery 2023*, page PC123520A. SPIE, 2023.

[166] Kapil Dev, Chris Jun Hui Ho, Renzhe Bi, Yik Weng Yew, Dinish U. S, Amalina Binte Ebrahim Attia, Mohesh Moothanchery, Steven Thng Tien, and Malini Olivo. Machine Learning Assisted Handheld Confocal Raman Micro-Spectroscopy for Identification of Clinically Relevant Atopic Eczema Biomarkers. *Sensors*, 22(13), 2022. doi: 10.3390/s22134674.

[167] Marianne Hald, Jacob P. Thyssen, Claus Zachariae, Mads A. Røpke, Jens M. Carstensen, Nette Schultz, and Jeanne D. Johansen. Multispectral imaging of hand eczema. *Contact Dermatitis*, 81(6):438–445, dec 2019. doi: 10.1111/cod.13377.

[168] Robert A. Byers, Raman Maiti, Simon G. Danby, Elaine J. Pang, Bethany Mitchell, Matt J. Carré, Roger Lewis, Michael J. Cork, and Stephen J. Matcher. Sub-clinical assessment of atopic dermatitis severity using angiographic optical coherence tomography. *Biomedical Optics Express*, 9(4):2001, 2018. doi: 10.1364/boe.9.002001.

[169] Linh Ha-Wissel, Handan Yasak, Robert Huber, Detlef Zillikens, Ralf J. Ludwig, Diamant Thaçi, and Jennifer E. Hundt. Case report: Optical coherence tomography for monitoring biologic therapy in psoriasis and atopic dermatitis. *Frontiers in Medicine*, 9(September):1–10, 2022. doi: 10.3389/fmed.2022.995883.

[170] Mohesh Moothanchery, Amalina Binte Ebrahim Attia, Xiuting Li, Yew Yik Weng, Steven Thng, Dinish U.S., and Malini Olivo. Assessment of oxygen saturation in microvasculature of atopic dermatitis patients using multispectral optoacoustic mesoscopy. 1193902(March 2022):7, 2022. doi: 10.1117/12.2610600.

[171] Shangshang Wang, Rui-Xing Yu, Wen Fan, Cheng-Xu Li, Wen-Min Fei, Shanshan Li, Junfeng Zhou, Ruiming Hu, Mengguo Liu, Feng Xu, Jinhua Xu, and Yong Cui. Detection of skin thickness and density in healthy Chinese people by using high-frequency ultrasound. *Skin Research and Technology*, 29(1): 1–14, jan 2023. doi: 10.1111/srt.13219.

[172] Kajal Patel and Rosemary Nixon. Irritant Contact Dermatitis — a Review. *Current Dermatology Reports*, 11(2):41–51, 2022. doi: 10.1007/s13671-021-00351-4.

[173] Rabia Sofia Rashid and Tang Ngee Shim. Contact dermatitis. *BMJ (Online)*, 353, 2016. doi: 10.1136/bmj.i3299.

[174] Manigé Fartasch, Esther Schnetz, and Thomas L. Diepgen. Characterization of Detergent-Induced Barrier Alterations — Effect of Barrier Cream on Irritation. *Journal of Investigative Dermatology Symposium Proceedings*, 3(2): 121–127, aug 1998. doi: 10.1038/jidsymp.1998.25.

[175] Irritant contact dermatitis. *Reviews on Environmental Health*, 29(3):195–206, 2014. doi: 10.1515/reveh-2014-0060.

[176] Kanwaljit K. Brar. A review of contact dermatitis. *Annals of Allergy, Asthma and Immunology*, 126(1):32–39, 2021. doi: 10.1016/j.anai.2020.10.003.

[177] R. A. Tupker, C. Willis, E. Berardksca, C. H. Lee, M. Fartasch, T. Atinrat, and J. Serup. Guidelines on sodium lauryl sulfate (SLS) exposure tests. *Contact Dermatitis*, 37(2):53–69, 1997. doi: 10.1111/j.1600-0536.1997.tb00041.x.

[178] Bente Brokstad Herlofson, Pal Brodin, and Harald Aars. Increased human gingival blood flow induced by sodium lauryl sulfate. *Journal of Clinical Periodontology*, 23(11):1004–1007, 1996. doi: 10.1111/j.1600-051x.1996.tb00528.x.

[179] Taeko Mizutani, Ryota Mori, Misaki Hirayama, Yuki Sagawa, Kenji Shimizu, Yuri Okano, and Hitoshi Masaki. Sodium lauryl sulfate stimulates the generation of reactive oxygen species through interactions with cell membranes. *Journal of Oleo Science*, 65(12):993–1001, 2016. doi: 10.5650/jos.ess16074.

[180] Thomas P.A. Hughes, Ifan G., Hase. *Measurements and their Uncertainties: A practical guide to modern error analysis*. Oxford University Press, 2010.

[181] Gaby Novak-Bilić, Majda Vučić, Iva Japundžić, Jelena Meštrović-štefekov, Sandra Stanić-Duktaj, and Liborija Lugović-Mihić. Irritant and allergic contact dermatitis – skin lesion characteristics. *Acta Clinica Croatica*, 57(4): 713–720, 2018. doi: 10.20471/acc.2018.57.04.13.

[182] Yanyu Zhao, Anahita Pilvar, Anup Tank, Hannah Peterson, John Jiang, Jon C Aster, John Paul Dumas, Mark C Pierce, and Darren Roblyer. Shortwave-infrared meso-patterned imaging enables label-free mapping of tissue water and lipid content. *Nature Communications*, 11(1):1–12, 2020. doi: 10.1038/s41467-020-19128-7.

[183] Ramy Abdlaty, Joseph Hayward, Thomas Farrell, and Qiyin Fang. Skin erythema and pigmentation: a review of optical assessment techniques. *Pho-*

todiagnosis and Photodynamic Therapy, 33(October 2020):102127, 2021. doi: 10.1016/j.pdpdt.2020.102127.

[184] Stephen S. Cheung. Responses of the hands and feet to cold exposure. *Temperature*, 2(1):105–120, 2015. doi: 10.1080/23328940.2015.1008890.

[185] David G. Lowe. Distinctive image features from scale-invariant keypoints. *International Journal of Computer Vision*, 60(2):91–110, 2004. doi: 10.1023/B:VISI.0000029664.99615.94.

[186] Martin A. Fischler and Robert C. Bolles. Random sample consensus: A Paradigm for Model Fitting with Applications to Image Analysis and Automated Cartography. *Communications of the ACM*, 24(6):381–395, 1981. doi: 10.1145/358669.358692.

[187] Michael S. Weingarten, Elisabeth S. Papazoglou, Leonid Zubkov, Linda Zhu, Michael Neidrauer, Guy Savir, Kim Peace, John G. Newby, and Kambiz Pourrezaei. Correlation of near infrared absorption and diffuse reflectance spectroscopy scattering with tissue neovascularization and collagen concentration in a diabetic rat wound healing model. *Wound Repair and Regeneration*, 16 (2):234–242, 2008. doi: 10.1111/j.1524-475X.2008.00364.x.

[188] S. Schreml, R. M. Szeimies, L. Prantl, S. Karrer, M. Landthaler, and P. Babilas. Oxygen in acute and chronic wound healing. *British Journal of Dermatology*, 163(2):257–268, 2010. doi: 10.1111/j.1365-2133.2010.09804.x.

[189] Diego M. Castilla, Zhao-Jun Liu, and Omaida C. Velazquez. Oxygen: Implications for Wound Healing. *Advances in Wound Care*, 1(6):225–230, 2012. doi: 10.1089/wound.2011.0319.

[190] Michael S. Weingarten, Michael Neidrauer, Alina Mateo, Xiang Mao, Jane E. McDaniel, Lori Jenkins, Sara Bouraee, Leonid Zubkov, Kambiz Pourrezaei, and Elisabeth S. Papazoglou. Prediction of wound healing in human diabetic

foot ulcers by diffuse near-infrared spectroscopy: A pilot study. *Wound Repair and Regeneration*, 18(2):180–185, 2010. doi: 10.1111/j.1524-475X.2010.00583.x.

[191] C. L. Campbell, C. T.A. Brown, K. Wood, and H. Moseley. Modelling topical photodynamic therapy treatment including the continuous production of Protoporphyrin IX. *Physics in Medicine and Biology*, 61(21):7507–7521, 2016. doi: 10.1088/0031-9155/61/21/7507.

[192] C. L. Campbell, K. Wood, R. M. Valentine, C. T.A. Brown, and H. Moseley. Monte Carlo modelling of daylight activated photodynamic therapy. *Physics in Medicine and Biology*, 60(10):4059–4073, 2015. doi: 10.1088/0031-9155/60/10/4059.

[193] Wanda A. Dorsett-Martin and Annette B. Wysocki. Rat models of skin wound healing. *Source Book of Models for Biomedical Research*, pages 631–638, 2008. doi: 10.1007/978-1-59745-285-4_65.

[194] PRISCILLA L Walling and JACQUELYN M Dabney. Moisture in skin by near-infrared reflectance spectroscopy. *J. Soc. Cosmet. Chem*, 40(3):151–171, 1989.

[195] Christopher Graham, John M. Girkin, and Cyril Bourgenot. Freeform based hyperspectral imager for moisture sensing (fymos). *Opt. Express*, 29(11):16007–16018, May 2021. doi: 10.1364/OE.425660.

[196] Jean Micheels, Bjarne Aisbjorn, and Bent Sorensen. Laser doppler flowmetry. a new non-invasive measurement of microcirculation in intensive care? *Resuscitation*, 12(1):31–39, 1984.

[197] Takeo Ishii, Shizuka Takabe, Yuki Yanagawa, Yuko Ohshima, Yasuhiro Kagawa, Atsuko Shibata, and Kunio Oyama. Laser doppler blood flowmeter as a useful instrument for the early detection of lower extremity peripheral

arterial disease in hemodialysis patients: an observational study. *BMC nephrology*, 20(1):1–11, 2019.

Colophon

This thesis is based on a template developed by Matthew Townson and Andrew Reeves. It was typeset with LaTeX 2_ε. It was created using the *memoir* package, maintained by Lars Madsen, with the *madsen* chapter style. The font used is Latin Modern, derived from fonts designed by Donald E. Kunith.